Microporous and Mesoporous Materials 117 (2009) 22–32

Contents lists available at ScienceDirect

Microporous and Mesoporous Materials

journal homepage: www.elsevier.com/locate/micromeso

Adsorption and diffusion of alkanes in CuBTC crystals investigated using infra-red microscopy and molecular simulations

C. Chmelik [a], J. Kärger [a], M. Wiebcke [b], J. Caro [c], J.M. van Baten [d], R. Krishna [d,*]

[a] Abteilung Grenzflächenphysik, Universität Leipzig, Linnéstrasse 5, D-04103 Leipzig, Germany
[b] Leibniz University of Hannover, Institut für Anorganische Chemie, Callinstrasse 9, D-30167 Hannover, Germany
[c] Leibniz University of Hannover, Institute of Physical Chemistry and Electrochemistry, Callinstrasse 3-3a, D-30167 Hannover, Germany
[d] Van 't Hoff Institute for Molecular Sciences, University of Amsterdam, Nieuwe Achtergracht 166, 1018 WV Amsterdam, The Netherlands

ARTICLE INFO

Article history:
Received 1 April 2008
Received in revised form 3 June 2008
Accepted 4 June 2008
Available online 13 June 2008

Keywords:
Maxwell–Stefan diffusivity
Adsorption
Molecular dynamics
Configurational-Bias Monte Carlo
Thermodynamic factor
Infra-red microscopy
Isotherm inflection
Alkanes
Metal-organic frameworks
CuBTC

ABSTRACT

The adsorption and intra-crystalline diffusion of *n*-butane (nC4), iso-butane (iC4), 2-methylbutane (2MB), and 2,2-dimethylpropane (neoP) in CuBTC ($Cu_3(BTC)_2$ where BTC = benzene-1,3,5-tricarboxylate) has been investigated using infrared microscopy (IRM), combined with molecular simulations. Both experiments and simulations show strong inflection characteristics in the adsorption isotherms. The primary cause of the inflection is due to the strong preference for adsorption within, and in the regions close to the mouths of tetrahedral pockets. The isotherm inflection has a significant influence on the dependence of the Maxwell–Stefan diffusivity, $Đ_i$, on the fractional occupancy, $Đ_i$. Both IRM experiments and simulations show that the $Đ_i$–θ_i behavior appears to be influenced by the loading dependence of the inverse thermodynamic factor $1/\Gamma_i = \mathrm{d}\ln\theta_i/\mathrm{d}\ln p_i$. For nC4 and iC4, the $Đ_i$ increase sharply by about one order of magnitude as the occupancy θ_i increases from 0 to about 0.2. This increase is caused by the fact that the diffusion characteristics undergo a transition from being dominated by hops across narrow 4.6 Å windows at low loadings to hops across large 9 Å windows for loadings higher than 8 molecules per unit cell. For loadings higher than 8 molecules per unit cell the $Đ_i$–θ_i dependence of nC4 and iC4 is dictated by $1/\Gamma_i$, characteristic of more open channel structures such as FAU zeolite. For 2MB and neoP, the IRM experiments show evidence of phase transition and except for the region in which this occurs the $Đ_i$ follows the occupancy dependence of $1/\Gamma_i$ for the entire range of loadings.

1. Introduction

In recent years there has been a remarkable upsurge in research activity on metal-organic frameworks (MOFs), in view of several potential applications in storage, separations, and catalysis [1–4]. A wide variety of MOFs have been synthesized, and investigated. The potential of MOFs for separations of variety of mixtures such as CO_2/N_2, CO_2/CH_4, CO_2/CO, CO_2/C_2H_4, C_2H_6/C_2H_4, and hydrocarbons have been investigated both experimentally [5–13] and by use of molecular simulations [14–20].

In the development of separation technologies using MOFs, data are required on both adsorption and diffusion of guest molecules. Both experimental and molecular simulation studies have shown the adsorption characteristics of a variety of guest-MOF host combinations to be rather complex and often exhibiting inflection characteristics in the isotherm, caused due to the existence of different adsorption sites of significantly varying strengths [21–27]. For zeolites, inflection in the isotherm is known to have a significant influence on the dependence of the Maxwell–Stefan (M–S) diffusivity, $Đ_i$ on the fractional occupancy, θ_i [28–30]. The only published experimental studies on diffusion in MOFs, that we are aware of are due to Stallmach et al. [31] who investigated the temperature dependence of self-diffusivities of alkanes in IRMOF-1 using PFG NMR, and Kortunov et al. [32] who used interference microscopy to study diffusion of methanol in manganese formate. Molecular dynamics (MD) simulation results have been published on the $Đ_i$–θ_i relation for small molecules such as Ar, CH_4, CO_2, N_2, Ar, Ne and H_2 [26,33,34]. In none of these MD simulations, inflection in $Đ_i$–θ_i dependence has been reported.

The current work focuses on one important MOF, i.e. CuBTC ($Cu_3(BTC)_2$ with BTC = benzene-1,3,5-tricarboxylate), whose synthesis was first reported by Chui et al. [35]. Our major objective is to gain insights into the adsorption and diffusion of a variety of linear and branched alkanes in CuBTC, with a view to examining the potential of this material in alkane separations. We aim to demonstrate the strong influence of isotherm inflection on the θ_i-dependence of the M–S diffusivity $Đ_i$. Our study uses a combination of molecular

* Corresponding author. Tel.: +31 20 5257007; fax: +31 20 5255604.
E-mail address: r.krishna@uva.nl (R. Krishna).

1387-1811/$ - see front matter © 2008 Elsevier Inc. All rights reserved.
doi:10.1016/j.micromeso.2008.06.003

Nomenclature

D_i	Fick, or transport, diffusivity, $m^2\ s^{-1}$
$Đ_{ii}$	self-exchange coefficient, $m^2\ s^{-1}$
$Đ_i$	Maxwell–Stefan diffusivity of species i, $m^2\ s^{-1}$
$Đ_i(0)$	zero-loading M–S diffusivity of species i, $m^2\ s^{-1}$
f_i	fugacity of species i, Pa
ΔH_{st}	isosteric heat of adsorption, J mol^{-1}
n_i	number of molecules of species i in simulation box, dimensionless
p_i	pressure, Pa
q_i	loading of species i, molecules per unit cell
$q_{i,sat}$	saturation loading of species i, molecules per unit cell
r	position vector, m
R	gas constant, 8.314 J $mol^{-1}\ K^{-1}$
t	time, s
T	absolute temperature, K
x	spatial distance, m

Greek letters

Γ_i	thermodynamic correction factor, dimensionless
θ_i	fractional occupancy, $\theta_i = q_i/q_{i,sat}$, dimensionless
ν_i	power in Sips isotherm, dimensionless
μ_i	molar chemical potential, J mol^{-1}
ρ	framework density, kg m^{-3}

Subscripts

sat	referring to saturation conditions
i	referring to component i

simulations (Configurational-Bias Monte Carlo (CBMC) for adsorption, and MD for diffusion), and Infra-red Microscopy (IRM) [36,37]. Details of the crystal synthesis, IRM experimental set-up, experimental technique, molecular simulation methodology,

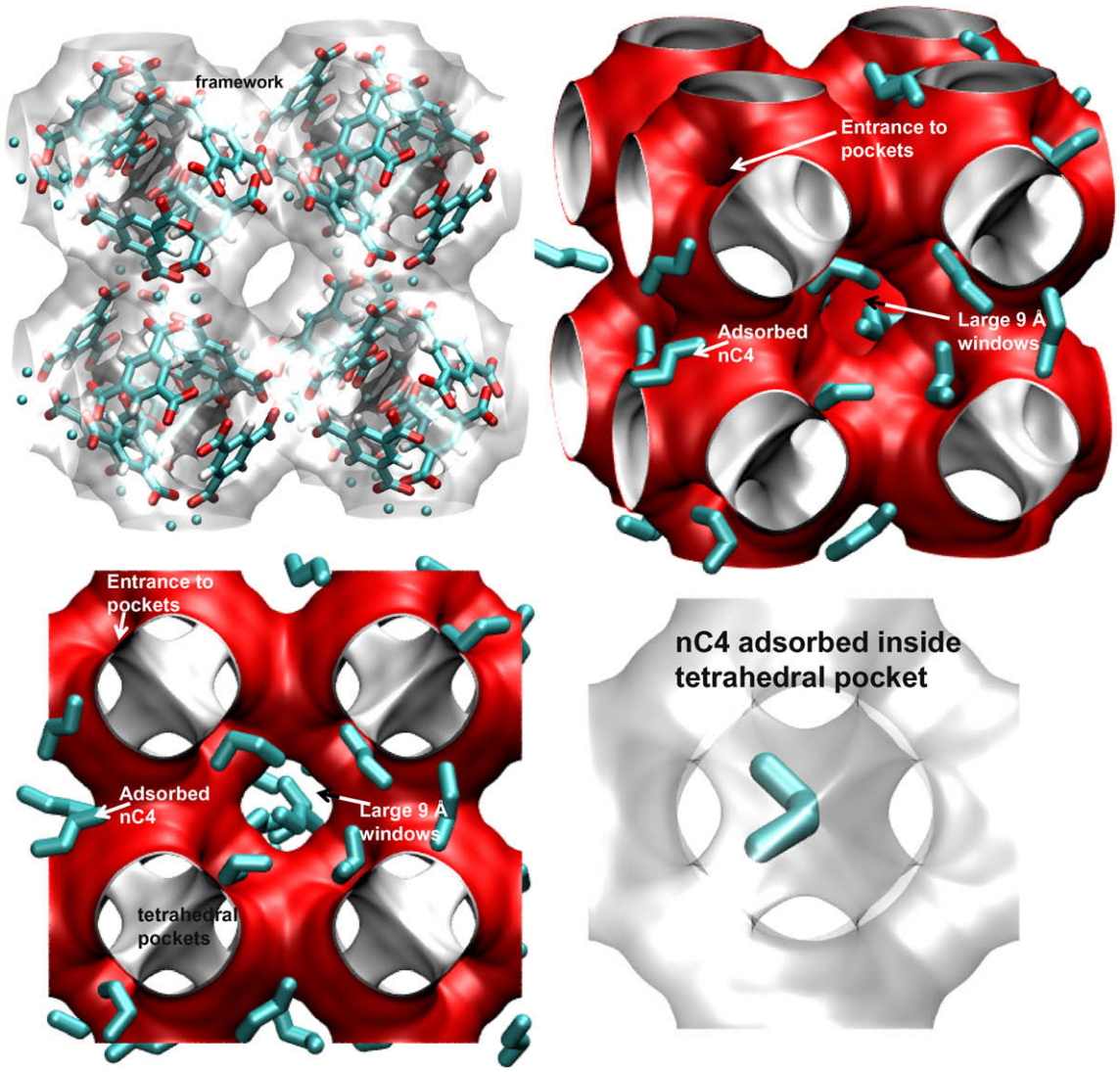

Fig. 1. The framework structure and different views of the pore landscape of CuBTC. The red areas are accessible to guest molecules in the large cage, such as nC4 pictured here. Also shown is one nC4 molecule adsorbed within a tetrahedral pocket.

description of the force fields used, and molecular simulation data for the adsorption isotherms, and the M–S diffusivity $Đ_i$ are given in the Supplementary material accompanying this publication.

The crystal structure of CuBTC includes axial oxygen atoms weakly bonded to the Cu atoms, which correspond to water ligands; our experiments and simulations were performed on dry CuBTC crystals with these oxygen atoms removed (this occurs during the activation of the crystals used in the IRM experiments). The unit cell dimensions are $a = b = c = 26.343$ Å; see the framework, along with snapshots of adsorbed molecules in the pore landscapes in Fig. 1. The CuBTC structure consists of two types of "cages" and two types of "windows" separating these cages. Large cages are inter-connected by 9 Å windows of square cross-section. The large cages are also connected to tetrahedral-shaped pockets of ca. 6 Å size through triangular-shaped windows of ca. 4.6 Å size (the window size is quoted to be 3.5 Å for the hydrated crystal [16]); see the cartoon in Fig. 2. There are 8 pockets per unit cell.

All the simulations reported in this study were performed with the assumption of a rigid framework. In recent work it has been shown that lattice flexibility will have a profound influence on MD simulated diffusivities [38].

2. Molecular simulations of adsorption and diffusion

Even though there is insufficient amount of experimental adsorption data for alkanes in CuBTC, or indeed in any MOF, to develop reliable force fields, molecular simulations using generic force fields such as UFF [39] and DREIDING [40] are still valuable in developing insights into the adsorption and diffusion characteristics. For linear and branched alkanes with carbon numbers in the 1–5 range the data for the adsorption isotherms (q_i vs. f_i), inverse thermodynamic factor ($1/\Gamma_i$), M–S diffusivity, $Đ_i$, were determined. Rather than calculating the $1/\Gamma_i$ by analytic, or numerical, differentiation of the simulated adsorption isotherms, the $1/\Gamma_i$ data are directly obtained by analyzing several samples of equilibrated molecules within the simulation box and using the Reed and Ehrlich fluctuation formula

$$\frac{1}{\Gamma_i} = \frac{\langle n_i^2 \rangle - \langle n_i \rangle^2}{\langle n_i \rangle} \tag{1}$$

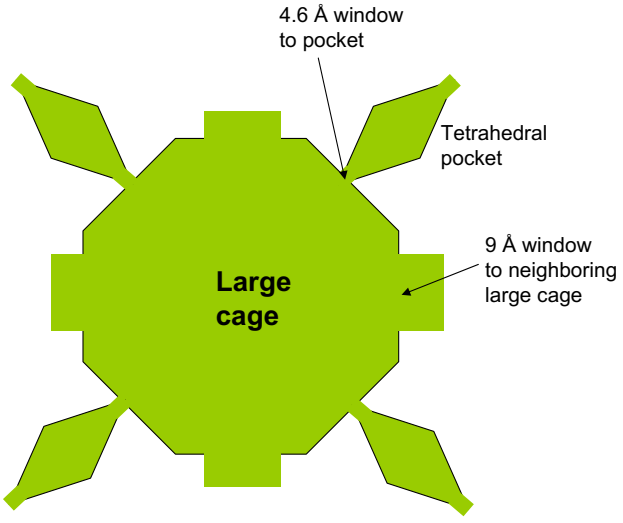

Fig. 2. Cartoon showing large cage, with windows to neighboring large cages, and to tetrahedral pockets.

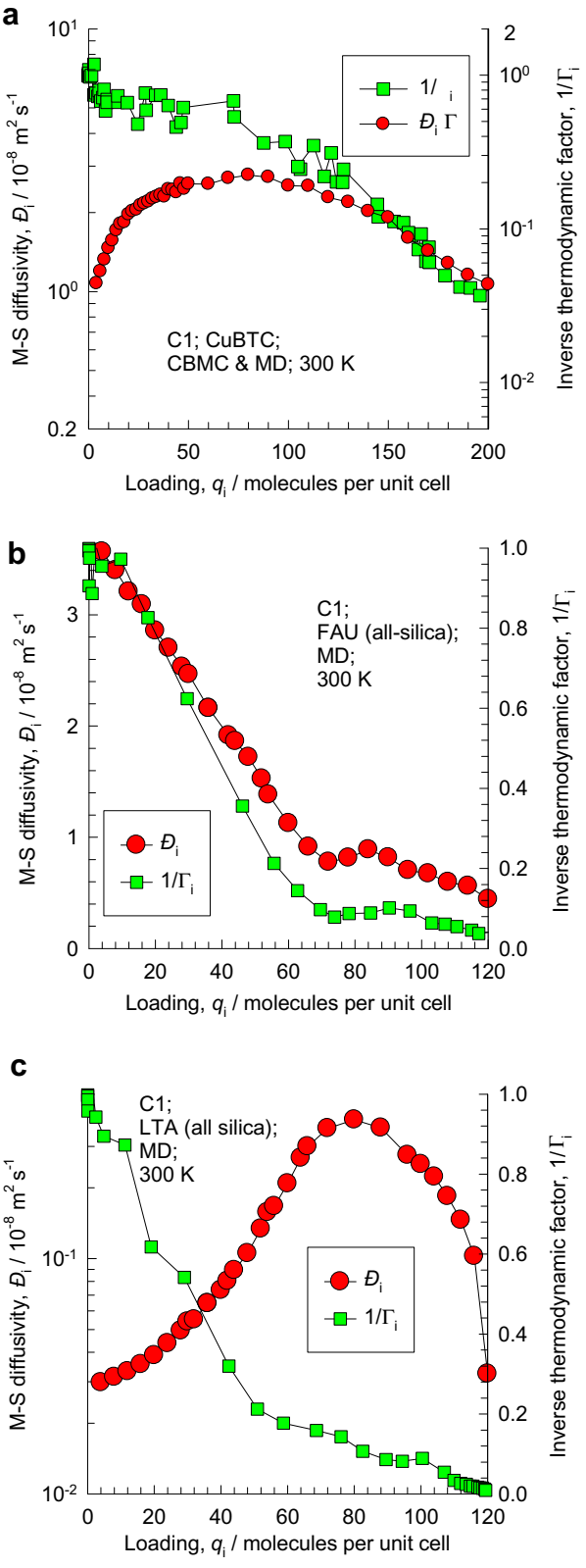

Fig. 3. Variation of the Maxwell–Stefan diffusivity $Đ_i$, and the inverse thermodynamic factor $1/\Gamma_i$ of methane with molecular loading for (a) CuBTC, (b) FAU zeolite, and (c) LTA zeolite. The symbols represent results of CBMC and MD simulations; simulation details are given in the Supplementary material. The FAU and LTA data are from earlier work [44].

where n_i represents the number of molecules in the simulation box and $\langle \ldots \rangle$ denotes ensemble averaging. This fluctuation formula has

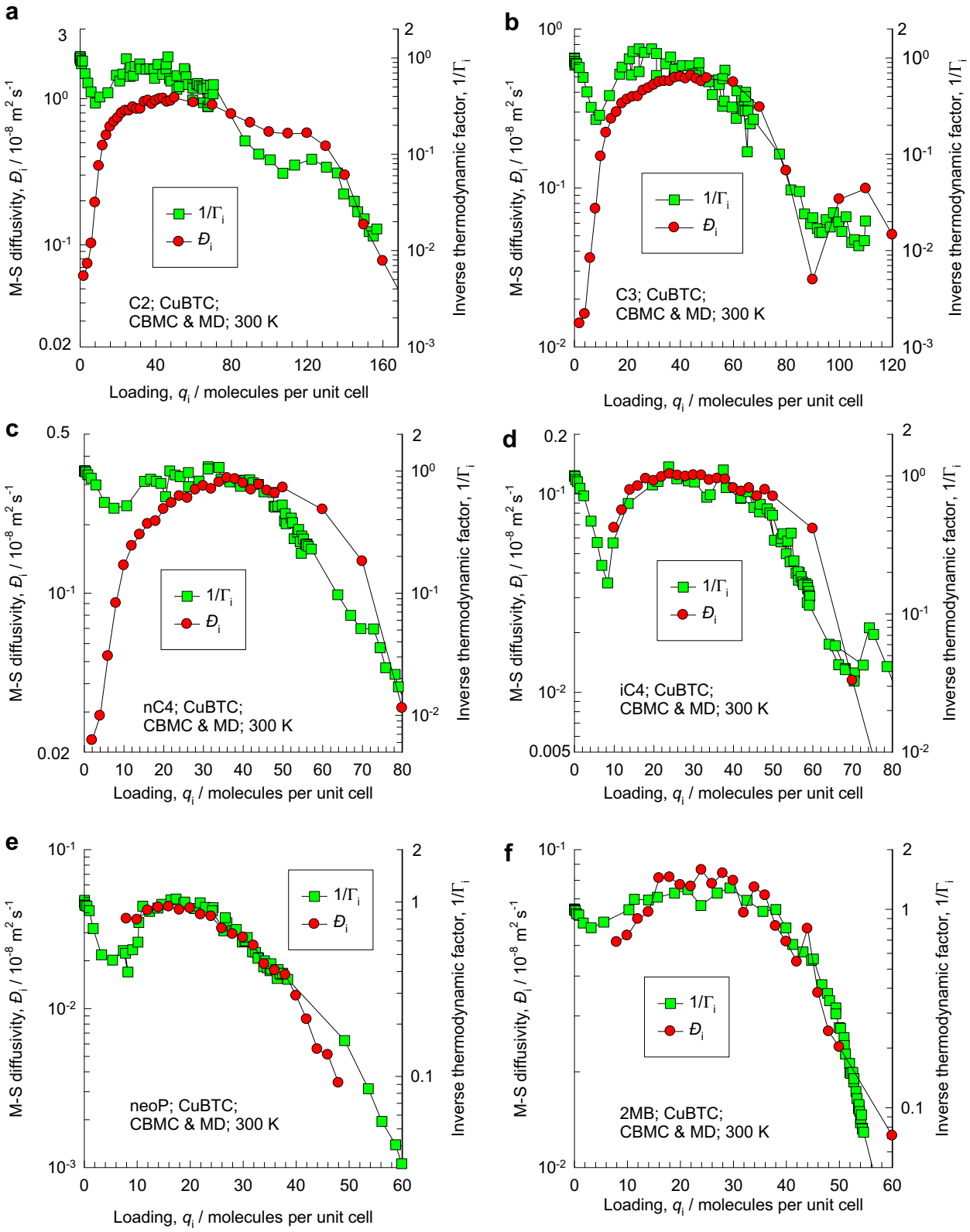

Fig. 4. Variation of the Maxwell–Stefan diffusivity $Đ_i$, and the inverse thermodynamic factor $1/\Gamma_i$ in CuBTC of (a) ethane, (b) propane, (c) *n*-butane, (d) iso-butane, (e) 2,2-dimethylpropane, and (f) 2-methylbutane.

been used in Monte Carlo simulations of adsorption in zeolites [29,41–43].

We shall set the background to further discussions by comparing the $Đ_i$–q_i data for methane (C1) in CuBTC with those in FAU and LTA zeolites; see Fig. 3. Also plotted in Fig. 3 is the CBMC simulated $1/\Gamma_i$–q_i data. Diffusion in FAU is the easiest to comprehend; this is a large pore size zeolite with large 12-ring windows separating cages. C1 is only weakly constrained within FAU, and the loading

dependence approximately follows the general expectation of a lattice model: a molecule can only hop to another site when the recipient site is vacant and therefore in the absence of inter-molecular interactions we may expect

$$Đ_i = Đ_i(0)(1-\theta_i) \quad (2)$$

where $(1-\theta_i)$ is the fractional *vacancy*. For single-site Langmuir adsorption, we have

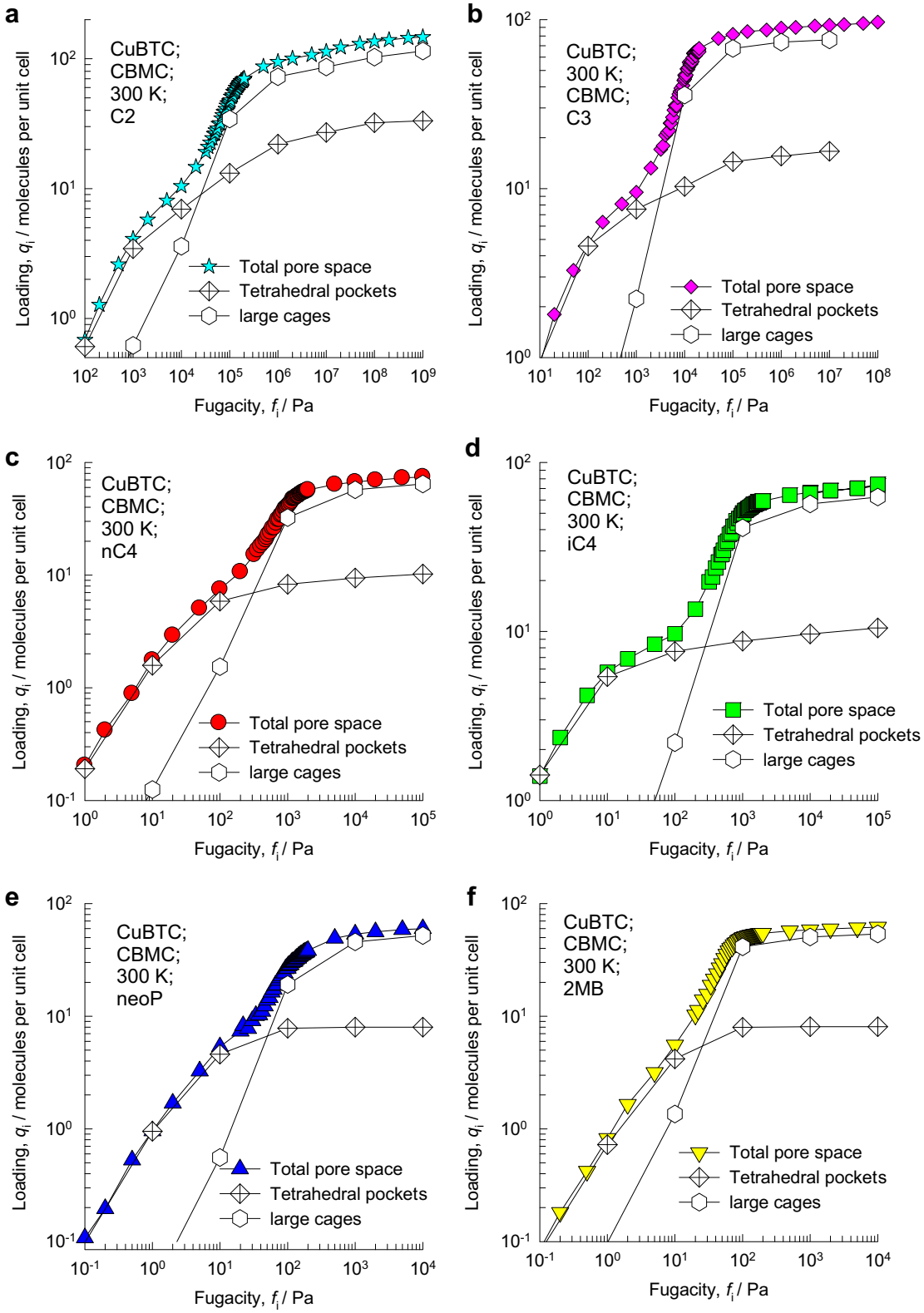

Fig. 5. CBMC simulations of adsorption isotherms in CuBTC for (a) ethane, (b) propane, (c) *n*-butane, (d) iso-butane, (e) 2,2-dimethylpropane, and (f) 2-methylbutane. Also shown is the loading in the tetrahedral pockets, and in the large cages.

$$\Gamma_i \equiv \frac{d \ln f_i}{d \ln q_i} \approx \frac{d \ln p_i}{d \ln q_i} = \frac{d \ln p_i}{d \ln \theta_i} = \frac{1}{1 - q_i/q_{i,sat}} = \frac{1}{1 - \theta_i} \quad (3)$$

For the general case in which the adsorption does not follow single-site Langmuirian behavior we may consider $1/\Gamma_i$ to be an appropriate measure of the vacancy that is available for a molecule to hop toward. A reasonably good model for the occupancy dependence of the M–S diffusivity of C1 in FAU is [43,44]

$$Đ_i = Đ_i(0) \frac{1}{\Gamma_i} \quad (4)$$

The validity of Eq. (4) is demonstrated in Fig. 3b. It is interesting to note that the mild inflection in the $1/\Gamma_i$ vs. q_i data also gets reflected in a corresponding inflection in the $Đ_i$–q_i [43]; see Fig. 3b. Eq. (4) is also a reasonable approximation for diffusion in AFI [43], a large pore zeolite with one-dimensional channels.

A different scenario holds for cage-type zeolites with narrow windows separating cages, such as LTA, CHA, DDR, and ERI [44]. In this case only one C1 molecule can hop between cages at a given time and the $Đ_i$ increases with increasing q_i, before eventually decreasing to near-zero values as saturation is approached; see data for LTA in Fig. 3c. The initial increase in the $Đ_i$ with q_i can be explained in terms of reduction in the free energy barrier for inter-cage hopping due to inter-molecular repulsion forces [44–46]. It is noteworthy that for LTA there is no correlation of the $Đ_i$–q_i variation with that of $1/\Gamma_i$–q_i; the same holds for CHA, DDR, and ERI [44,47]. The diffusivities in LTA are about one order of magnitude lower than that for FAU. There is experimental evidence to verify the loading dependence portrayed in Fig. 3b, c [48,49].

Broadly speaking, diffusion of C1 in CuBTC has features of both FAU and LTA; see Fig. 3a. For loadings $q_i < 50$ molecules per unit cell, the $Đ_i$ increases with q_i, typically observed for LTA. For $q_i > 100$, $Đ_i$ *decreases* with q_i, and this decrease appears to mirror $1/\Gamma_i$–q_i, as found for FAU. A similar *hybrid* diffusion behavior is observed for all *n*-alkanes in CuBTC that we investigated; witness the corresponding data for ethane (C2), propane (C3), and *n*-butane (nC4) in Fig. 4. At low loadings, for C2, C3, and nC4 there is a steep increase in $Đ_i$ with q_i. The diffusivities of branched alkanes: iso-butane, (iC4), 2-methylbutane (2MB), and 2,2-dimethylpropane (neoP = neopentane), at low loadings were too small to be

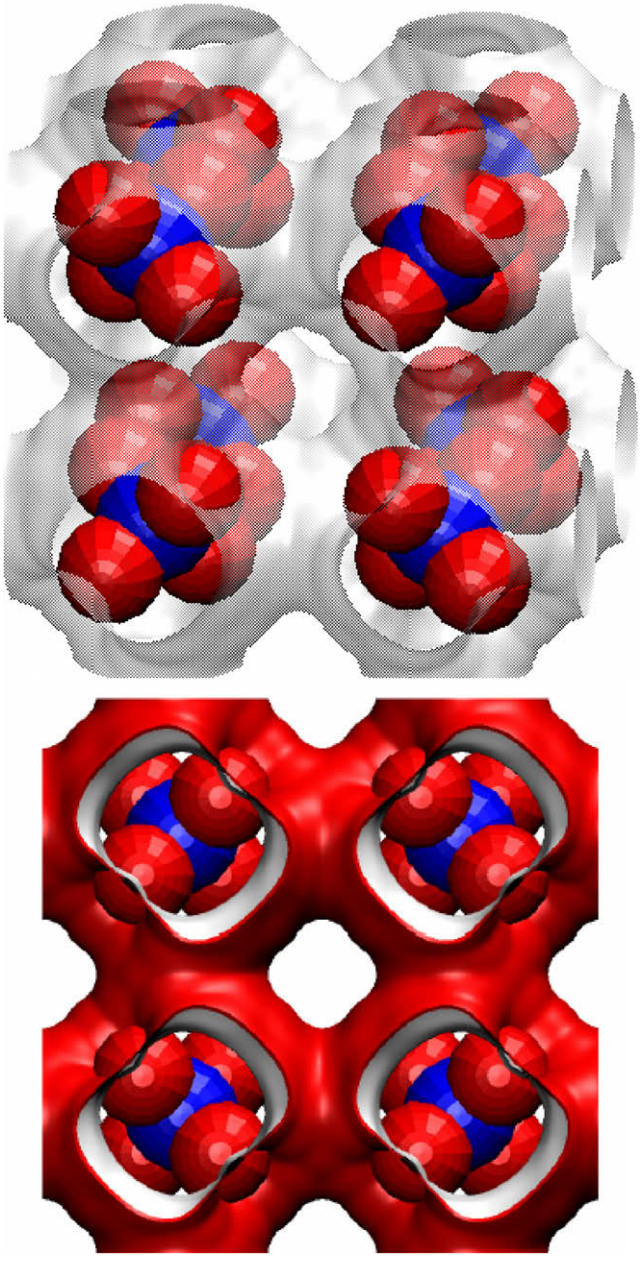

Fig. 6. CuBTC structure in which the red and blue spheres are used to envelop the molecules located in the tetrahedral pockets. (For interpretation of the references to colour in this figure legend, the reader is referred to the web version of this article.)

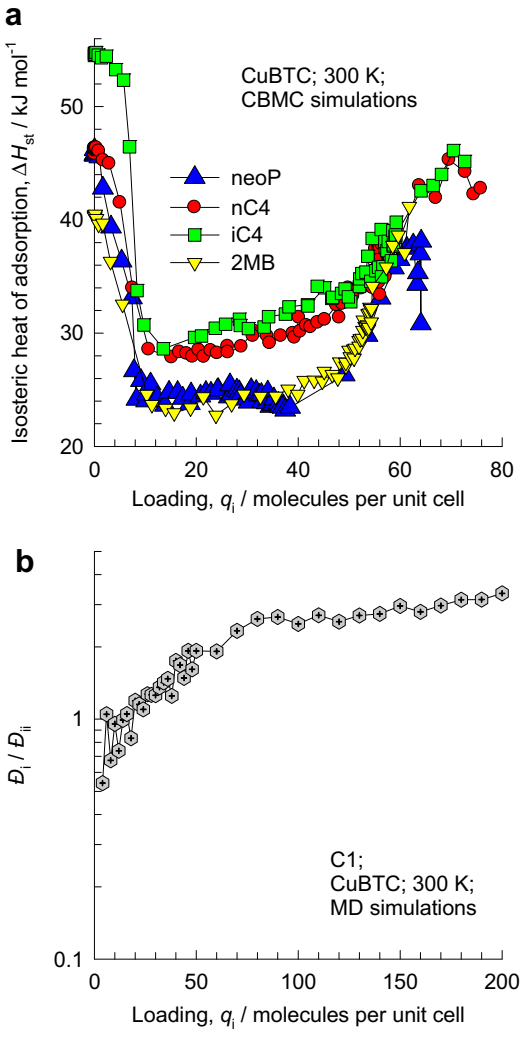

Fig. 7. (a) CBMC simulations of the isosteric heat of adsorption, ΔH_{st}, of alkanes in CuBTC. (b) MD simulations of the variation of $Đ_i/Đ_{ii}$ for C1 with loading.

determined with sufficient accuracy using MD simulations. For *both* linear and branched alkanes at loadings $q_i > 10$ molecules per unit cell, the $Đ_i$–q_i variation is approximately the same as that of $1/\Gamma_i$–q_i; see Fig. 4.

A closer examination of the $1/\Gamma_i$ vs. q_i data in Fig. 4 reveals a distinct inflection at 8 molecules per unit cell for all alkanes. The severe order-of-magnitude increase in $Đ_i$ for C2, C3, and nC4 occurs prior to this inflection. Isotherm inflection is practically non-existent for C1; cf. Fig. 3a.

The inflection in the $1/\Gamma_i$–q_i data in Fig. 4 has its origins in the inflection in the adsorption isotherm; this can be established by examination of the CBMC simulated adsorption isotherms in Fig. 5. To unravel the cause for this inflection, we ran the CBMC simulations for 10^6 cycles and collected equilibrated positions from 10^3 cycles. The region of the tetrahedral pockets was, arbitrarily, taken to be enveloped by the red (mouth region of the pockets) and blue (central region of the pockets) spheres as indicated in Fig. 6. By counting the statistics of 10^3 equilibrated samples we could determine the probabilities of locating a molecule within the pockets or at the mouth to the pockets (total of locations in red and blue spheres), and in the larger cages. Multiplying these probabilities by the total loading yields an estimate of the loading in the pockets and in the large cages; this data has also been plotted in Fig. 5. For C2 and C3, the saturation loadings in the side pockets are 32 and 16 molecules per unit cell, corresponding to 4 and 2 molecules per pocket, respectively, whereas for the C4 and C5 alkanes, the saturation loading in the side pockets is 8 molecules per unit cell, corresponding to 1 molecule per pocket. For all alkanes in Fig. 5, the isotherm inflection occurs at 8 molecules per unit cell; this also corresponds to the saturation loading for the pocket regions for C4 and C5 alkanes.

It is to be noted that in CBMC simulations, the equilibrium positions are determined by trial moves and a molecule can be "placed" at the centre of the pockets (the central region offers more room, and is about 6 Å in size) despite the fact that it might find it difficult to diffuse to this position due to the bottleneck at the mouth of the pockets caused by the narrow 4.6 Å window. It must be pointed out that no "blocking" strategy was used to prevent molecules to be placed in the pockets, because it is not known *a priori* which molecules will find it impossible to diffuse to the pocket regions. Furthermore, another possibility is for branched alkanes such as iC4, 2MB and neoP to preferentially adsorb near the mouths to the pockets.

Fig. 5 clearly shows that the tetrahedral pockets are the preferred adsorption sites at low loadings. However, the capacity of the pockets is rather limited and at a loading corresponding to 1 molecule per pocket, there is a tendency to populate the larger cages. Another noteworthy point is that the loading in the total pore space appears to increase sharply at the point where the pocket loading is 1 molecule; a similar sharp increase is observed

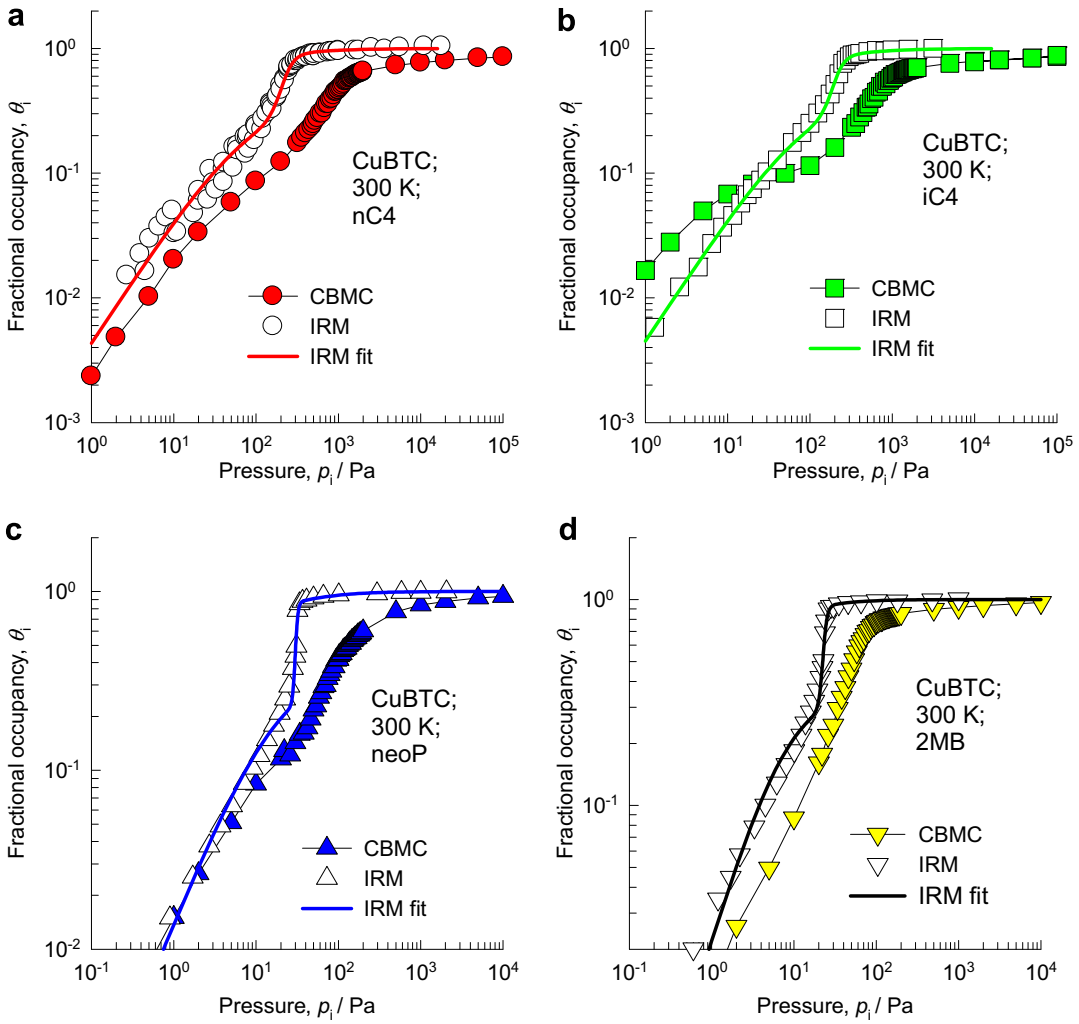

Fig. 8. Normalized adsorption isotherms (a) nC4, (b) iC4, (c) neoP, and (d) 2MB in CuBTC determined by IRM experiments, along with those determined by CBMC simulations. The IRM isotherm fits are also indicated by continuous solid lines; the parameters of the multi-site Sips isotherm are given in the Supplementary material.

in our IRM experiments for isotherms, to be discussed later in this paper. Our findings are consonant with earlier works for Ar adsorption in CuBTC [23–26]. The data in Fig. 5 provides an explanation for the inflection in $1/\Gamma_i$ at $q_i = 8$ observed in Fig. 4.

Since for loadings $q_i < 8$ molecules per unit cell, the alkanes prefer location in the pockets, the diffusion characteristics are dictated by hops across triangular windows of 4.6 Å and, consequently the diffusivities tend to be low. The diffusivities of molecules inhabiting the larger cages are about an order of magnitude higher because they correspond to hops across larger 9 Å windows. In the MD simulations the M–S diffusivities are calculated from the gathered statistics on individual molecular displacements

$$Đ_i = \frac{1}{6}\lim_{\Delta t\to\infty}\frac{1}{n_i}\frac{1}{\Delta t}\left\langle\left(\sum_{l=1}^{n_i}(r_{l,i}(t+\Delta t)-r_{l,i}(t))\right)^2\right\rangle \quad (5)$$

At $q_i < 8$ molecules per unit cell, most but not all molecules, are located in the pockets and the $Đ_i$ values reflect hops across narrow windows to pockets. As the molecules begin to populate the larger cages, the $Đ_i$ increase sharply till a maximum is reached, when the mean squared-displacements of the molecules within the pockets have a negligible influence on summation term in Eq. (5), and consequently on the $Đ_i$. For loadings higher than that corresponding to the maximum in $Đ_i$, the variation with q_i, follows the trend dictated by $1/\Gamma_i$–q_i, typical of diffusion in open structures such as FAU. The C5 isomers, neoP and 2MB are perhaps too bulky to diffuse across the narrow 4.6 Å windows, and these molecules do not exhibit the strong increase experienced by the other alkanes at loadings $q_i < 8$. Furthermore, for loadings below about 10 molecules per unit cell, the diffusivity values from MD simulations are too low to determine accurately. Therefore, a definitive statement about the diffusivity of neoP and 2MB at low loadings cannot be given; IRM diffusivity data measurements will be discussed below.

Methane, the most weakly confined alkane molecule, does not exhibit a pronounced inflection and the diffusion characteristic switches smoothly from "LTA-like" to "FAU-like" with increasing q_i; see Fig. 3a. MD simulations for diffusion of Ar, and Kr, show almost similar, smooth, transition in characteristics of diffusion as observed for C1. For molecules that are much smaller, e.g. Ne, He, and H_2 any segregation inside the pockets has very little impact on the loading dependence of $Đ_i$; see data in Supplementary material.

Another fingerprint of the preferential adsorption in the side pockets is obtained by examining the isosteric heat of adsorption, ΔH_{st}, for the various alkanes as a function of the total loading; the data obtained from CBMC simulations are presented in Fig. 7a. The data show the ΔH_{st} decreases with q_i till a loading of 8 molecules per unit cell is reached. When the energetically favored pocket regions are fully occupied ΔH_{st} increases with further increase in the loading, as the less-favorable sites in the larger cages become populated; this increase is only mild at first, followed by a sharper increase. The steep increase in ΔH_{st} for nC4, iC4, neoP, and 2MB at $q_i \approx 50$ molecules per unit cell is particularly worthy of note; this increase is due to adsorbate–adsorbate interactions becoming increasingly important as the large cages get filled up. Complementary results for ΔH_{st} have been reported for adsorption of Ar, ethene, and CO in CuBTC [15,23].

Correlation effects in diffusion are stronger for diffusion in larger channels, than for inter-cage hopping, one-molecule-at-a-time, from the pockets to the large cages. The strength of correlations can be quantified by the ratio of the M-S diffusivity $Đ_i$ to the self-exchange coefficient $Đ_{ii}$; data for C1 obtained from MD simulations are presented in Fig. 7b. We note again a sharp increase in $Đ_i/Đ_{ii}$ with loading for diffusion within the pockets; when the pockets are fully occupied the increase in $Đ_i/Đ_{ii}$ is significantly milder for diffusion across the larger 9 Å windows between large cages. Correlation effects will have a significant influence on the mixture diffusion characteristics.

We now seek experimental confirmation, using IRM, of the *hybrid* diffusion characteristics of alkanes, caused by the preferential adsorption in the side pockets at low loadings.

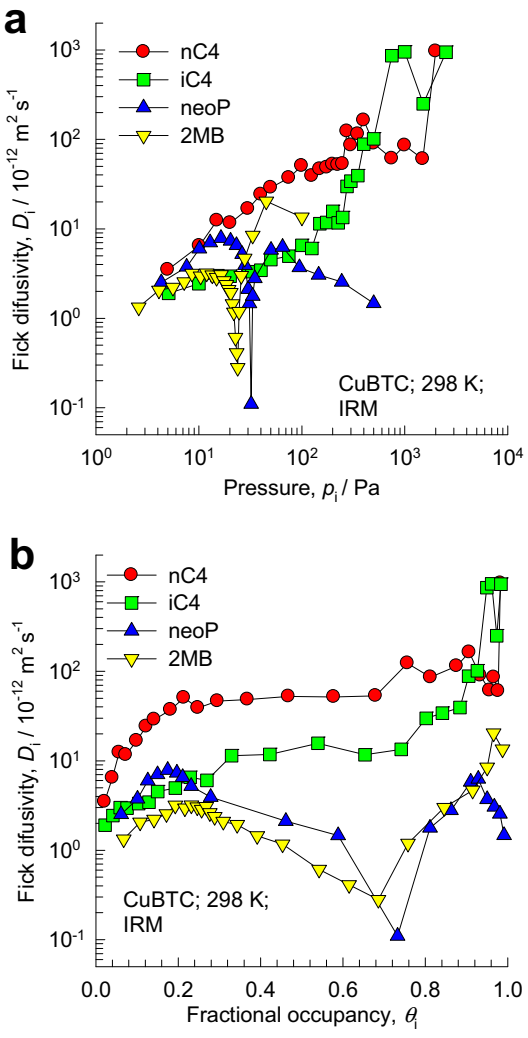

Fig. 9. Fick (or transport) diffusivity data for nC4, iC4, neoP, and 2MB in CuBTC, determined by IRM experiments plotted as function of the (a) pressure, and (b) fractional occupancy.

3. IRM experiments for adsorption and diffusion

Diffusion of C1, C2, and C3 is difficult to monitor using IRM because the uptake within single crystals is too fast for accurate determination of the diffusivities. For this reason, measurements were performed with butane isomers (nC4, and iC4), and pentane isomers (neoP, and 2MB). The adsorption isotherms are determinable, without further calibration, only in terms of relative amounts, and therefore the measured isotherms are reported in terms of fractional occupancies, θ_i, rather than in terms of molecular loadings q_i; see Fig. 8. All four measured isotherms show a sharp increase in the occupancy at pressures corresponding to the situation in which the pocket regions are fully loaded. In the case of neoP and 2MB, the increase is practically step-like, and is reminiscent of capillary condensation in *mesoporous* materials [50]. Step-like increases in adsorption isotherms have been reported

for CO_2 adsorption in IRMOF-1; the suggested cause of this are electrostatic interactions between CO_2 molecules [27]. Comparison of the measured isotherms with the CBMC simulated ones, show only a qualitative agreement. In particular the step-like increases, observed experimentally, are not anticipated by the simulations. A fundamental explanation for the step-like increase in the occupancy for neoP and 2MB in IRM experiments cannot, therefore, be given as yet; this aspect deserves further detailed investigation. For the present moment we shall attribute it to "phase transition", without further qualification.

The data on the measured Fick, or transport, diffusivities, D_i, obtained from fitting of the measured uptake curves are presented in Fig. 9a and b. We note that the D_i, for neoP and 2MB decreases sharply at "phase transition".

In order to calculate the M–S $Đ_i$, we need to determine the thermodynamic correction factor Γ_i by fitting the measured isotherms; these do not lend themselves to fitting with the usual Langmuir type isotherm. We found that a multi-site Sips isotherm [50] is required for accurate fitting purposes

$$q_i = q_{i,A,\mathrm{sat}} \frac{b_{i,A} p_i^{\nu_{i,A}}}{1 + b_{i,A} p_i^{\nu_{i,A}}} + q_{i,B,sat} \frac{b_{i,B} p_i^{\nu_{i,B}}}{1 + b_{i,B} p_i^{\nu_{i,B}}} \tag{6}$$

On the basis of the insights provided by CBMC simulations we can identify these two sites as being (A) pocket regions, and (B) larger cages; the fitted curves are also indicated in Fig. 8. Fig. 10 compares the $1/\Gamma_i$ obtained from the fitted isotherms with the corresponding values from CBMC simulations. For nC4 and iC4, there is qualitative agreement between the inflection behaviour of the two sets, as well as the overall trend. The experimental data for all four molecules exhibit inflections at $\theta_i \approx 0.2$, slightly higher than the occupancies at which the CBMC simulations show inflection. The origin of the inflection is most likely caused due to the same reasons as discussed earlier, i.e. due to preferential location at the pocket regions at low loadings. For neoP and 2MB the experimental $1/\Gamma_i$ values are significantly higher than unity for the range of occupancies where phase transition occurs. The CBMC simulations do not account for the experimentally observed phase transition, and the simulated values of $1/\Gamma_i \leqslant 1$.

The data on the M–S $Đ_i$, backed out from the Fick D_i, are shown in Fig. 11, along with the corresponding $1/\Gamma_i$. For nC4 and iC4 the occupancy dependence of $Đ_i$ closely mirrors that of $1/\Gamma_i$ for $\theta_i > 0.3$, in *qualitative* agreement with the MD simulation results presented in Fig. 4, suggesting that at higher occupancies, diffusion is predominantly in the larger cages, and across large windows. For $\theta_i < 0.3$, the sharp increase in the $Đ_i$ with increasing θ_i is also in

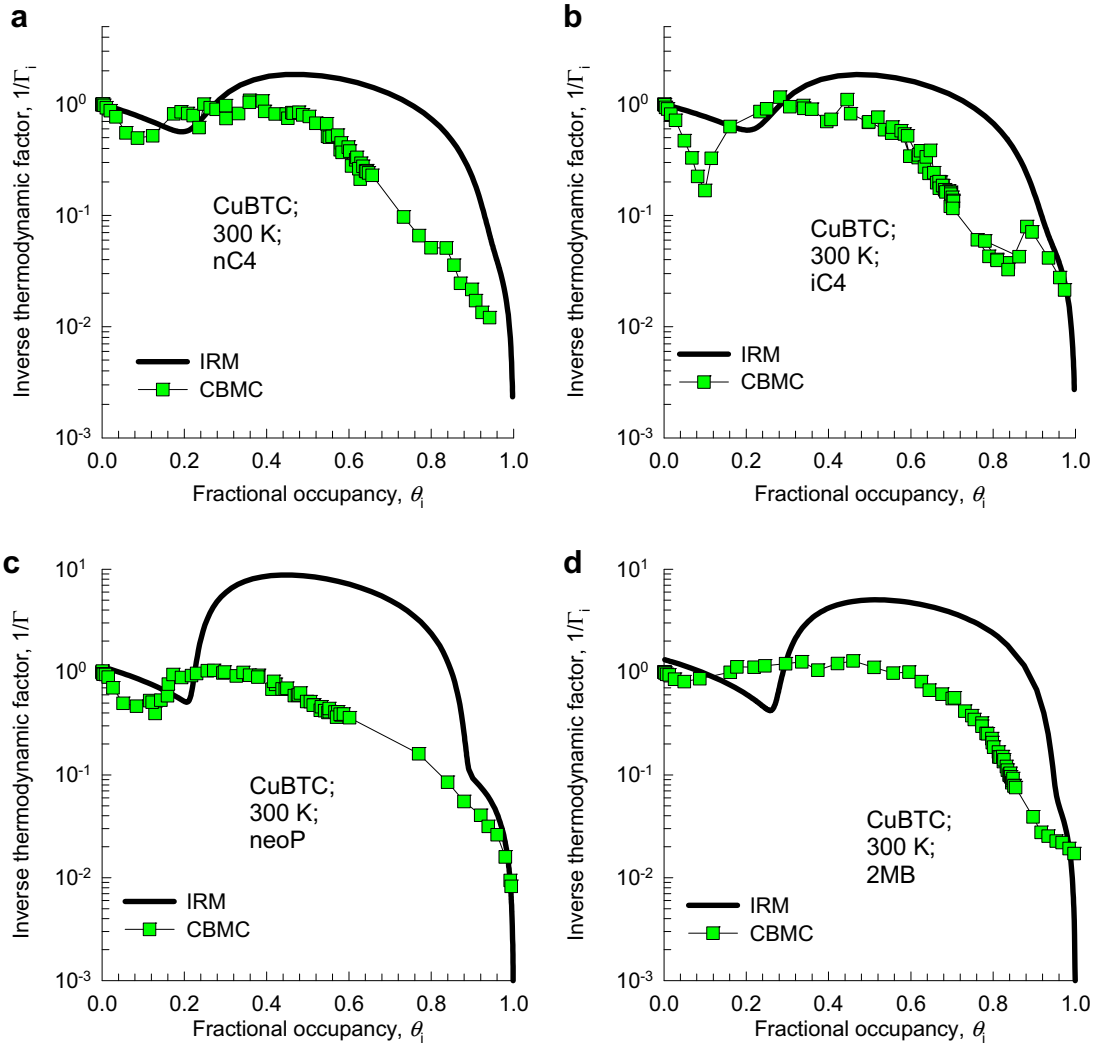

Fig. 10. Variation of inverse thermodynamic factor $1/\Gamma_i$ of (a) *n*-butane, (b) iso-butane, (c) 2,2- dimethylpropane, and (d) 2-methylbutane with occupancy obtained from IRM isotherm fits (continuous solid lines), and CBMC simulations (square symbols).

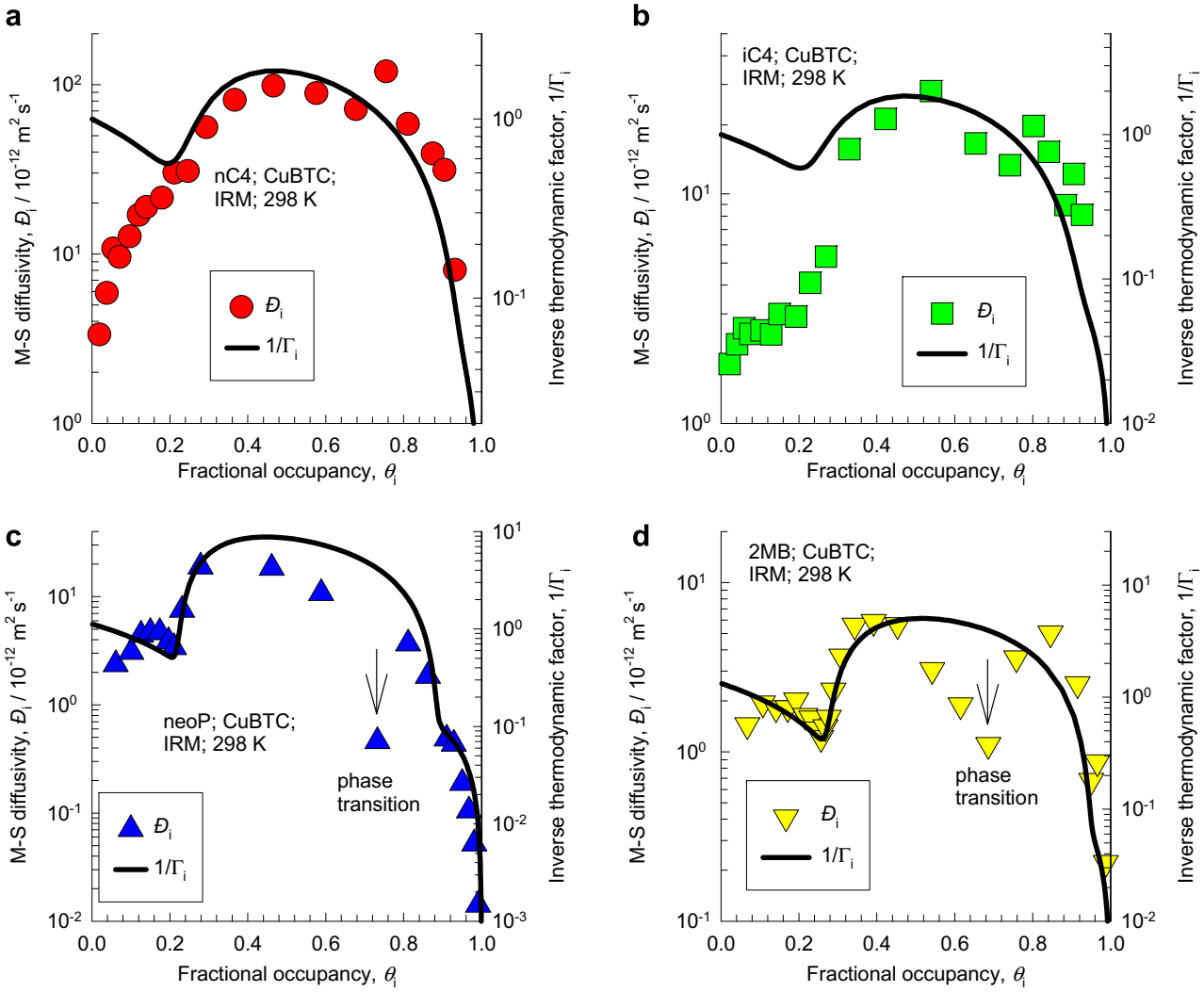

Fig. 11. Occupancy dependence of the Maxwell–Stefan diffusivity $Đ_i$, and the inverse thermodynamic factor $1/\Gamma_i$ in CuBTC of (a) *n*-butane, (b) iso-butane, (c) 2,2-dimethylpropane, and (d) 2-methylbutane. The symbols represent $Đ_i$ values backed out from IRM experiments, and the continuous solid lines are derived from IRM isotherm fits.

conformity with the MD simulation results, and is due to transition from hops across narrow windows to pockets, to hops across large windows.

For neoP and 2MB, the variation of $Đ_i$ with increasing θ_i follows the $1/\Gamma_i$–θ_i trend only in regions *outside* the phase transition region. For occupancies $0.4 < \theta_i < 0.8$, corresponding to the near-vertical branch of the isotherms for neoP and 2MB, the $Đ_i$ is significantly lower than the trend line following $1/\Gamma_i$. It must be emphasised that for the range $0.4 < \theta_i < 0.8$, the calculation of the $1/\Gamma_i$ is extremely sensitive to the precise choice of the isotherm fit parameters; a small change in parameter values can lead to variations in $Đ_i$ by a factor of about five. Outside the region $0.4 < \theta_i < 0.8$, the $Đ_i$–θ_i dependence is in good *qualitative* agreement with $1/\Gamma_i$–θ_i; these results are also in harmony with those obtained from MD simulations; cf. Fig. 4. For the range of occupancies $0 < \theta_i < 0.2$, the increase in the $Đ_i$ for neoP and 2MB is much less steep than for nC4 and iC4 and this indicates that neoP and 2MB find it difficult to diffuse into the side pockets.

The absolute values of the $Đ_i$ calculated from MD tend to be about two orders of magnitude higher than those obtained from experiment. The MD simulated diffusivities are extremely sensitive to the choice of the Lennard–Jones σ parameter; a 10% increase in this parameter can lead to a lowering in the diffusivities by two orders of magnitude in zeolites [44]; a similar result holds for MOFs [38]. Furthermore, in our simulations we have assumed a rigid lattice framework; recent published work show that whether the framework lattice is assumed to be rigid or flexible, has a significant, about one order of magnitude, influence on the diffusivities [51]. Nevertheless, it is remarkable to note that several of the key features of adsorption and diffusion anticipated by the simulations, in particular the *hybrid* character of the $Đ_i$–θ_i dependence, is also confirmed experimentally.

4. Conclusions

The adsorption and diffusion characteristics of alkanes in CuBTC have been investigated using a combination of molecular simulations and IRM. The following major insights emerge from our studies.

(1) The adsorption isotherms exhibit inflection characteristics due to the strong preference for adsorption within, and in the regions close to the mouths of tetrahedral pockets. For alkanes with 2 or more C atoms, CBMC simulations show that inflection occurs at 8 molecules per unit cell, corresponding

to a loading of 1 molecule per pocket; for C4 and C5 alkanes, saturation of the pockets occur at this loading. Extra molecules can only be lodged in the larger cages.

(2) For neoP, and 2MB the adsorption isotherms from IRM show step increase in the loading at certain pressures; the precise reasons for this "phase transition" need further elucidation.

(3) Both MD simulations and IRM experiments show that the loading dependence of the M–S $Đ_i$ has a hybrid character. At high occupancies, corresponding to location of molecules in the larger cages, the $Đ_i$–θ_i dependence closely follows that of $1/\Gamma_i$–θ_i; this behavior is similar to that in FAU zeolite. For occupancies lower than that corresponding to saturation of the tetrahedral pockets the $Đ_i$ increases sharply with θ_i, because the diffusivities undergo transition from hops across narrow windows to hops across larger windows. The C5 isomers, neoP and 2MB, are too bulky to diffuse across the windows to the pockets and for these molecules there is no "LTA-like" increase in $Đ_i$ at low occupancies. In the IRM experiments phase transition is experienced for the occupancy range $0.4 < \theta_i < 0.8$; in this case the $Đ_i$ is significantly lowered and this results are not matched by molecular simulations.

(4) Though molecular simulations provide a fundamental background for the hybrid character of diffusion, *quantitative* data for both adsorption and diffusion are not provided. In particular, the phase transition observed for neoP and 2MB are not reproduced. There is a need for further improvement in the force fields in order to provide quantitative predictions.

This paper highlighted the rich features of adsorption and diffusion of alkanes in CuBTC. Our study provides a platform for further research on diffusion in CuBTC and will aid in separation technology development using MOFs.

Acknowledgments

Financial support by *Deutsche Forschungsgemeinschaft* (Mercator Professorship for RK, International Research Group "Diffusion in Zeolites" and International Research Training Group "Diffusion in Porous Materials"), *Max-Buchner-Forschungsstiftung* and *Fonds der Chemischen Industrie* is gratefully acknowledged.

Appendix A. Supplementary material

Supplementary data associated with this article can be found, in the online version, at doi:10.1016/j.micromeso.2008.06.003.

References

[1] O.M. Yaghi, M. O'Keeffe, N.W. Ockwig, H.K. Chae, M. Eddaoudi, J. Kim, Nature 423 (2003) 705.
[2] J.L.C. Rowsell, O.M. Yaghi, Micropor. Mesopor. Mater. 73 (2004) 3.
[3] O.M. Yaghi, Nature Mater. 6 (2007) 92.
[4] R.Q. Snurr, J.T. Hupp, S.T. Nguyen, A.I.Ch.E.J. 50 (2004) 1090.
[5] L. Bastin, P.S. Bárcia, E.J. Hurtado, J.A.C. Silva, A.E. Rodrigues, B. Chen, J. Phys. Chem. C 112 (2008) 1575.
[6] L. Pan, D.H. Olson, L.R. Ciemnolonski, R. Heddy, J. Li, Angew. Chem. Int. Ed. 45 (2006) 616.
[7] P.S. Bárcia, F. Zapata, J.A.C. Silva, A.E. Rodrigues, B. Chen, J. Phys. Chem. B 111 (2008) 6101.
[8] B. Chen, C. Liang, J. Yang, D.S. Contreras, Y.L. Clancy, E.B. Lobkovsky, O.M. Yaghi, S. Dai, Angew. Chem. Int. Ed. 45 (2006) 1590.
[9] L. Pan, B. Parker, X. Huang, D.H. Olson, J.Y. Lee, J. Li, J. Am. Chem. Soc. 128 (2006) 4180.
[10] D.N. Dybtsev, H. Chun, S.H. Yoon, D. Kim, K. Kim, J. Am. Chem. Soc. 126 (2004) 32.
[11] V. Finsy, H. Verelst, L. Alaerts, D. De Vos, P.A. Jacobs, G.V. Baron, J.F.M. Denayer, J. Am. Chem. Soc. 130 (2008) 7110.
[12] L. Alaerts, C.E.A. Kirschhock, M. Maes, M. van der Veen, V. Finsy, A. Depla, J.A. Martens, G.V. Baron, P.A. Jacobs, J.F.M. Denayer, D. De Vos, Angew. Chem. Int. Ed. 46 (2007) 4293.
[13] Q.M. Wang, D. Shen, M. Bülow, M.L. Lau, S. Deng, F.R. Fitch, N.O. Lemcoff, J. Semanscin, Micropor. Mesopor. Mater. 55 (2002) 217.
[14] L. Zhang, Q. Wang, T. Wu, Y.C. Liu, Chem. Eur. J. 13 (2007) 6387.
[15] S. Wang, Q. Yang, C. Zhong, Sep. Purif. Technol. 60 (2008) 30.
[16] Q. Yang, C. Xue, C. Zhong, J.F. Chen, A.I.Ch.E.J. 53 (2007) 2832.
[17] Q. Yang, C. Zhong, J. Phys. Chem. B 110 (2006) 17776.
[18] S. Keskin, D.S. Sholl, J. Phys. Chem. C 111 (2007) 14055.
[19] J. Jiang, S.I. Sandler, Langmuir 22 (2006) 5702.
[20] R. Babarao, Z. Hu, J. Jiang, S. Chempath, S.I. Sandler, Langmuir 23 (2007) 659.
[21] A. Kondo, H. Noguchi, L. Carlucci, D.M. Proserpio, G. Ciani, H. Kajiro, T. Ohba, H. Kanoh, K. Kaneko, J. Am. Chem. Soc. 129 (2007) 12362.
[22] D. Dubbeldam, H. Frost, K.S. Walton, R.Q. Snurr, Fluid Phase Equilibr. 261 (2007) 152.
[23] V. Krungleviciute, K. Lask, L. Heroux, A.D. Migone, J.Y. Lee, J. Li, A.I. Skoulidas, Langmuir 23 (2007) 3106.
[24] V. Krungleviciute, K. Lask, A.D. Migone, J.Y. Lee, J. Li, A.I.Ch.E.J. 54 (2008) 918.
[25] A. Vishnyakov, P.I. Ravikovitch, A.V. Neimark, M. Bülow, Q.M. Wang, Nano Lett. 3 (2003) 713.
[26] A.I. Skoulidas, J. Am. Chem. Soc. 126 (2004) 1356.
[27] K.S. Walton, A.R. Millward, D. Dubbeldam, H. Frost, J.J. Low, O.M. Yaghi, R.Q. Snurr, J. Am. Chem. Soc. 130 (2008) 406.
[28] D.B. Shah, C.J. Guo, D.T. Hayhurst, J. Chem. Soc.-Faraday Trans. 91 (1995) 1143.
[29] H. Jobic, C. Laloué, C. Laroche, J.M. van Baten, R. Krishna, J. Phys. Chem. B 110 (2006) 2195.
[30] C. Chmelik, L. Heinke, J. Kärger, D.B. Shah, W. Schmidt, J.M. van Baten, R. Krishna, Chem. Phys. Lett. 459 (2008) 141.
[31] F. Stallmach, S. Gröger, V. Künzel, J. Kärger, O.M. Yaghi, M. Hesse, U. Müller, Angew. Chem. Int. Ed. 45 (2006) 2123.
[32] P. Kortunov, L. Heinke, M. Arnold, Y. Nedellec, D.J. Jones, J. Caro, J. Kärger, J. Am. Chem. Soc. 129 (2007) 8041.
[33] A.I. Skoulidas, D.S. Sholl, J. Phys. Chem. B 109 (2005) 15760.
[34] R. Krishna, J.M. Van Baten, Chem. Eng. Sci. 63 (2008) 3120.
[35] S.S.Y. Chui, S.M.F. Lo, J.P.H. Charmant, A.G. Orpen, I.D. Williams, Science 283 (1999) 1148.
[36] C. Chmelik, A. Varma, L. Heinke, D.B. Shah, J. Kärger, F. Kremer, U. Wilczok, W. Schmidt, Chem. Mater. 19 (2007) 6012.
[37] L. Heinke, C. Chmelik, P. Kortunov, D.M. Ruthven, D.B. Shah, S. Vasenkov, J. Kärger, Chem. Eng. Technol. 30 (2007) 995.
[38] J.A. Greathouse, M.D. Allendorf, J. Phys. Chem. C 112 (2008) 5795.
[39] A.K. Rappé, C.J. Casewit, K.S. Colwel, W.A. Goddard, W.M. Skiff, J. Am. Chem. Soc. 114 (1992) 10024.
[40] S.L. Mayo, B.D. Olafson, W.A. Goddard, J. Phys. Chem. 94 (1990) 8897.
[41] H. Chen, D.S. Sholl, Langmuir 22 (2006) 709.
[42] R. Krishna, J.M. van Baten, Chem. Eng. J. 133 (2007) 121.
[43] R. Krishna, J.M. van Baten, Chem. Phys. Lett. 420 (2006) 545.
[44] R. Krishna, J.M. van Baten, Micropor. Mesopor. Mater. 109 (2008) 91.
[45] E. Beerdsen, D. Dubbeldam, B. Smit, Phys. Rev. Lett. 95 (2005) 164505.
[46] E. Beerdsen, D. Dubbeldam, B. Smit, Phys. Rev. Lett. 96 (2006) 044501.
[47] R. Krishna, J.M. van Baten, Sep. Purif. Technol. 61 (2008) 414.
[48] J. Caro, M. Bülow, W. Schirmer, J. Kärger, W. Heink, H. Pfeifer, J. Chem. Soc. Faraday Trans. 81 (1985) 2541.
[49] R. Krishna, J.M. van Baten, Chem. Eng. Technol. 30 (2007) 1235.
[50] J.W. Lee, W.G. Shim, H. Moon, Micropor. Mesopor. Mater. 73 (2004) 109.
[51] S. Amirjalayer, M. Tafipolsky, R. Schmid, Angew. Chem. Int. Ed. 46 (2007) 463.

Supplementary Material to accompany:

Adsorption and diffusion of alkanes in CuBTC crystals investigated using infra-red microscopy and molecular simulations

C. Chmelik[(1)], J. Kärger[(1)], M. Wiebcke[(2)], J. Caro[(3)], J.M. van Baten[(4)],

and R. Krishna[(4)]*

[(1)] Abteilung Grenzflächenphysik, Universität Leipzig, Linnéstrasse 5, 04103 Leipzig, Germany

[(2)] Leibniz University of Hannover, Institut für Anorganische Chemie,

Callinstrasse 9, D-30167 Hannover, Germany

[(3)] Leibniz University of Hannover, Institute of Physical Chemistry and Electrochemistry,

Callinstrasse 3-3a, D-30167 Hannover, Germany

[(4)] Van 't Hoff Institute for Molecular Sciences, University of Amsterdam, Nieuwe Achtergracht 166,

1018 WV Amsterdam, The Netherlands

Appendix A1: Synthesis and General Characterization

1. Synthesis

CuBTC was synthesized solvothermally in ethanol-water solution according to reported methods [1-3]. A comparatively high temperature of 150 °C was found to be necessary to produce single crystals of sufficient size suitable for the IRM studies. It is well known that such high temperatures result in the formation of by-products, e.g., Cu_2O.

In a typical synthesis, 3.6 mmol of $Cu(NO_3)_2 \cdot 3H_2O$ (0.86 g) and 2.0 mmol of benzene-1,3,5-tricarboxylic acid (0.42 g) were dissolved in 18 mL of EtOH-H_2O (67 : 33) solution. The solution was charged into a Teflon-lined autoclave and kept in an oven at 150 °C under static conditions and autogeneous pressure for 14 h. The crystalline product was separated by filtration, washed with EtOH and H_2O and dried in air.

Inspection under a polarizing microscope revealed that the product contained large turquoise-blue CuBTC crystals of various shapes (up to ca. 60 μm in size) and minor amounts of red (probably Cu_2O) particles as well as colourless, birefrigent particles of an as yet unknown phase. A powder X-ray diffraction (XRD) pattern taken from the product (Fig. 1) revealed high crystallinity. All but one reflection were cleanly indexed on a face-centered cubic lattice (space group Fm3m) with a lattice constant of a = 26.299(3) Å. Cu_2O does not show up in the XRD pattern; the unindexed reflection may be due to the colourless impuritiy phase seen under the microscope. A thermogravimetry (TG) and difference thermal analysis (DTA) measurement was performed simultaneously on a sample of the product in air atmosphere. Three distinct weight losses are seen on the TG trace (Fig. 2). The final residue was identified as CuO by XRD. If the three weight losses are assigned, respectively, to the escape of water molecules (-32 %), EtOH molecules (-5 %) and combustion products of the organic

linker molecules (-33 %), a formulation of $[Cu_3(BTC)_2 \cdot 3H_2O] \cdot 6.2H_2O \cdot 0.5EtOH$ is obtained for our product.

2. Methods

Powder XRD patterns were recorded on a Stoe STADI-P diffractometer in transmission geometry using $CuK_{\alpha 1}$ radiation (λ = 1.54060 Å, bent Ge(111) monochromator). Simultaneous TG/DTA measurements were performed on a Netzsch thermal analyzer 429. For this purpose, samples were filled into alumina crucibles and heated in flowing air at a rate of 5 °C/min up to 1000 °C.

3. References

[1] Q.M. Wang, D. Shen, M. Bülow, M.L. Lau, S. Deng, F.R. Fitch, N.O. Lemcoff, J. Semanscin, Metallo-organic molecular sieve for gas separation and purification, Microporous Mesoporous Mater. 55 (2002) 217.

[2] K. Schlichte, T. Kratzke, S. Kasken, Improved synthesis, thermal stability and catalytic properties of the metal-organic framework compound $Cu_3(BTC)_2$, Microporous Mesoporous Mater. 73 (2004) 81.

[3] L. Alaerts, E. Séguin, H. Poelman, F. Thibault-Starzyk, P.A. Jacobs, D.E. de Vos, Probing the Lewis Acidity and Catalytic Activity of the Metal-Organic Framework $[Cu_3(btc)_2]$ (BTC=Benzene-1,3,5-tricarboxylate), Chem. Eur. J. 12 (2006) 7353.

[4] S. S.-Y. Chui, S. M.-F. Lo, J.P.H. Charmant, A.G. Orpen, I.D. Williams, A Chemically Functionalizable Nanoporous Material $[Cu_3(TMA)_2(H_2O)]_n$, Science 283 (1999) 1148.

4. Captions for Figures

Figure 1. Experimental powder XRD pattern (blue) of as-synthesized CuBTC. An XRD pattern (red) was simulated using crystal structure data (including guest water molecules) taken from ref. [4]. One reflection (marked by *) in the experimental pattern could not be indexed on a face-centered cubic lattice.

Figure 2. TG/DTA curves for as-synthesized CuBTC.

Figure 1

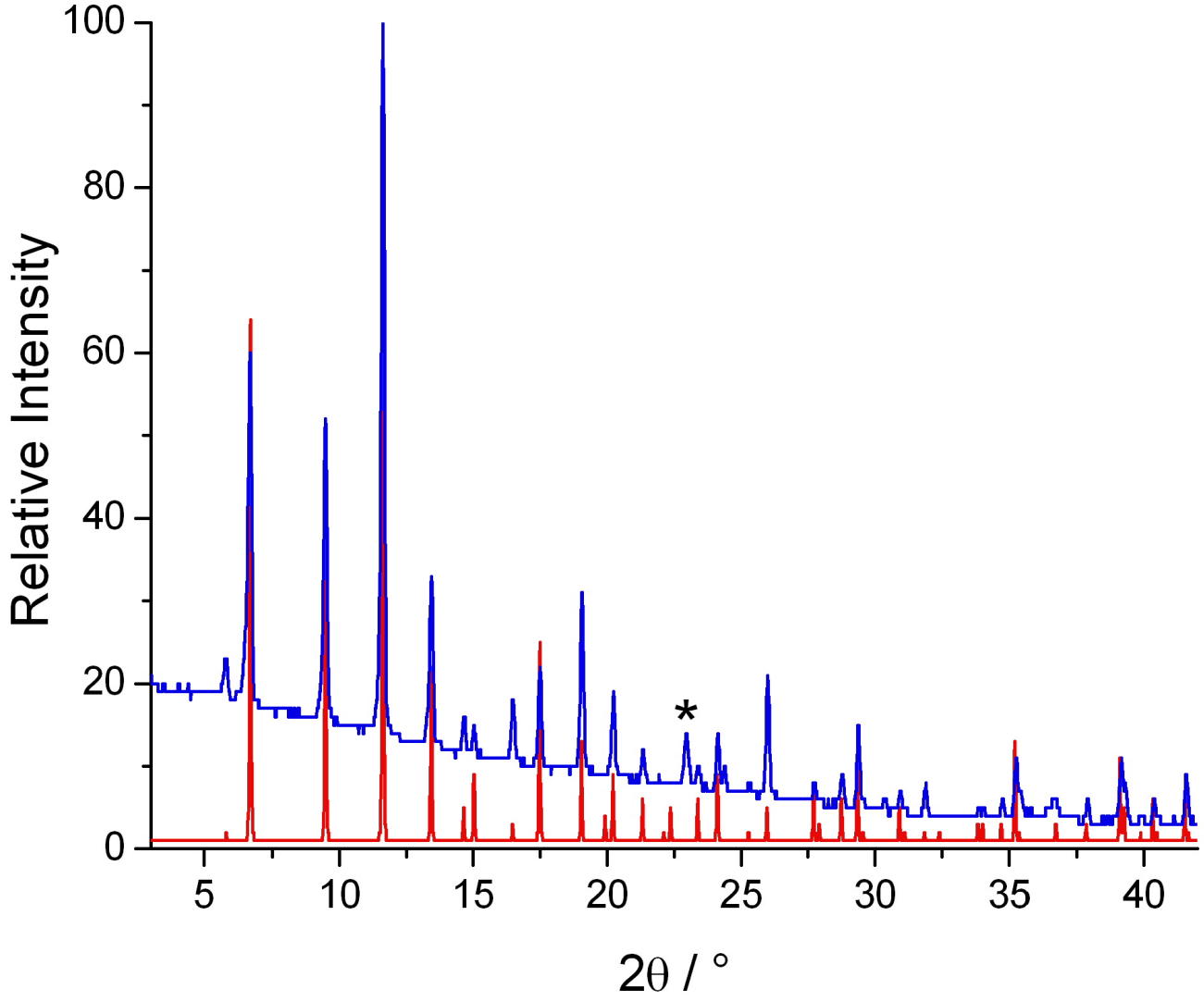

Figure 2

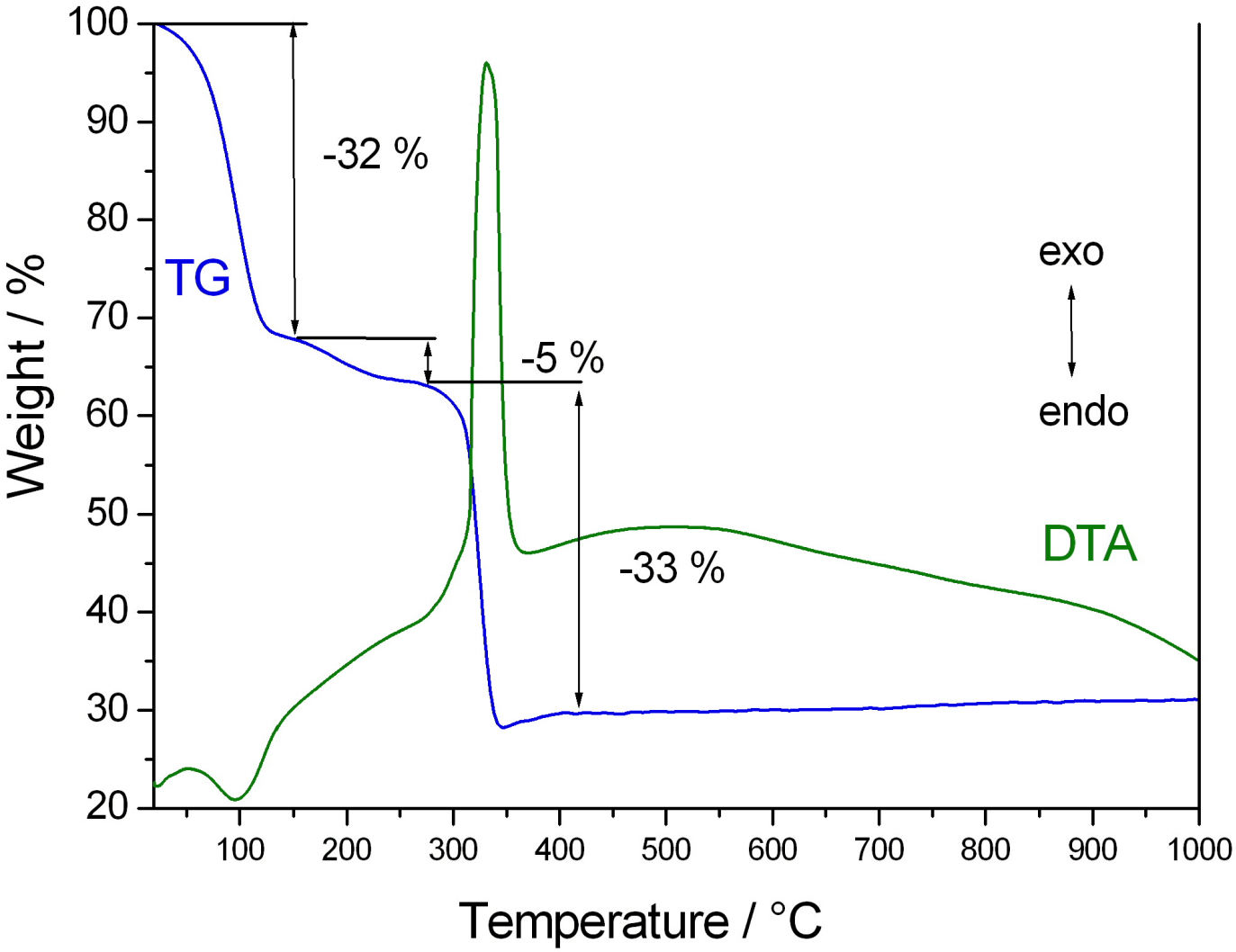
100
90
80
70
60
50
40
30
20
Weight / %
TG
-32 %
-5 %
-33 %
exo
endo
DTA
100
200
300
400
500
600
700
800
900
1000
Temperature / °C

Appendix A2: Experimental set-up, experimental procedure, diffusivity determinations

1. Experimental Method

The IR microscopy (IRM) experimental set-up comprises an IR microscope HYPERION 3000 coupled with an IR spectrometer VERTEX 80v (both *Bruker Optics*) and a static vacuum system. The schematics of the IRM set-up is illustrated in Figure 1.

Prior to the measurements, several hundred crystals were filled into the IR cell and activated as follows. At first, the IR cell was evacuated at room temperature for about 6 h. Then, the crystals were heated with a rate of 0.5 $K \cdot min^{-1}$ up to 383 K and kept for 6 h at this elevated temperature under high vacuum. Directly after activation the IR cell is fixed on the motorized sample platform of the microscope.

The IR microscope can be operated in optical mode or in IR mode. In the viewing mode, one particular MOF crystal is selected for the measurement by moving the platform and adjusting the aperture appropriately (see Figure 1). Since the panels of the aperture are not transparent for IR light, only the rectangular region in the centre is scanned by IR light during the measurements. The size of the aperture was typically set to 120×120 μm^2. All IR measurements were preformed at room temperature, i.e. at 298 K, in the IR-transmittance mode of the microscope.

The attached vacuum system consists of pressure sensors, turbo-molecular pump, gas bottle with the sorbate and stock volume. It allows us to control the gas phase composition in the IR cell. Step changes in the gas phase surrounding the crystals at time $t = 0$ were used to initiate the adsorption or desorption experiments.

To monitor the uptake or release of the guest molecules within the crystal, a series of absorption spectra was recorded with a time resolution between 0.1 and 1.0 s and a spectral resolution of 16 cm^{-1}. According to the Beer-Lambert law

$$A = \log\left(I_0/I\right) = \alpha_{\mathrm{m}} \cdot c \cdot d \quad , \tag{1}$$

the change in the concentration c of the guest molecules in the crystals is proportional to the area under the characteristic absorption bands, viz. the C-H stretching bands. Here, A represents the absorbance, I and I_0 denote the intensities of the sample scan and background scan, respectively, α_{m} is the coefficient of the extinction in molar units and d symbolizes the thickness of the medium. The area under the C-H bands was calculated between 2830 and 2990 cm^{-1} using a straight baseline between 2780 and 3015 cm^{-1} (see Figure 2). Without further calibration, the concentration can be obtained in relative units, only.

For each adsorption or desorption step, the obtained relative concentration was normalized and plotted against time to obtain the integral uptake curve. The obtained uptake curves were fitted by an adequate solution of Fick's second law to calculate the Fick , or transport, diffusivity D [1-3]. Finally, the concentration dependence of the Fick diffusivity D was obtained from a series of small loading steps.

2. Determination of Fick diffusivity

For each loading step, the uptake curves were normalized to go from 0 at $t = 0$ to unity at equilibrium. The curves were fitted by the solution of Fick's second law for uptake in spherical shaped particles with three-dimensional pore network [1] to obtain the transport (Fick) diffusivity D:

$$A_{norm} \equiv \frac{A_t - A_0}{A_\infty - A_0} = 1 - \frac{6}{\pi^2}\sum_{n=1}^{\infty}\frac{1}{n^2}\exp\left(-\frac{n^2\pi^2 Dt}{r_{Sph}{}^2}\right) \quad . \tag{2}$$

r_{sph} is the equivalent sphere radius, calculated for a sphere with the same surface –to-volume ratio as the investigated crystal. The dimensions of the investigated crystals were typically in the range of $60 \times 80 \times 20$ μm^3, resulting in $r_{\mathrm{sph}} \approx 19$ µm. A_0, A_t, and A_∞ represent the absorbance at time 0, t and ∞,

respectively, leading to the normalized absorbance A_{norm}, which reflects the fractional uptake at time t. For fitting the data the sum was calculated up to the 100th term.

3. Experimental Data

Equilibrium Isotherm

Single-crystal sorption isotherms were recorded for different, individual crystals for each sorbate molecule by changing the gas phase pressure in small steps between vacuum and 20 kPa. At sorption equilibrium, the relative concentration was measured for each step. The spectra were recorded with a spectral resolution of 4 cm^{-1} by averaging over 64 scans. The values of relative concentration were normalized with respect to the saturation loading to obtain the fractional occupancy θ_i. The fractional occupancy reaches from 0 at zero loading to unity at saturation loading. By plotting these values against pressure the sorption equilibrium isotherms were obtained.

Isotherm measurements were repeated for different sorbates on different MOF crystals. Clearly, the magnitude of the detected relative concentrations depends also on the size of the chosen crystals (see Eq. (1)). By calculation of the fractional occupancy the influence of the size differences was compensated, allowing for a direct comparison of the isotherms. After this procedure, all isotherms measured for the same sorbate showed good agreement.

Within the uncertainty of the measurements no differences between the adsorption and desorption branches could be observed.

Table 1 summarizes the fits of the (normalized) IRM isotherms using multi-site Sips model.

Uptake Measurements

The uptake kinetics of *n*-butane (nC4), *iso*-butane (iC4), 2,2-dimethylpropane (neoP – neopentane) and 2-methylbutane (2MB) were measured for many differential loading steps. The gas phase pressure was varied in a range from 2 Pa to 2 kPa, covering a loading range of θ_i from almost zero to more than

0.9. The loading steps covered in the uptake experiments were small enough to practically ensure the condition of a constant diffusivity implied in Eq. (2). Some typical examples for experimentally measured uptake curves fitted using Eq. (2) are shown in Figure 3.

4. References

[1] J. Crank, *Mathematics of Diffusion*, Oxford University Press, 2nd Edition, 1975.

[2] H.G. Karge and W. Niessen; *Catal. Today* **8** (1991) 451-465.

[3] J. Kärger and D.M. Ruthven, *Diffusion in Zeolites and Other Microporous Solids*; Wiley & Sons, New York, 1992.

Table 1. Parameters in the multi-site Sips isotherm. The saturation capacities are normalized values, adding to unity.

$$q_i = q_{i,A,sat}\frac{b_{i,A}p_i^{\nu_{i,A}}}{1+b_{i,A}p_i^{\nu_{i,A}}} + q_{i,B,sat}\frac{b_{i,B}p_i^{\nu_{i,B}}}{1+b_{i,B}p_i^{\nu_{i,B}}}$$

Molecule	$q_{sat,A}$	b_A	ν_A	$q_{sat,B}$	b_B	ν_B
nC4	0.4	0.01096	1	0.6	7.4×10^{-15}	6
iC4	0.44	0.01033	1	0.56	2.34×10^{-15}	6.308
2MB	0.37	0.0629	1.325	0.63	1.04×10^{-24}	17.54
neoP	0.37	0.0389	1.124	0.63	2.27×10^{-41}	27.32

Captions for Figures

Figure 1. Photograph of the Infra-Red microscopy (IRM) experimental set-up. The upper-right picture depicts the MOF crystal observed with the microscope operated in the viewing mode. The bottom-right picture is a close-up of the motorized platform on which the cell with crystal inside is placed. The crystal size chosen for experimental study is 100 μm in size (longest distance along crystal).

Figure 2. Absorption spectra of 2,2-dimethylpropane (neoP) recorded with time progression. The area under the C-H stretching band between wave numbers of 2830 and 2990 cm^{-1} is proportional to concentration of neoP within the crystal.

Figure 3. Comparison of normalized uptake curves determined by IR microscopy with best fits using Eq. (2) for different loading steps of a) n-butane, b) iso-butane, c) 2,2-dimethylpropane, and d) 2-methylbutane.

Figure 1

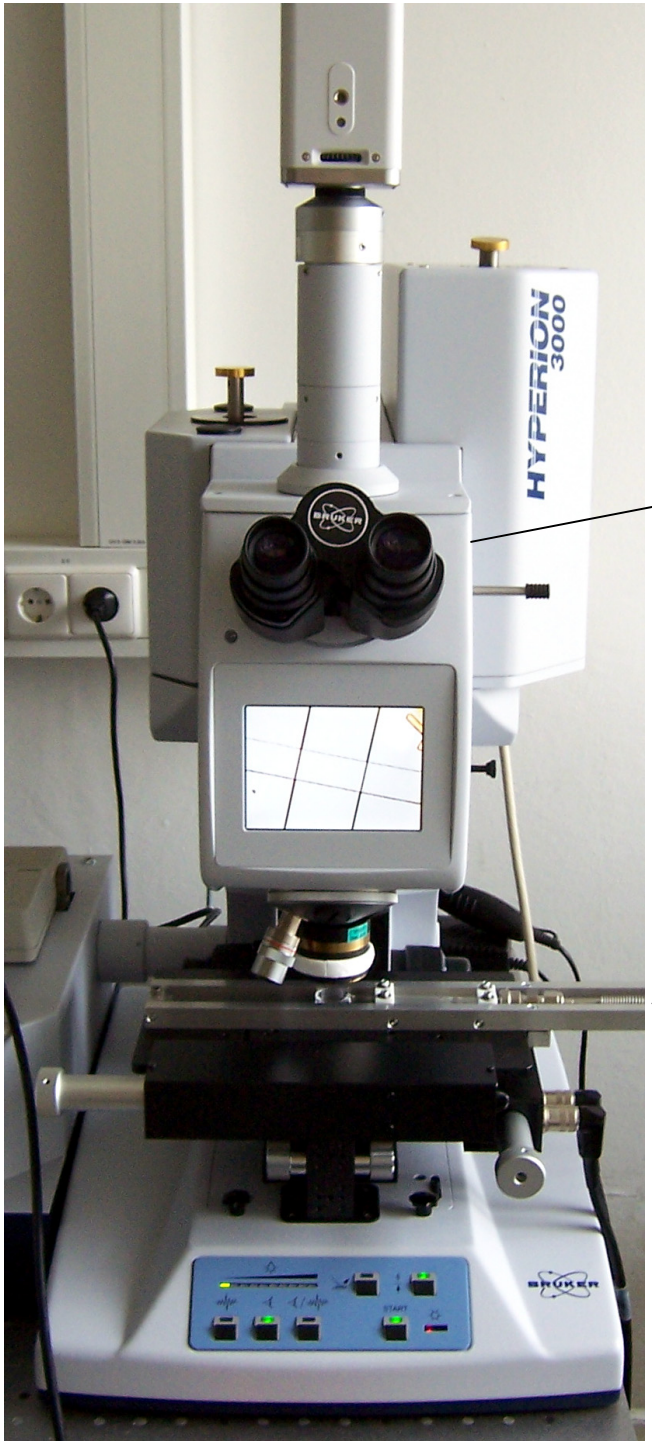

Viewing mode of microscope for adjusting the aperture to an individual crystal

IR cell mounted on motorized platform

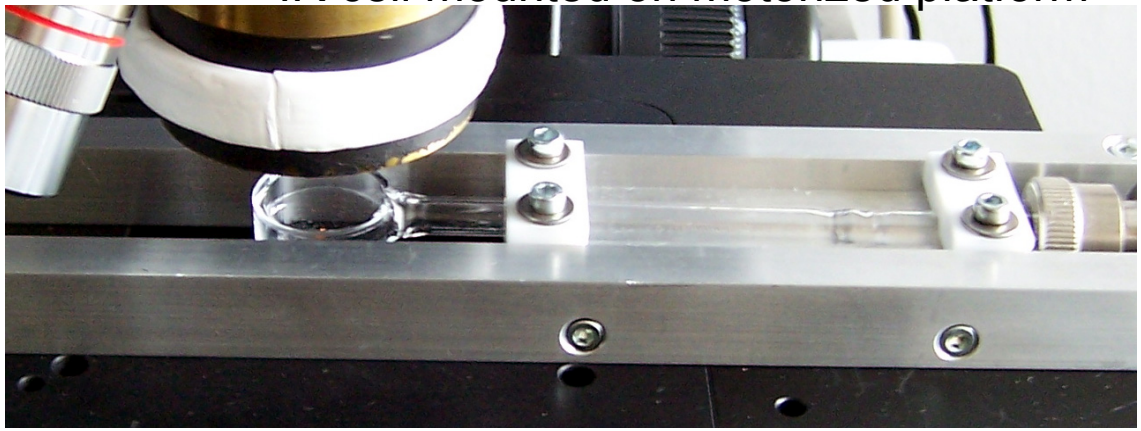

Figure 2

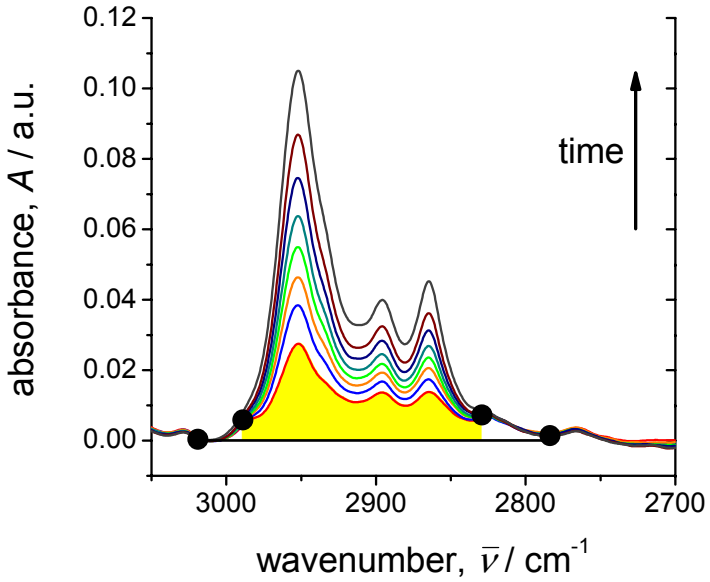
0.12
0.10
0.08
0.06
0.04
0.02
0.00
absorbance, A / a.u.
time
3000
2900
2800
2700
wavenumber, $\bar{\nu}$ / cm^{-1}

Figure 3

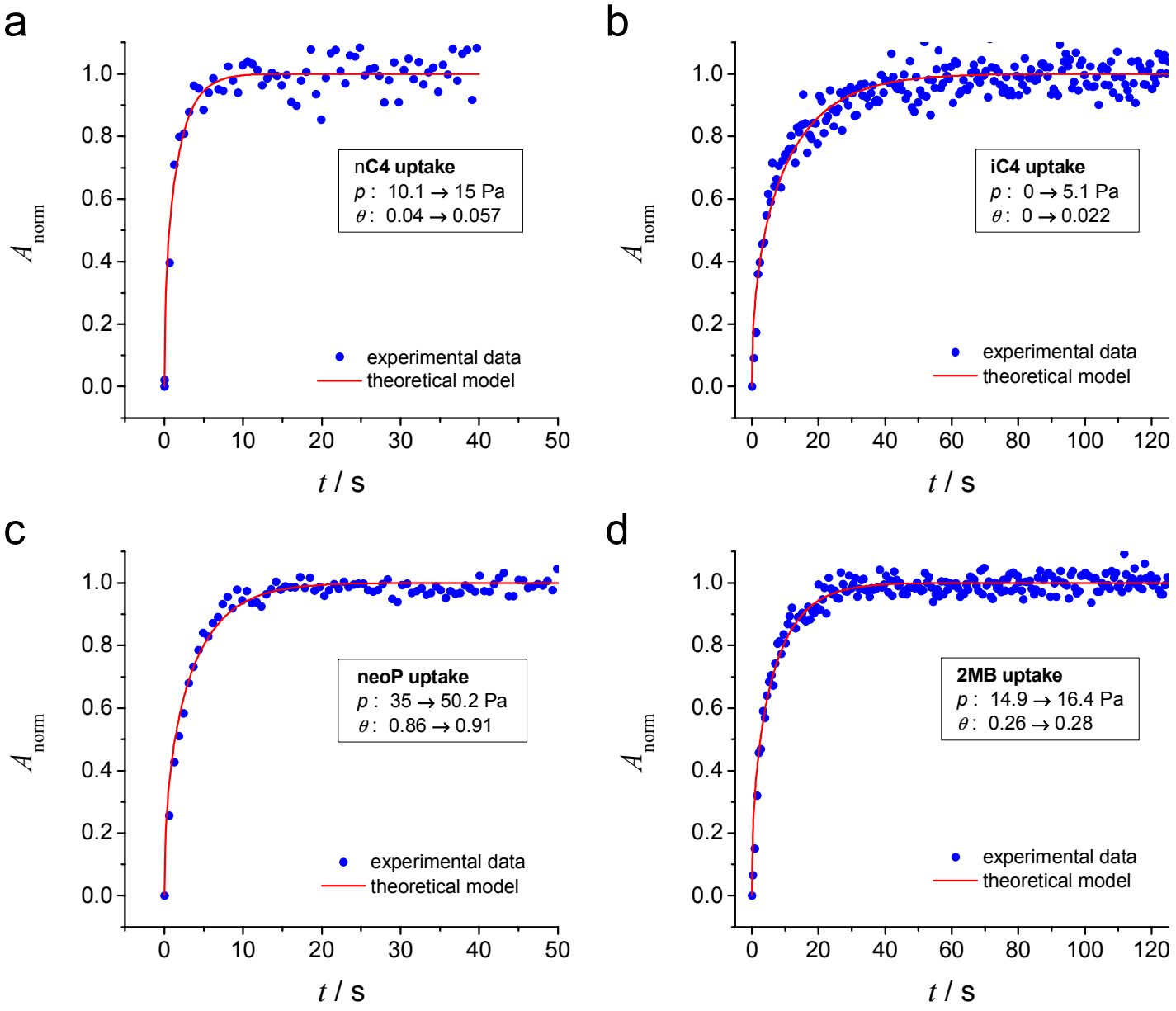
a
b
c
d
A_{norm}
t / s
nC4 uptake
p : 10.1 → 15 Pa
θ : 0.04 → 0.057
iC4 uptake
p : 0 → 5.1 Pa
θ : 0 → 0.022
neoP uptake
p : 35 → 50.2 Pa
θ : 0.86 → 0.91
2MB uptake
p : 14.9 → 16.4 Pa
θ : 0.26 → 0.28
experimental data
theoretical model

Appendix A3: Molecular Simulation methodology and simulation results

1. Monte Carlo simulation methodology

The structural information for CuBTC simulations have been taken from Chui et al. [1] and Yang and Zhong [2]. The crystal structure of Chui et al. [1] includes axial oxygen atoms weakly bonded to the Cu atoms, which correspond to water ligands. Our simulations have been performed on the dry CuBTC with these oxygen atoms removed. The structure data file we used is available on our website [3]. The framework structure, and the pore landscapes are presented in Figures 1, 2, 3, 4, and 5.

The adsorption isotherms were computed using Monte Carlo (MC) simulations in the grand canonical (GC) ensemble. The united atom force field for alkanes, developed by Dubbeldam et al. [4], is used to describe alkane-alkane, Lennard-Jones, interactions. Some simulations were also carried out for Ar, Ne, Kr, H_2 and Ne. The intermolecular Lennard-Jones parameters for He, Ne and Ar are those listed in Skoulidas and Sholl[5]. For Kr the parameters are from Talu and Myers [6]. The force field for H_2 corresponds to that given by Kumar et al. [7]. The Lennard-Jones parameters for molecule-molecule interactions of Ar, Ne, He, Kr, and H_2 are summarized in Tables 1. For alkane-alkane interactions the tabulated force fields are available in Dubbeldam et al. [4]; the potential for the n-alkanes includes bond stretching, bending, and torsion.

The CuBTC framework was considered to be rigid in the simulations. For the atoms in the guest metal organic framework CuBTC, the generic UFF [8] and DREIDING [9] force fields were used. The Lennard-Jones parameters in Table 2. The Lorentz-Berthelot mixing rules were applied for calculating σ and ε/k_B for guest-host interactions. For simulations with linear and branched alkanes with two or more C atoms, the Configurational-Bias Monte Carlo (CBMC) simulation technique [10, 11] was

employed. The beads in the chain are connected by harmonic bonding potentials. A harmonic cosine bending potential models the bond bending between three neighboring beads, a Ryckaert-Bellemans potential controls the torsion angle. The beads in a chain separated by more than three bonds interact with each other through a Lennard-Jones potential. The Lennard-Jones potentials are shifted and cut at 12 Å. The CBMC simulation details have been given in detail elsewhere [4, 10-12].

The simulation box chosen was 1 unit cell of CuBTC (a = b = c = 26.343 Å). Periodic boundary conditions were employed.

The CBMC simulations were performed using the BIGMAC code developed by T.J.H. Vlugt[13] as basis.

Rather than calculating the $1/\Gamma_i$ by analytic or numerical differentiation of the simulated adsorption isotherms, the $1/\Gamma_i$ data is directly obtained by sampling several samples of equilibrated molecules within the simulation box and using the Reed and Ehrlich fluctuation formula

$$\frac{1}{\Gamma_i} = \frac{\left\langle n_i^2 \right\rangle - \left\langle n_i \right\rangle^2}{\left\langle n_i \right\rangle} \qquad (1)$$

where n_i represents the number of molecules in the simulation box and $\langle \ldots \rangle$ denotes ensemble averaging. This fluctuation formula has been recently used in Monte Carlo simulations of adsorption in zeolites [14-17].

We also determined the isosteric heats of adsorption, ΔH_{st}, for alkanes from CBMC simulations using the fluctuation formula

$$\Delta H_{st} = RT - \frac{< U_i n_i > - < U_i >< n_i >}{\left\langle n_i^2 \right\rangle - \left\langle n_i \right\rangle^2} \qquad (2)$$

In this connection the reader is referred to the paper of Karavias and Myers [18], who point out that the conventional definition of the isosteric heat of *adsorption* is in reality the heat of *desorption*.

The molecules investigated in the present study are methane (C1), ethane (C2), propane (C3), n-butane (nC4), iso-butane, (iC4), 2-methylbutane (2MB), 2,2-dimethylpropane (neoP = neopentane), n-

pentane (nC5), Ar, and Ne. The data for nC5, Ar, and Ne is not discussed in the text of the main paper but has been included in this Appendix A2 for completeness.

In order to determine the distribution of molecules within the CuBTC framework, sampling volumes indicated by the red and blue spheres in Figures 6 and 7 were used. The CBMC simulations were run for a total of 10^6 cycles, and the equilibrated 10^3 cycles were sampled to obtain the distributions within the red and blue spheres and in the rest of the pore space. A 2D picture of the sampling zones is shown in Figure 8.

2. MD simulation methodology

Diffusion is simulated using Newton's equations of motion until the system properties, on average, no longer change in time. The Verlet algorithm is used for time integration. A time step of 1 fs was used in all simulations. For each simulation, *initializing* CBMC moves are used to place the molecules in the domain, minimizing the energy. Next, follows an *equilibration* stage. These are essentially the same as the production cycles, only the statistics are not yet taken into account. This removes any initial large disturbances in the system that do not affect statistics on molecular displacements. After a fixed number of initialization and equilibrium steps, the MD simulation *production* cycles start. For every cycle, the statistics for determining the mean square displacements (MSDs) are updated. The MSDs are determined for time intervals ranging from 2 fs to 1 ns. In order to do this, an order-*N* algorithm, as detailed in Chapter 4 of Frenkel and Smit[10] is implemented. The Nosé-Hoover thermostat is applied to all the diffusing particles.

The DLPOLY code[19] was used along with the force field implementation as described in the previous section. DL_POLY is a molecular dynamics simulation package written by W. Smith, T.R. Forester and I.T. Todorov and has been obtained from CCLRCs Daresbury Laboratory via the website.[19]

The MD simulations were carried out for a variety of molecular loadings. All simulations were carried out on the LISA clusters of PCs equipped with Intel Xeon processors running at 3.4 GHz on the Linux

operating system[20]. Each MD simulation, for a specified loading, was run for 120 h, determined to be long enough to obtain reliable statistics for determination of the diffusivities. In many cases, several independent MD simulations were run and the results averaged.

The self-diffusivities, $D_{\mathrm{i,self}}$, were computed by analyzing the mean square displacement of each species i for each of the coordinate directions:

$$D_{i,self} = \frac{1}{2n_i} \lim_{\Delta t \to \infty} \frac{1}{\Delta t} \left\langle \left(\sum_{l=1}^{n_i} \left(\mathbf{r}_{l,i}(t + \Delta t) - \mathbf{r}_{l,i}(t) \right)^2 \right) \right\rangle \tag{3}$$

In this expression n_{i} represents the number of molecules of species i respectively, and $\mathbf{r}_{\mathrm{l,i}}(t)$ is the position of molecule l of species i at any time t. Even though the self-diffusivities are not discussed in the main text of the paper, the simulated values are presented in the Figures accompanying this Supplementary material.

For single component diffusion, the Maxwell-Stefan diffusivity was determined for each of the coordinate directions from

$$Đ_i = \frac{1}{2} \lim_{\Delta t \to \infty} \frac{1}{n_i} \frac{1}{\Delta t} \left\langle \left(\sum_{l=1}^{n_i} \left(\mathbf{r}_{l,i}(t + \Delta t) - \mathbf{r}_{l,i}(t) \right) \right)^2 \right\rangle \tag{4}$$

The CuBTC is isotropic and the average values calculated according to $Đ = \left(Đ_x + Đ_y + Đ_z \right)/3$ are presented. In all cases reported here, the MSD values were linear in t for $t > 10$ ps.

The self-exchange coefficient $Đ_{\mathrm{ii}}$ were calculated from

$$Đ_{ii} = \frac{\theta_i}{\frac{1}{D_{i,self}} - \frac{1}{Đ_i}} \tag{5}$$

where θ_{i} is the fractional occupancy:

$$\theta_i = \frac{q_i}{q_{i,sat}} \tag{6}$$

The values of the saturation capacities $q_{\mathrm{i,sat}}$ were determined from CBMC simulations of the isotherms.

3. Animations

For visual appreciation of the diffusion phenomena in CuBTC, animations were created on the basis of the MD simulations; these can be viewed by downloading the movies from our website[3].

4. Simulation results

The CBMC, and MD simulation results for methane (C1), ethane (C2), propane (C3), n-butane (nC4), iso-butane, (iC4), 2-methylbutane (2MB), 2,2 dimethylpropane (neoP = neopentane), n-pentane (nC5), Ar, and Ne, along with snapshots showing the location of molecules are given in graphical form in Figures 9, 10, 11, 12, 13, 14, 15, 16, 17, 18, 19. 20, 21, 22, 23, 24, 25, 26, 27, 28, 29, and 30. The loadings in these Figures is expressed in terms of mol/kg framework. The factor for converting molecules per unit cell to mol/kg is 0.10336; for example a loading of 100 molecules per unit cell corresponds with 10.336 mol/kg.

Also shown in Figure 9 is the comparisons between the absolute loadings from CBMC simulations with the experimental data of Senkovska and Kaskel [21]. The excellent agreement points to the reliability of the molecular simulations.

5. Acknowledgements

We are grateful to T.J.H. Vlugt, Delft, for providing the BIGMAC code. This code was modified to handle rigid molecular structures and charges, with generous assistance and technical inputs from S. Calero, Seville.

For CuBTC simulations we obtained the structural data files from D. Dubbeldam, Northwestern University; for this we are grateful. Additional information on force fields for CuBTC was also provided by S. Calero, Seville.

6. Notation

$D_{i,self}$	self-diffusivity, $m^2\ s^{-1}$
$Đ_i$	Maxwell-Stefan diffusivity of species *i*, $m^2\ s^{-1}$
f_i	fugacity of species *i*, Pa
n_i	number of molecules of species *i* in simulation box, dimensionless
q_i	loading of species *i*, mol kg^{-1}
$q_{i,sat}$	saturation loading of species *i*, mol kg^{-1}
$\mathbf{r}_{l,i}(t)$	position of molecule *l* of species *i* at any time *t*, m
R	gas constant, 8.314 J $mol^{-1}\ K^{-1}$
t	time, s
T	absolute temperature, K
x	spatial distance, m

Greek letters

Γ_i	thermodynamic factors, dimensionless
θ_i	fractional occupancy of component *i*, dimensionless
μ_i	molar chemical potential, J mol^{-1}
ρ	framework density, kg m^{-3}

Subscripts

sat	referring to saturation conditions
i	referring to component *i*

Table 1. Lennard-Jones parameters for guest molecules Ar, Ne, He, Kr, and H_2.

(pseudo-) atom	σ / Å	ε/k_B / K
Ar	3.42	124.07
Ne	2.789	35.7
He	2.28	10.223
Kr	3.636	166.4
H_2	2.782	38.7

Table 2. Lennard-Jones parameters for atoms in metal-organic host framework The charges on the atoms C_a, C_b, and C_c are different (see also Figure 5); these are not specified here in this Table because we deal only with neutral molecules in the present simulation studies. The Cu parameters are taken from the UFF force field, and also given by Yang and Zhong [2].

(pseudo-) atom	σ / Å	ε/k_B / K
Cu	3.114	2.518
O	3.03	48.19
C_a	3.47	47.86
C_b	3.47	47.86
C_c	3.47	47.86
H	2.85	7.65

7. References

[1] S.S.Y. Chui, S.M.F. Lo, J.P.H. Charmant, A.G. Orpen, I.D. Williams, A chemically functionalizable nanoporous material $[Cu_3(TMA)_2(H2O)_3]_n$, Science 283 (1999) 1148-1150.

[2] Q. Yang, C. Zhong, Electrostatic-Field-Induced Enhancement of Gas MixtureSeparation in Metal-OrganicFrameworks: A Computational Study, ChemPhysChem 7 (2006) 1417-1421.

[3] J.M. van Baten, R. Krishna, MD animations of diffusion in nanoporous materials, University of Amsterdam, Amsterdam, http://www.science.uva.nl/research/cr/animateMD/, 1 June 2008.

[4] D. Dubbeldam, S. Calero, T.J.H. Vlugt, R. Krishna, T.L.M. Maesen, B. Smit, United Atom Forcefield for Alkanes in Nanoporous Materials, J. Phys. Chem. B 108 (2004) 12301-12313.

[5] A.I. Skoulidas, D.S. Sholl, Transport diffusivities of CH_4, CF_4, He, Ne, Ar, Xe, and SF_6 in silicalite from atomistic simulations, J. Phys. Chem. B 106 (2002) 5058-5067.

[6] O. Talu, A.L. Myers, Reference potentials for adsorption of helium, argon, methane and krypton in high-silica zeolites, Colloids Surf., A 187-188 (2001) 83-93.

[7] A.V.A. Kumar, H. Jobic, S.K. Bhatia, Quantum effects on adsorption and diffusion of hydrogen and deuterium in microporous materials, J. Phys. Chem. B 110 (2006) 16666-16671.

[8] A.K. Rappé, C.J. Casewit, K.S. Colwel, W.A. Goddard, W.M. Skiff, UFF, a Full Periodic Table Force Field for Molecular Mechanics and Molecular Dynamics Simulations, J. Am. Chem. Soc. 114 (1992) 10024-10035.

[9] S.L. Mayo, B.D. Olafson, W.A. Goddard, DREIDING: A Generic Force Field for Molecular Simulations, J. Phys. Chem. 94 (1990) 8897-8909.

[10] D. Frenkel, B. Smit, Understanding molecular simulations: from algorithms to applications, Academic Press, 2nd Edition, San Diego, 2002.

[11] T.J.H. Vlugt, R. Krishna, B. Smit, Molecular simulations of adsorption isotherms for linear and branched alkanes and their mixtures in silicalite, J. Phys. Chem. B 103 (1999) 1102-1118.

[12] D. Dubbeldam, S. Calero, T.J.H. Vlugt, R. Krishna, T.L.M. Maesen, E. Beerdsen, B. Smit, Force Field Parametrization through Fitting on Inflection Points in Isotherms, Phys. Rev. Lett. 93 (2004) 088302.

[13] T.J.H. Vlugt, BIGMAC, University of Amsterdam, http://molsim.chem.uva.nl/bigmac/, 1 November 2000.

[14] H. Chen, D.S. Sholl, Efficient Simulation of Binary Adsorption Isotherms Using Transition Matrix Monte Carlo, Langmuir 22 (2006) 709-716.

[15] R. Krishna, J.M. van Baten, Using molecular simulations for screening of zeolites for separation of CO_2/CH_4 mixtures, Chem. Eng. J. 133 (2007) 121-131.

[16] R. Krishna, J.M. van Baten, Linking the loading dependence of the Maxwell-Stefan diffusivity of linear alkanes in zeolites with the thermodynamic correction factor, Chem. Phys. Lett. 420 (2006) 545-549.

[17] H. Jobic, C. Laloué, C. Laroche, J.M. van Baten, R. Krishna, Influence of isotherm inflection on the loading dependence of the diffusivities of n-hexane and n-heptane in MFI zeolite. Quasi-Elastic Neutron Scattering experiments supplemented by molecular simulations, J. Phys. Chem. B 110 (2006) 2195-2201.

[18] F. Karavias, A.L. Myers, Isosteric Heats of Multicomponent Adsorption: Thermodynamics and Computer Simulations, Langmuir 7 (1991) 3118-3126.

[19] W. Smith, T.R. Forester, I.T. Todorov, The DL_POLY Molecular Simulation Package, Warrington, England, http://www.cse.clrc.ac.uk/msi/software/DL_POLY/index.shtml, March 2006.

[20] SARA, Computing & Networking Services, Amsterdam, https://subtrac.sara.nl/userdoc/wiki/lisa/description, 16 January 2008.

[21] I. Senkovska, S. Kaskel, High pressure methane adsorption in the metal-organic frameworks $Cu_3(btc)_2$, $Zn_2(bdc)_2dabco$, and $Cr_3F(H_2O)_2O(bdc)_3$, Microporous Mesoporous Mater. XXX (2008) XX-XX. http://dx.doi.org/10.1016/j.micromeso.2007.09.016

[22] A. Vishnyakov, P.I. Ravikovitch, A.V. Neimark, M. Bülow, Q.M. Wang, Nanopore Structure and Sorption Properties of Cu-BTC Metal-Organic Framework, Nano Lett. 3 (2003) 713-718.

8. Captions for Figures

Figure 1. CuBTC framework structure.

Figure 2. Pore landscape highlighting the large windows and the entrance to the tetrahedral side pockets

Figure 3. Pore landscape highlighting the triangular window to the tetrahedral side pockets.

Figure 4. Top-down view of the large windows and the tetrahedral side pockets

Figure 5. Cu atoms connected to organic linker. This picture is adapted from Vishnyakov et al.[22], and specifies the different carbon atoms, C_a, C_b, and C_c; see also Table 2.

Figure 6. The red spheres envelop the mouth of the tetrahedral pockets. The blue spheres envelop the central region of the tetrahedral pockets. These two spheres are used in sampling of the equilibrium positions to determine the probability of locating a molecule in the pockets.

Figure 7. Top-down view of the red, and blue spheres used for sampling.

Figure 8. Top-down, two-dimensional view showing the sampling envelopes for the tetrahedral pockets.

Figure 9. Adsorption isotherm, along with loading in tetrahedral pockets, and diffusivity data for C1 in CuBTC at 300 K. The saturation capacity obtained from CBMC simulations, $q_{i,sat}$ = 27 mol/kg. Also shown are the comparisons between the absolute loadings from CBMC simulations with the experimental data of Senkovska and Kaskel [21].

Figure 10. Variation of the Maxwell-Stefan diffusivity $Đ_i$, the inverse thermodynamic factor $1/\Gamma_i$, and the isosteric heat of adsorption, ΔH_{st}, of C1 in CuBTC. Also shown are snapshots of the equilibrium location of molecules in the large cage and within a side pocket.

Figure 11. Adsorption isotherm, along with loading in tetrahedral pockets, and diffusivity data for C2 in CuBTC at 300 K. The saturation capacity obtained from CBMC simulations, $q_{i,sat}$ = 17.5 mol/kg.

Figure 12. Variation of the Maxwell-Stefan diffusivity $Đ_i$, the inverse thermodynamic factor $1/\Gamma_i$, and the isosteric heat of adsorption, ΔH_{st}, of C2 in CuBTC. Also shown are snapshots of the equilibrium location of molecules in the large cage and within a side pocket.

Figure 13. Adsorption isotherm, along with loading in tetrahedral pockets, and diffusivity data for C3 in CuBTC at 300 K. The saturation capacity obtained from CBMC simulations, $q_{i,sat}$ = 13 mol/kg.

Figure 14. Variation of the Maxwell-Stefan diffusivity $Đ_i$, the inverse thermodynamic factor $1/\Gamma_i$, and the isosteric heat of adsorption, ΔH_{st}, of C3 in CuBTC. Also shown are snapshots of the equilibrium location of molecules in the large cage and within a side pocket.

Figure 15. Adsorption isotherm, along with loading in tetrahedral pockets, and diffusivity data for nC4 in CuBTC at 300 K. Also shown is the comparison of CBMC and IRM isotherms, in terms of occupancies. The saturation capacity obtained from CBMC simulations, $q_{i,sat}$ = 9 mol/kg.

Figure 16. Variation of the Maxwell-Stefan diffusivity $Đ_i$, the inverse thermodynamic factor $1/\Gamma_i$, and the isosteric heat of adsorption, ΔH_{st}, of nC4 in CuBTC. Also shown are snapshots of the equilibrium location of molecules in the large cage and within a side pocket.

Figure 17. Adsorption isotherm, along with loading in tetrahedral pockets, and diffusivity data for iC4 in CuBTC at 300 K. The saturation capacity obtained from CBMC simulations, $q_{i,sat}$ = 8.7 mol/kg.

Figure 18. Variation of the Maxwell-Stefan diffusivity $Đ_i$, the inverse thermodynamic factor $1/\Gamma_i$, and the isosteric heat of adsorption, ΔH_{st}, of iC4 in CuBTC. Also shown are snapshots of the equilibrium location of molecules in the large cage and within a side pocket.

Figure 19. Adsorption isotherm, along with loading in tetrahedral pockets, and diffusivity data for neoP in CuBTC at 300 K. The saturation capacity obtained from CBMC simulations, $q_{i,sat}$ = 6.6 mol/kg.

Figure 20. Variation of the Maxwell-Stefan diffusivity $Đ_i$, the inverse thermodynamic factor $1/\Gamma_i$, and the isosteric heat of adsorption, ΔH_{st}, of neoP in CuBTC. Also shown are snapshots of the equilibrium location of molecules in the large cage and within a side pocket.

Figure 21. Adsorption isotherm, along with loading in tetrahedral pockets, and diffusivity data for 2MB in CuBTC at 300 K. The saturation capacity obtained from CBMC simulations, $q_{i,sat}$ = 6.6 mol/kg.

Figure 22. Variation of the Maxwell-Stefan diffusivity $Đ_i$, the inverse thermodynamic factor $1/\Gamma_i$, and the isosteric heat of adsorption, ΔH_{st}, of 2MB in CuBTC. Also shown are snapshots of the equilibrium location of molecules in the large cage and within a side pocket.

Figure 23. Adsorption isotherm, along with loading in tetrahedral pockets, and diffusivity data for nC5 in CuBTC at 300 K.

Figure 24. Variation of the Maxwell-Stefan diffusivity $Đ_i$, the inverse thermodynamic factor $1/\Gamma_i$, and the isosteric heat of adsorption, ΔH_{st}, of nC5 in CuBTC. Also shown are snapshots of the equilibrium location of molecules in the large cage and within a side pocket.

Figure 25. Adsorption isotherm, along with loading in tetrahedral pockets, and diffusivity data for Ar in CuBTC at 300 K.

Figure 26. Variation of the Maxwell-Stefan diffusivity $Đ_i$, the inverse thermodynamic factor $1/\Gamma_i$, and the isosteric heat of adsorption, ΔH_{st}, of Ar in CuBTC. Also shown are snapshots of the equilibrium location of molecules in the large cage.

Figure 27. Adsorption isotherm, along with loading in tetrahedral pockets, and diffusivity data for Ne in CuBTC at 300 K.

Figure 28. Variation of the Maxwell-Stefan diffusivity $Đ_i$, the inverse thermodynamic factor $1/\Gamma_i$, and the isosteric heat of adsorption, ΔH_{st}, of Ne in CuBTC. Also shown are snapshots of the equilibrium location of molecules in the large cage.

Figure 29. Adsorption isotherm and diffusivity data for He, and H_2 in CuBTC at 300 K.

Figure 30. Adsorption isotherm and diffusivity data for Kr in CuBTC at 300 K.

Figure 1

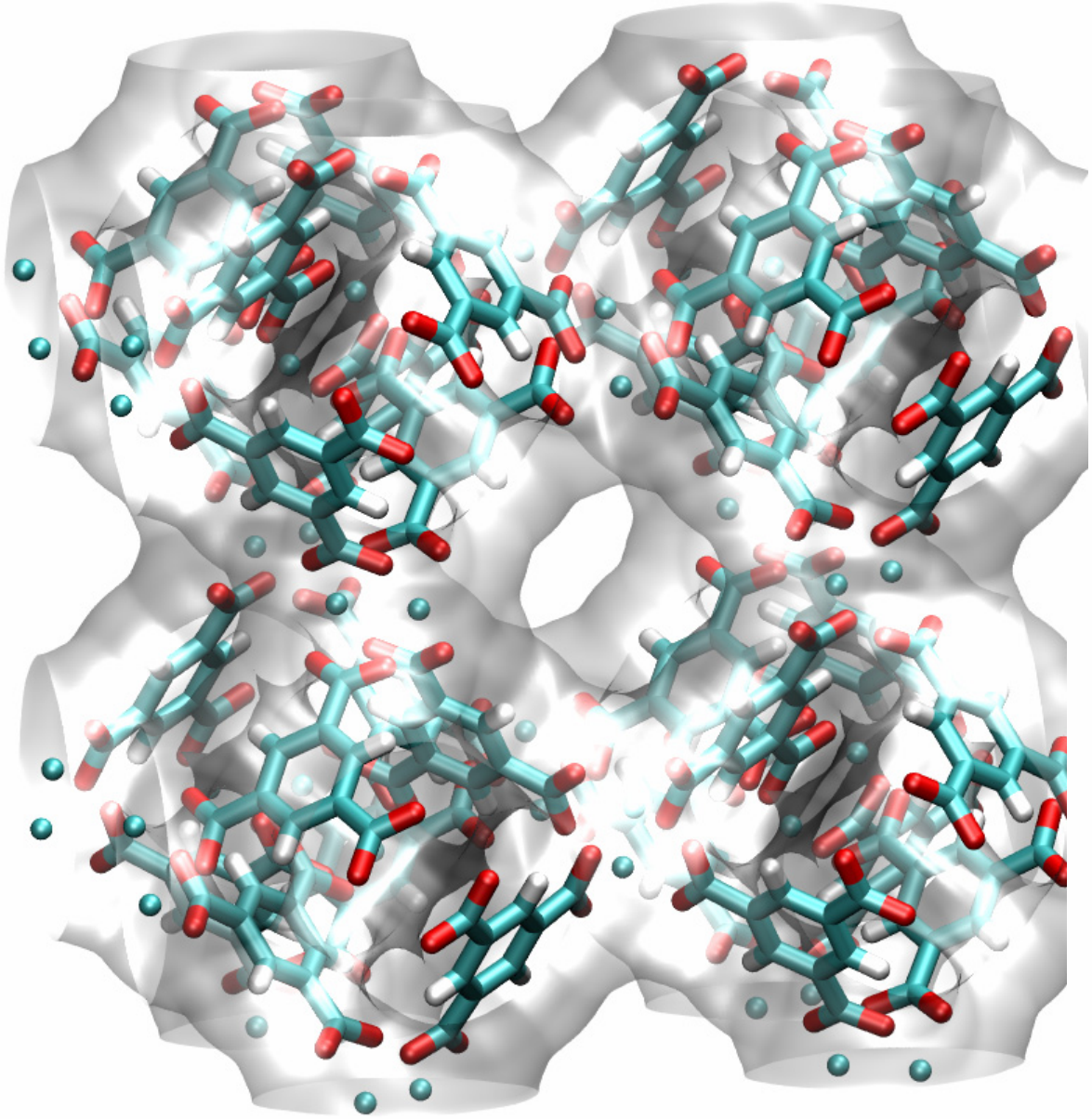

9 Å windows

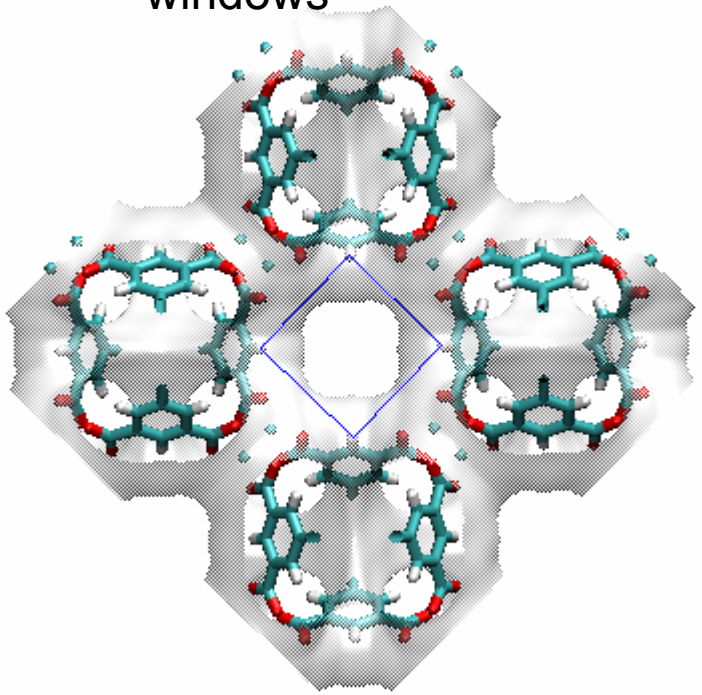

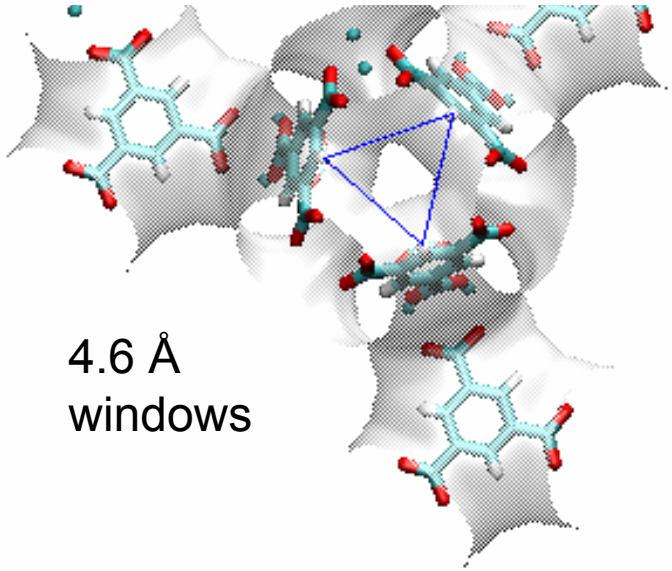

4.6 Å windows

Figure 2

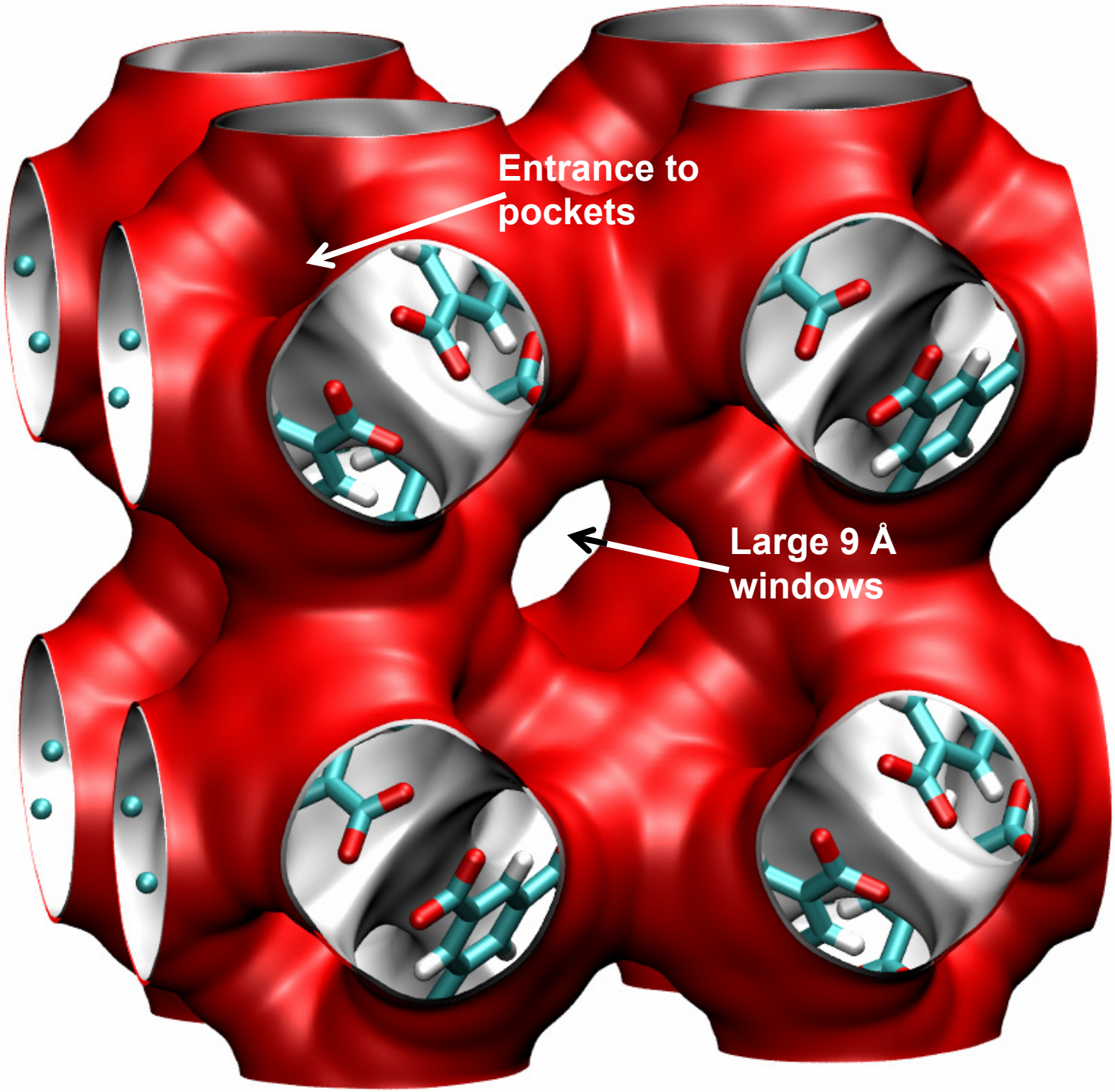

Figure 3

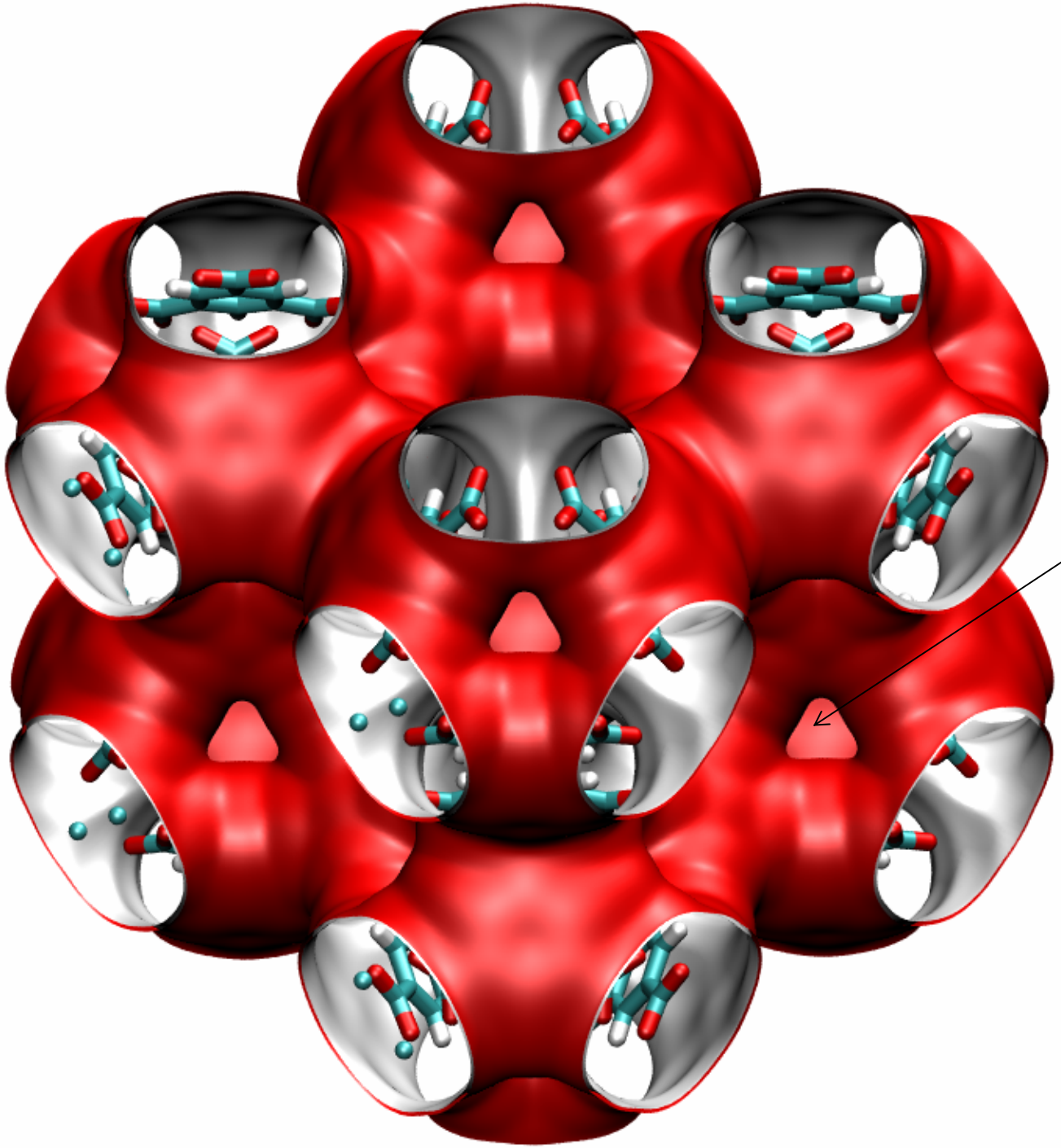

Triangular 4.6 Å windows connecting large cages to tetrahedral side pockets

Figure 4

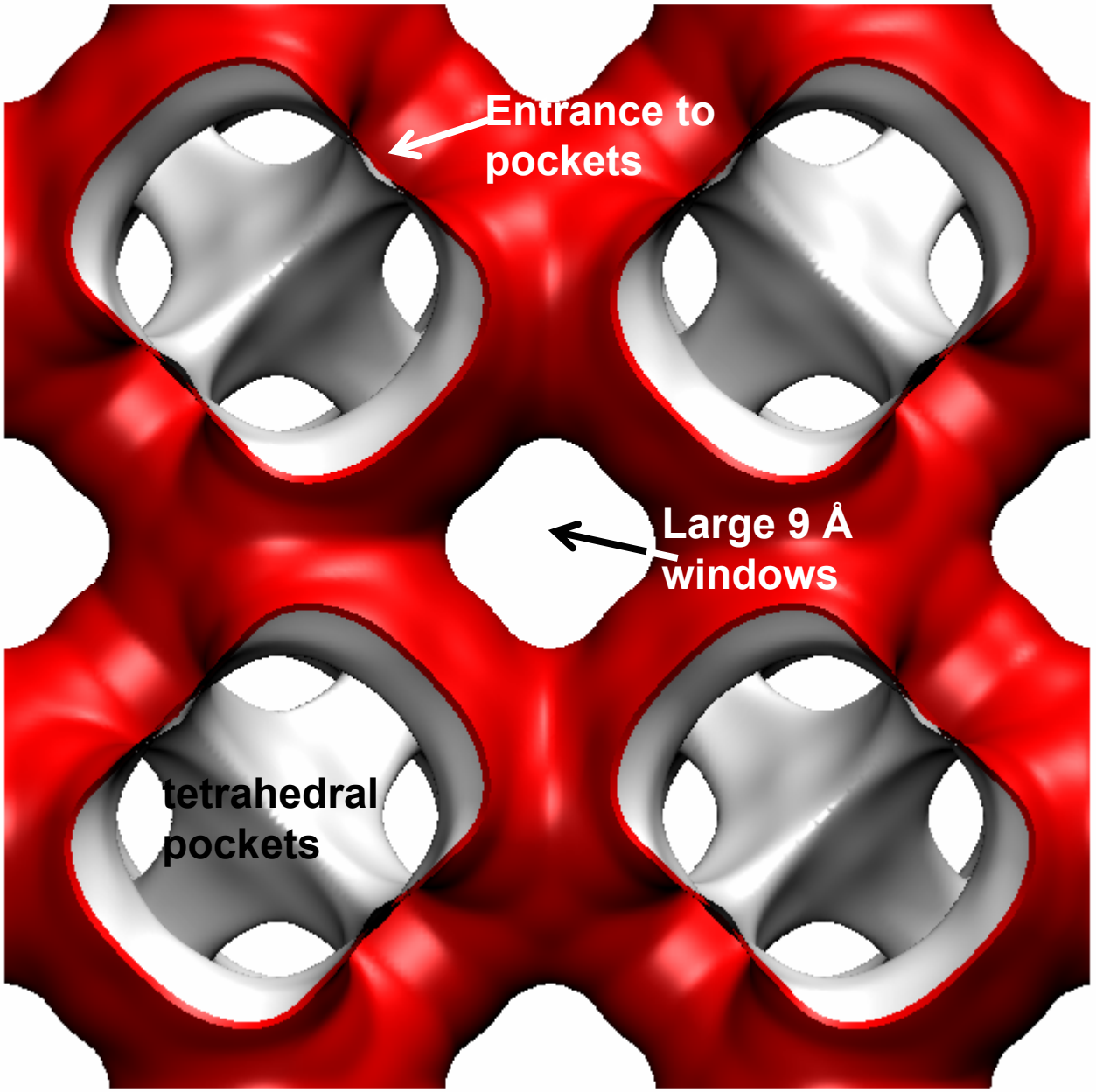

Figure 5

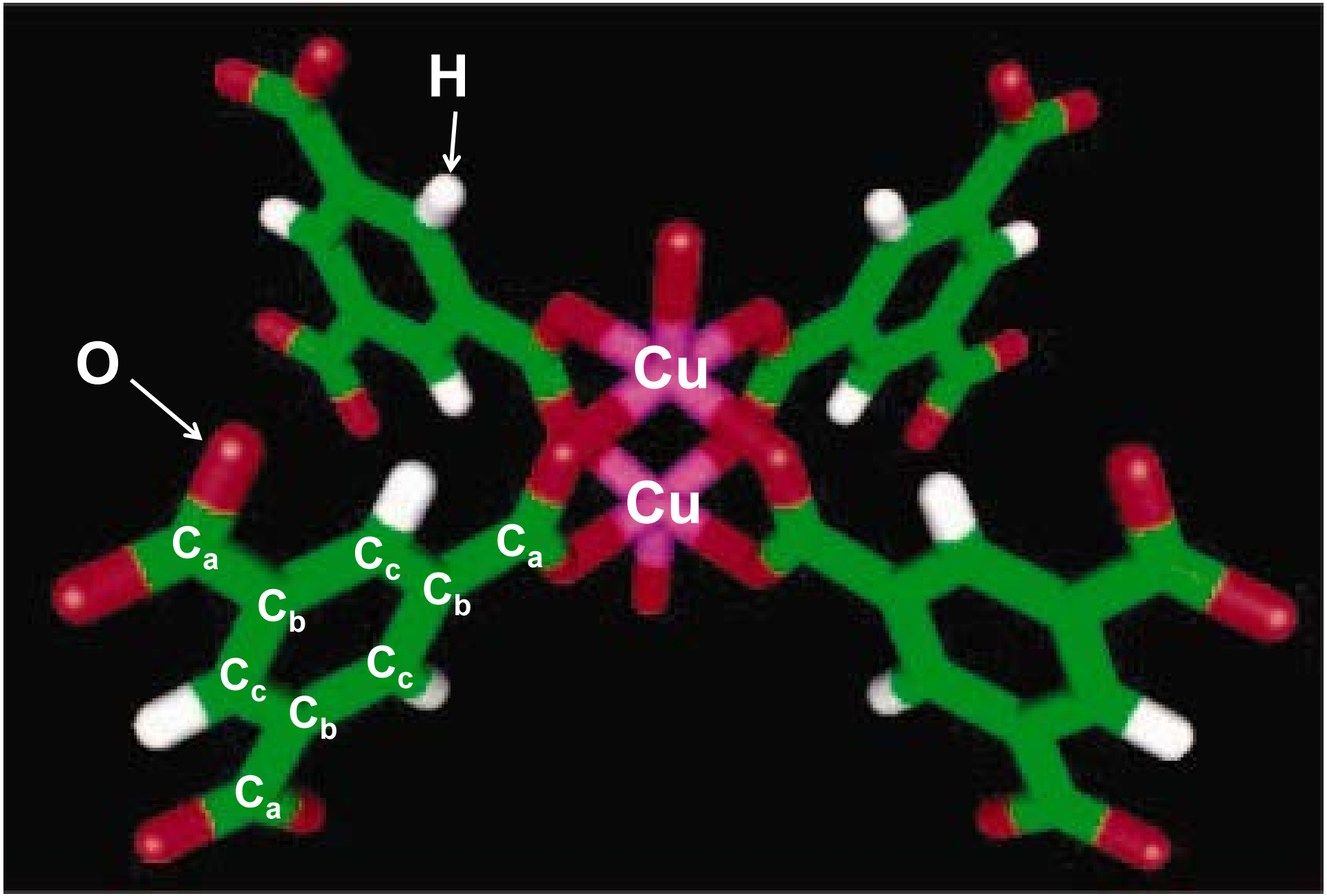

Figure 6

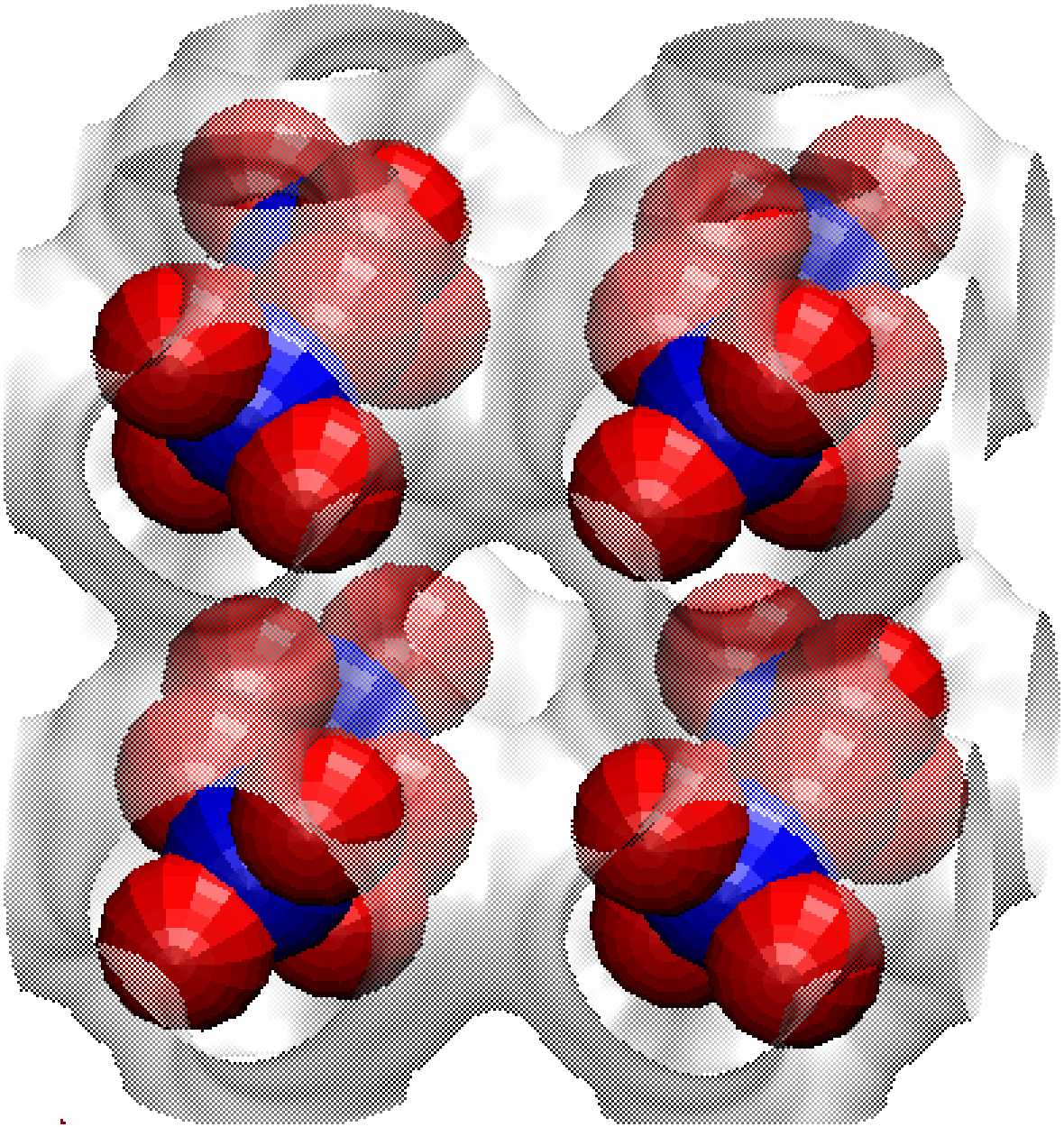

The red and blue spheres combined represent the tetrahedral side pockets

Figure 7

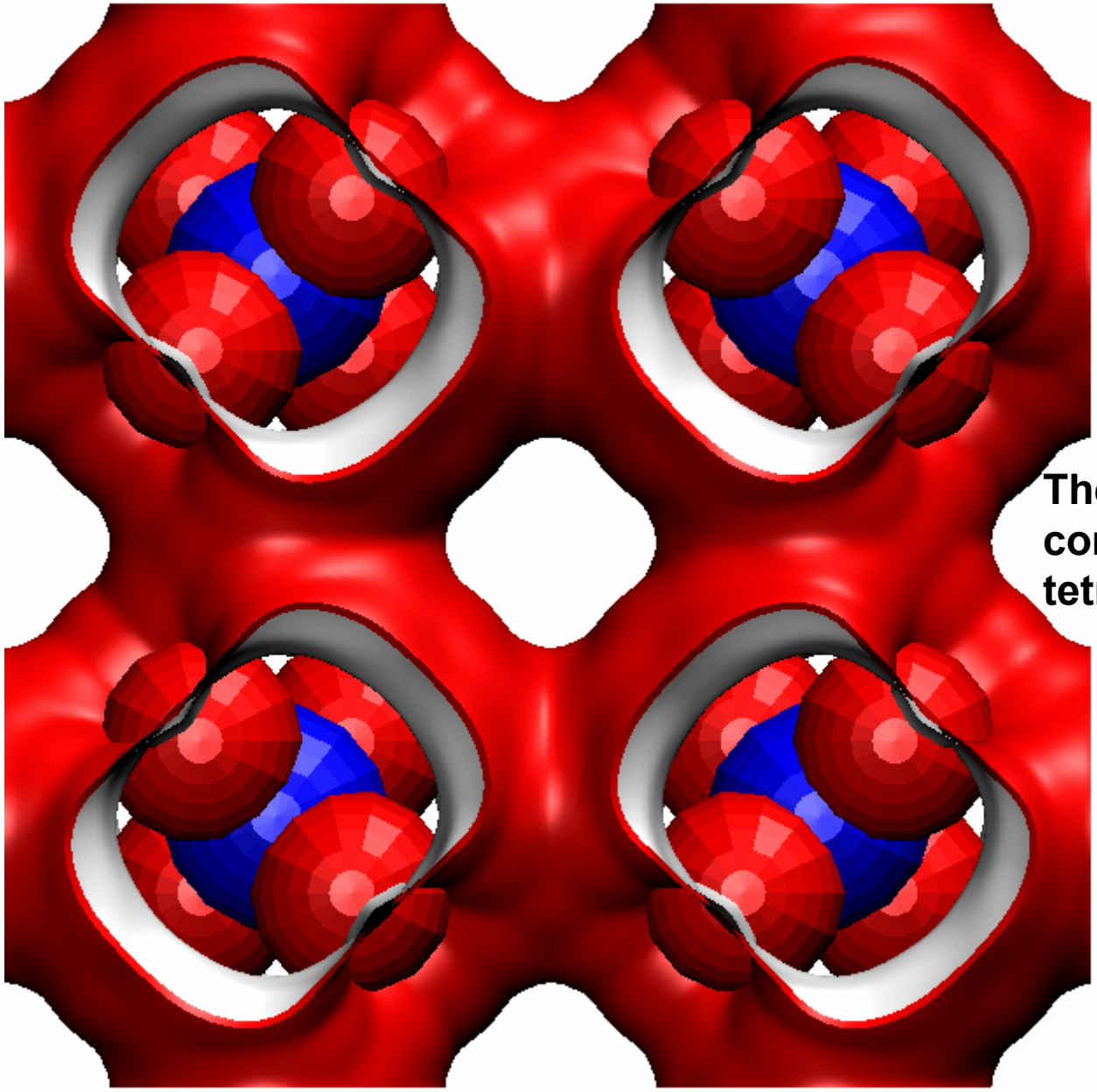

The red and blue spheres combined represent the tetrahedral side pockets

Figure 8

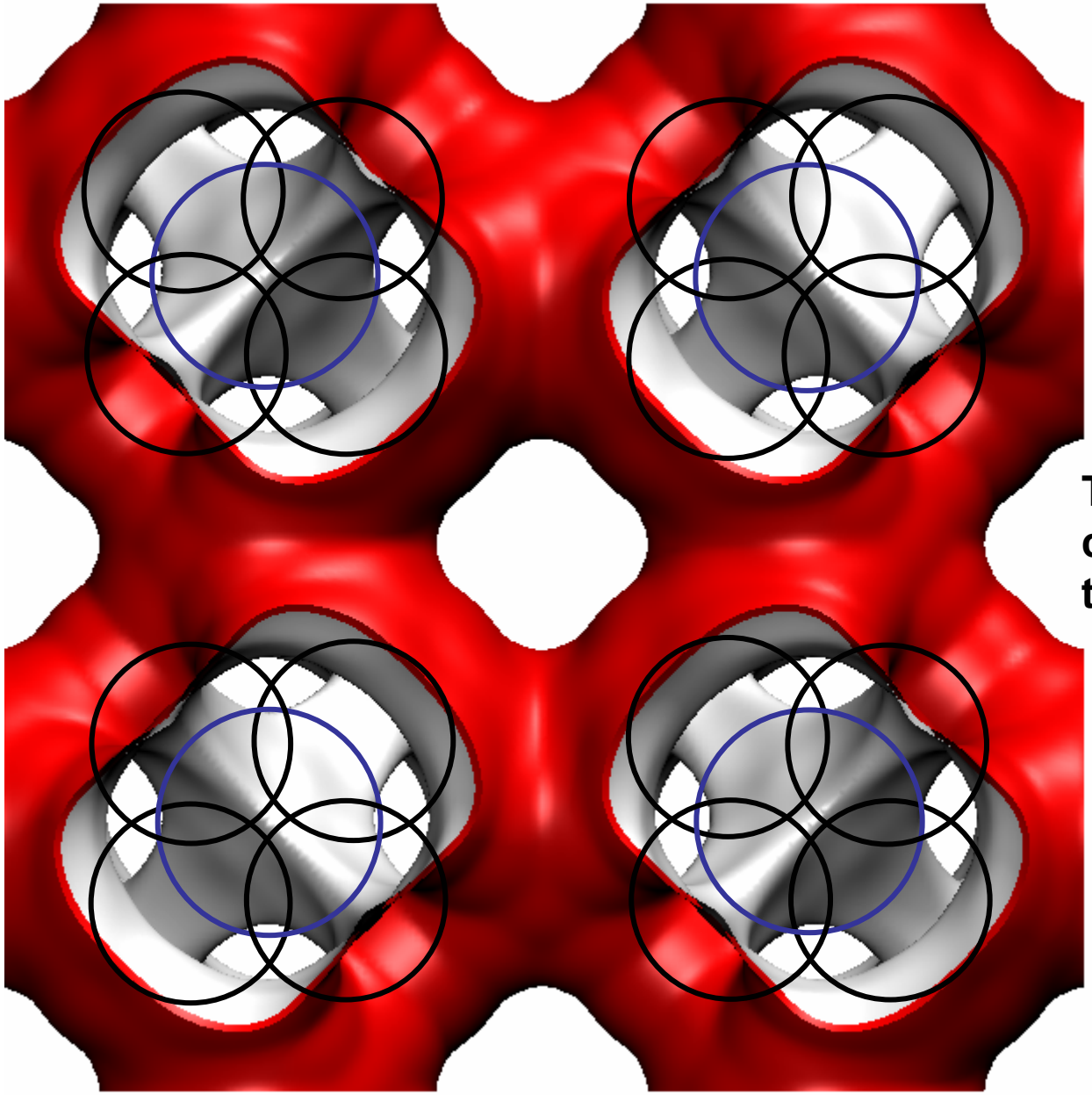

The black and blue circles combined represent the tetrahedral side pockets

Figure 9

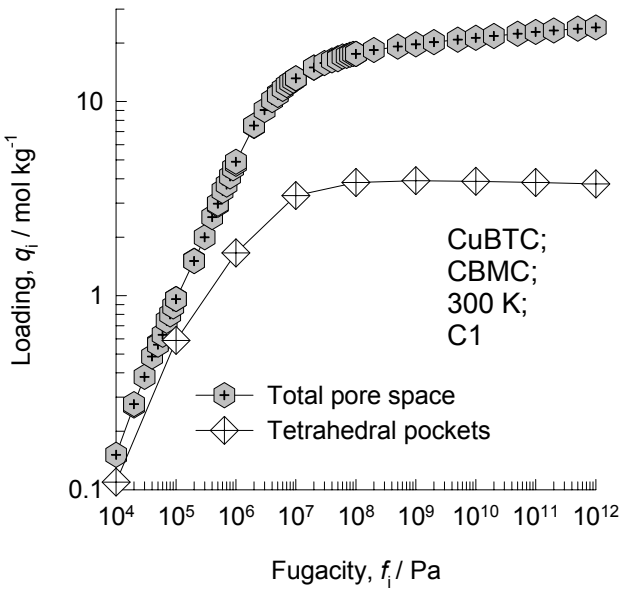

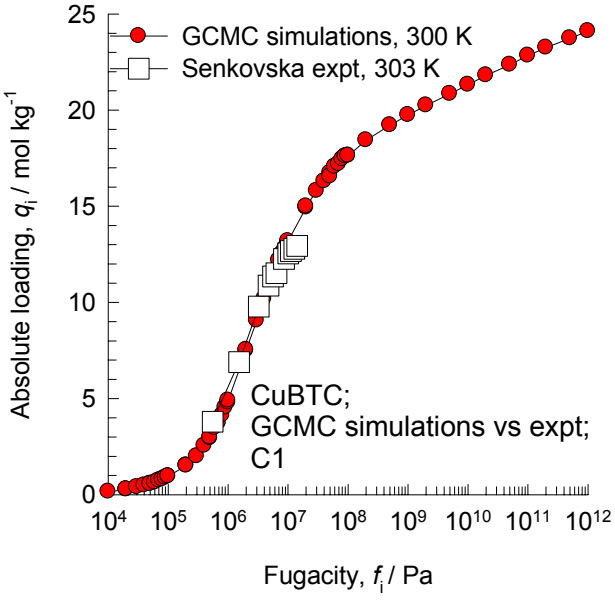

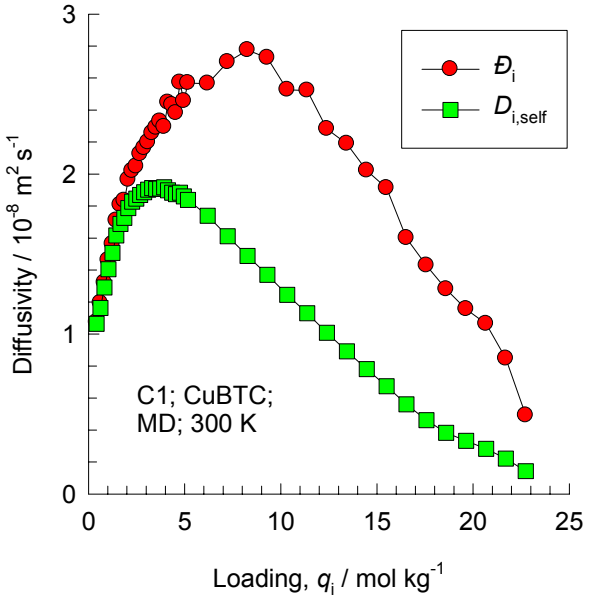

CuBTC
300 K, C1

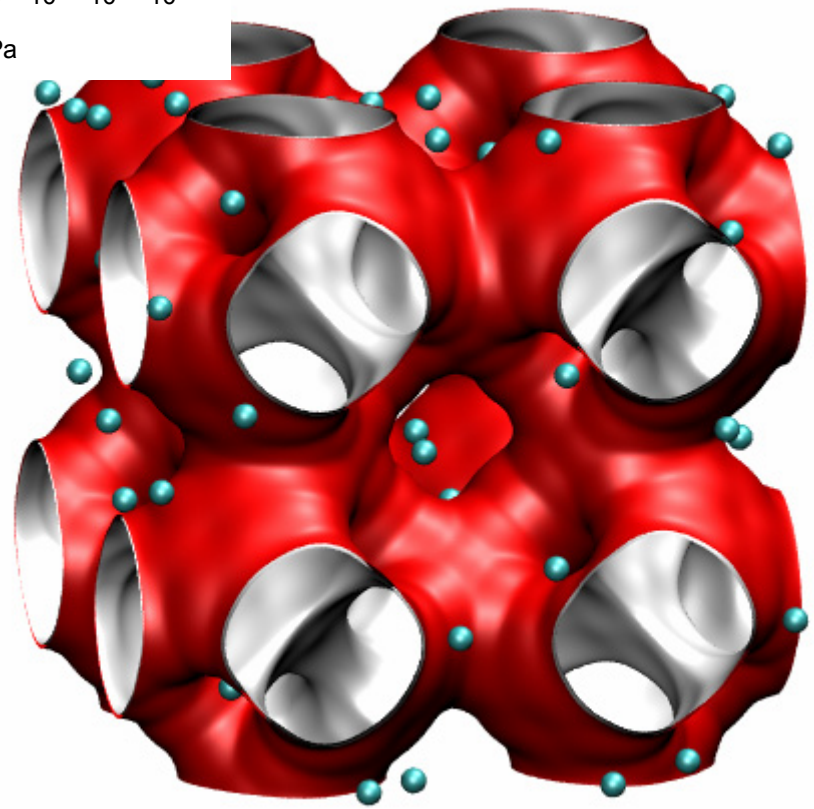

Figure 10

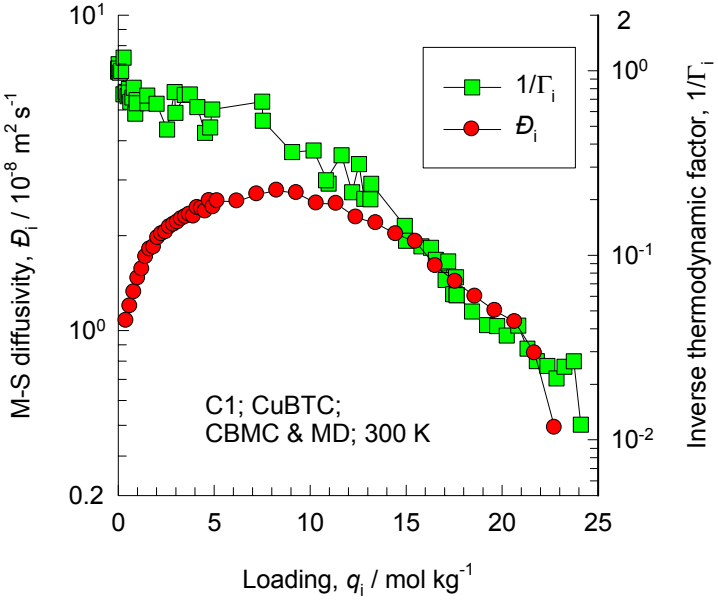

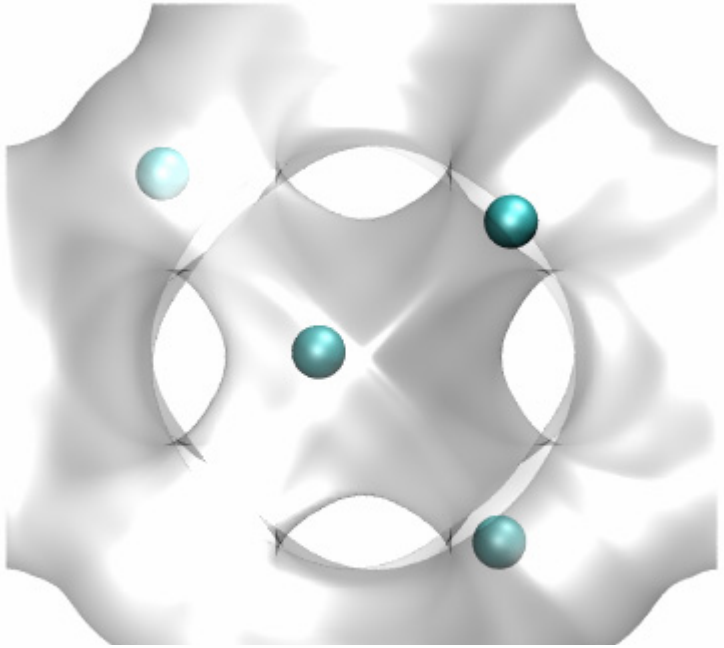

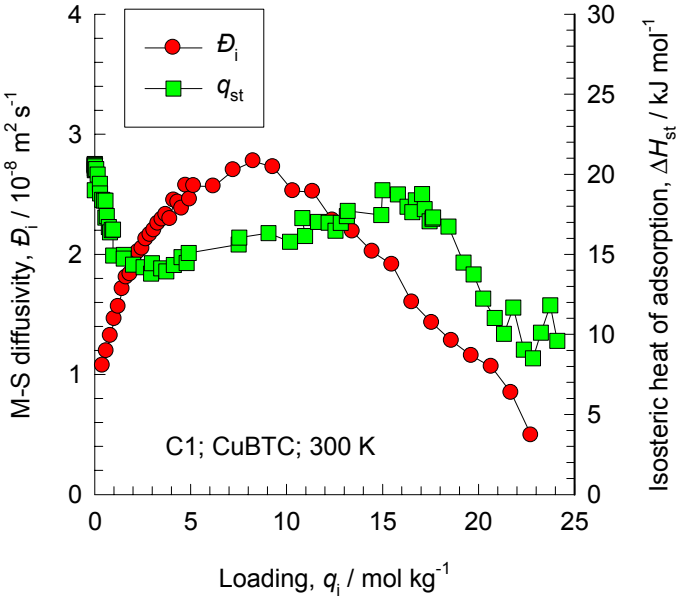

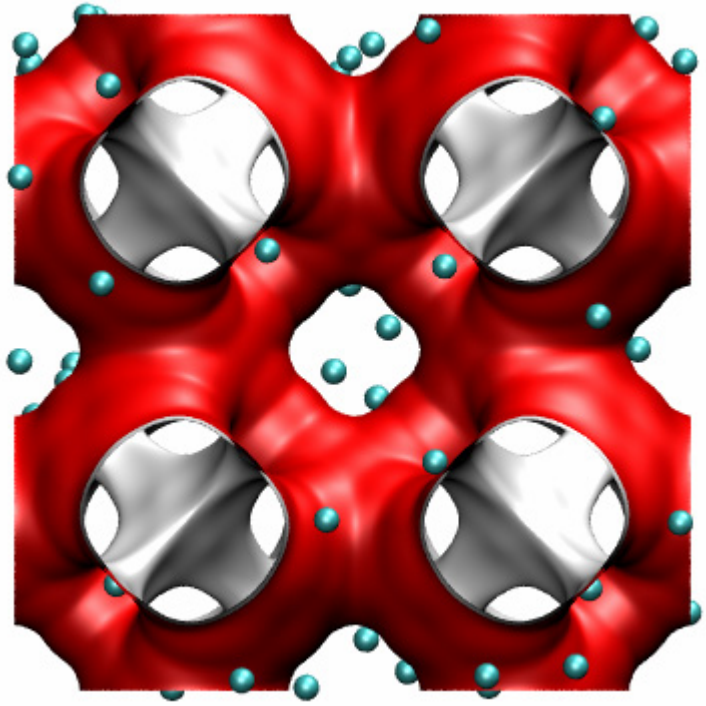

CuBTC
300 K
C1

Figure 11

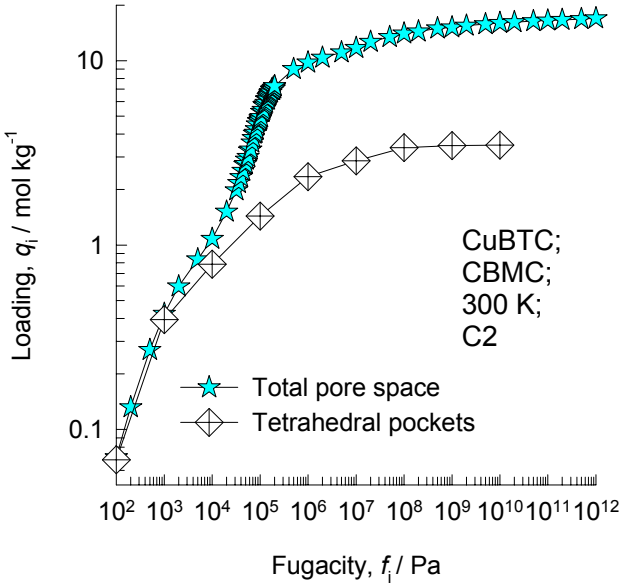

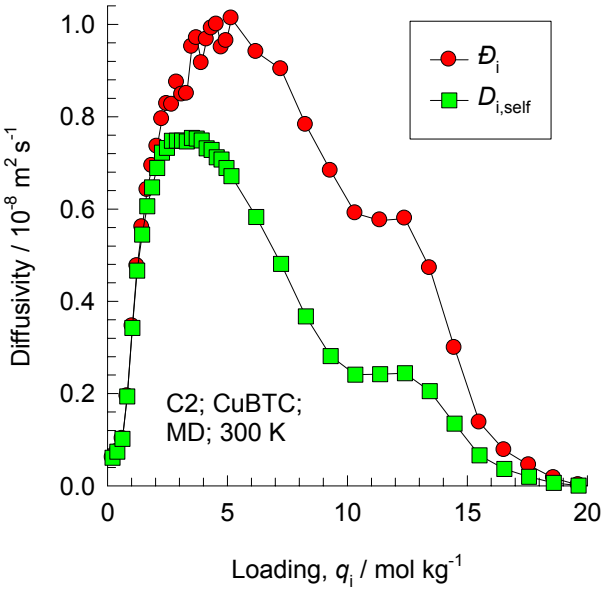

CuBTC, 300 K
C2

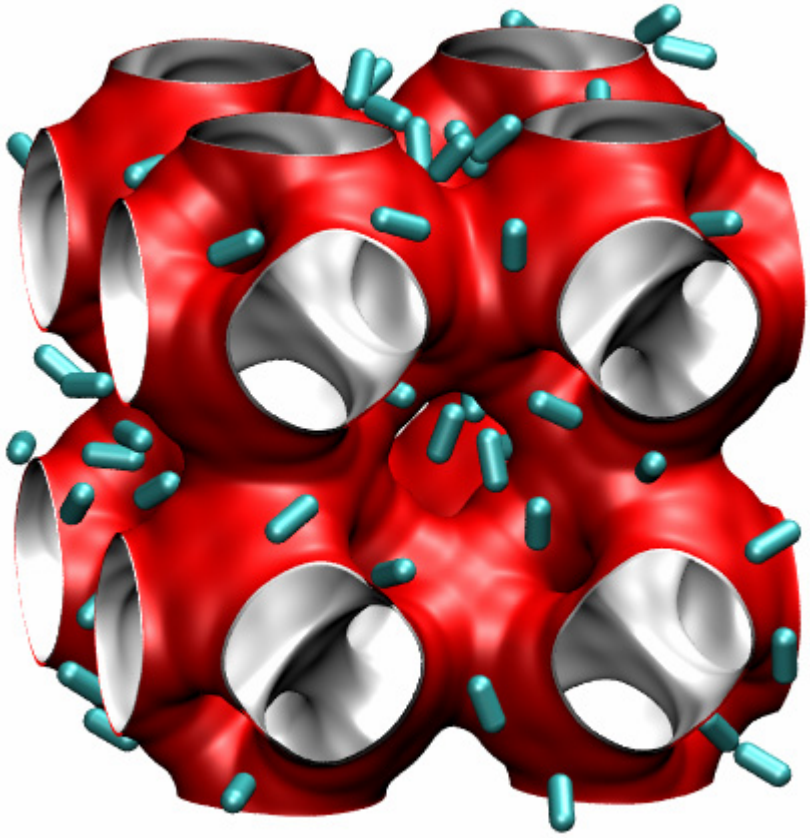

Figure 12

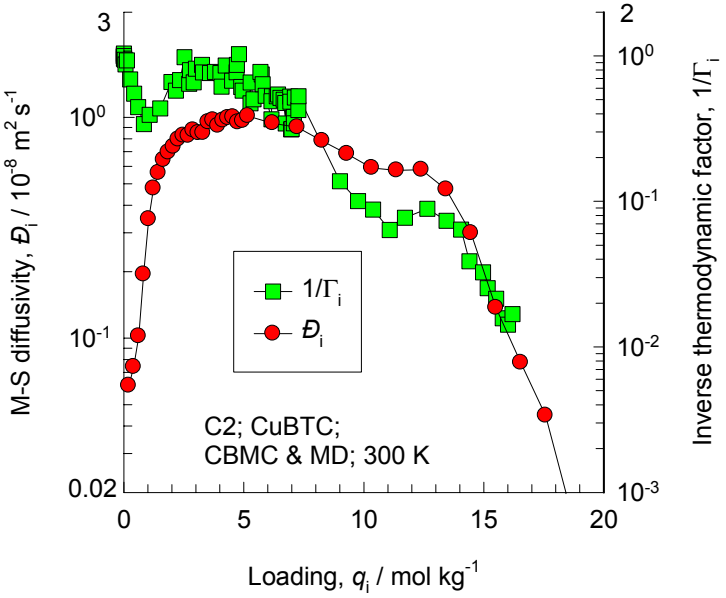

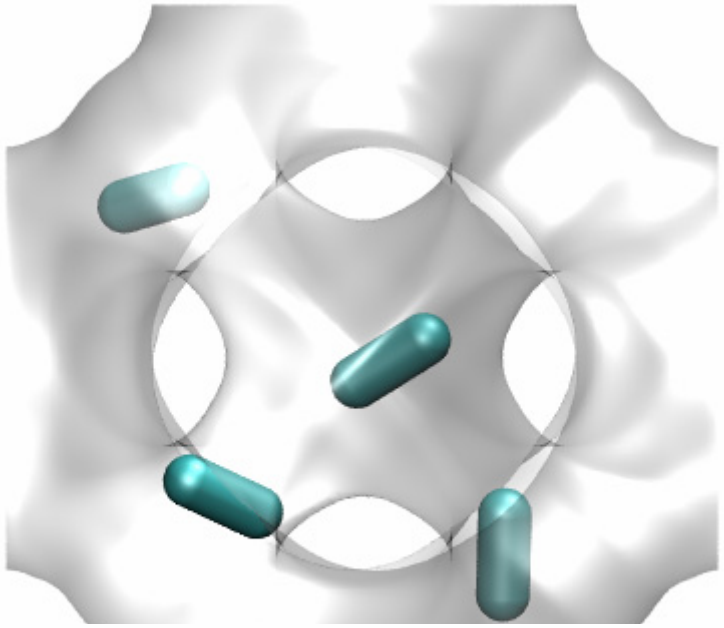

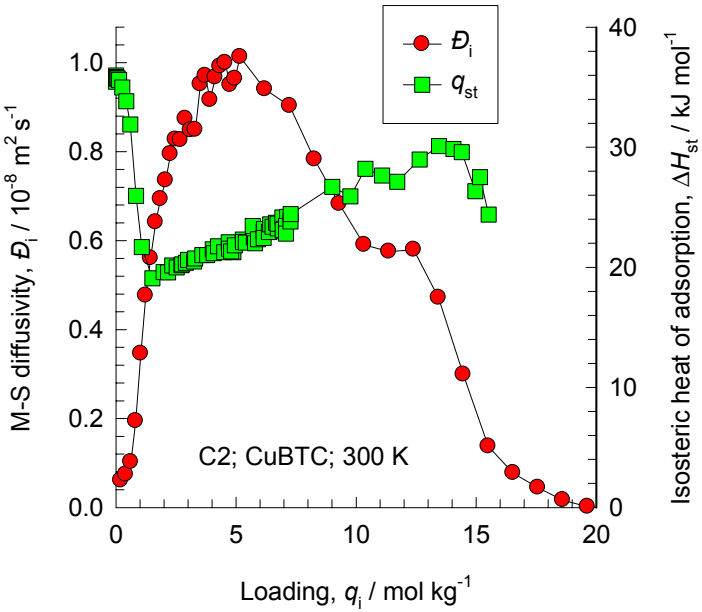

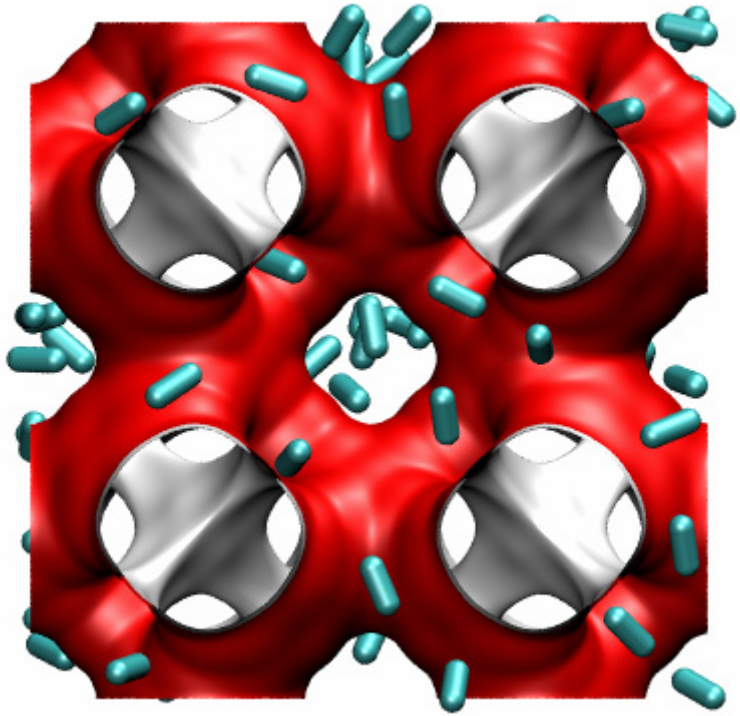

CuBTC
300 K
C2

Figure 13

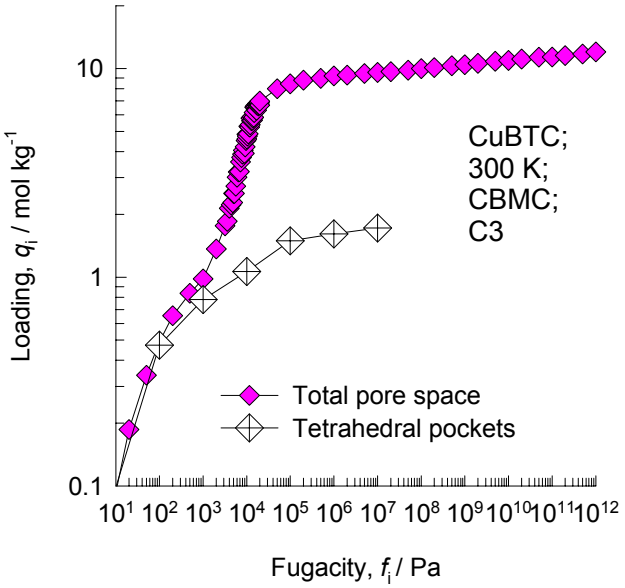

CuBTC, 300 K
C3

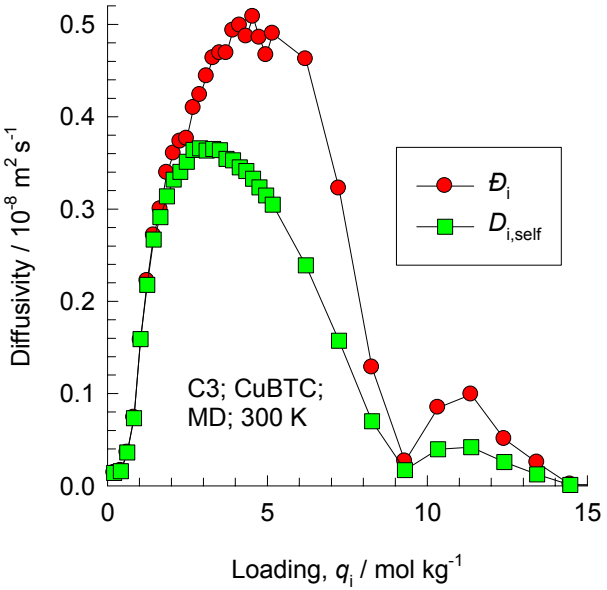

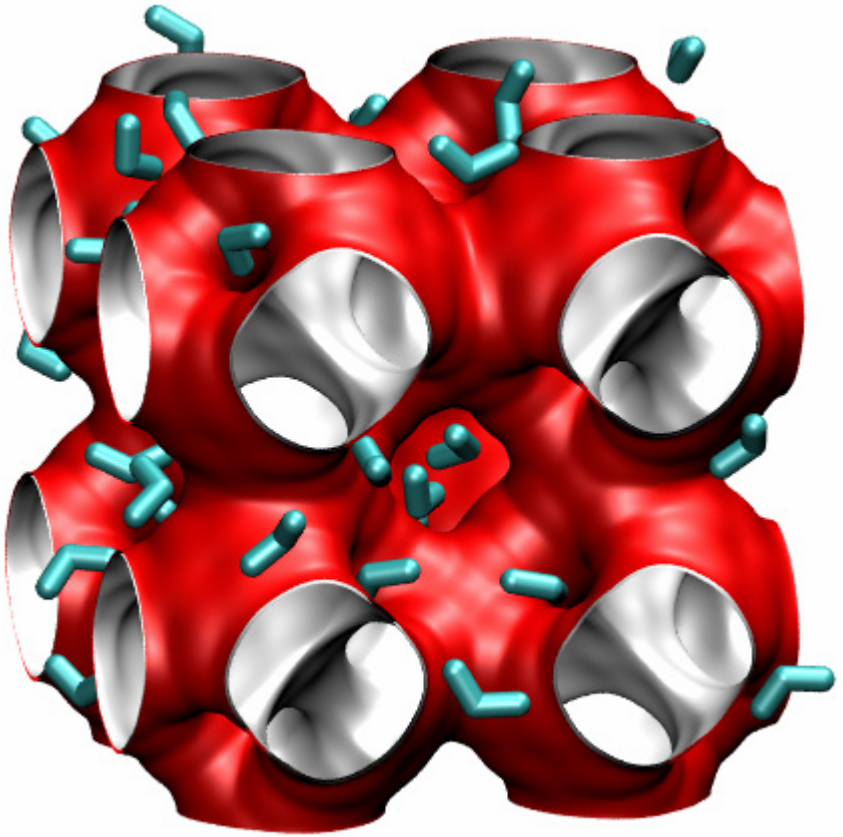

Figure 14

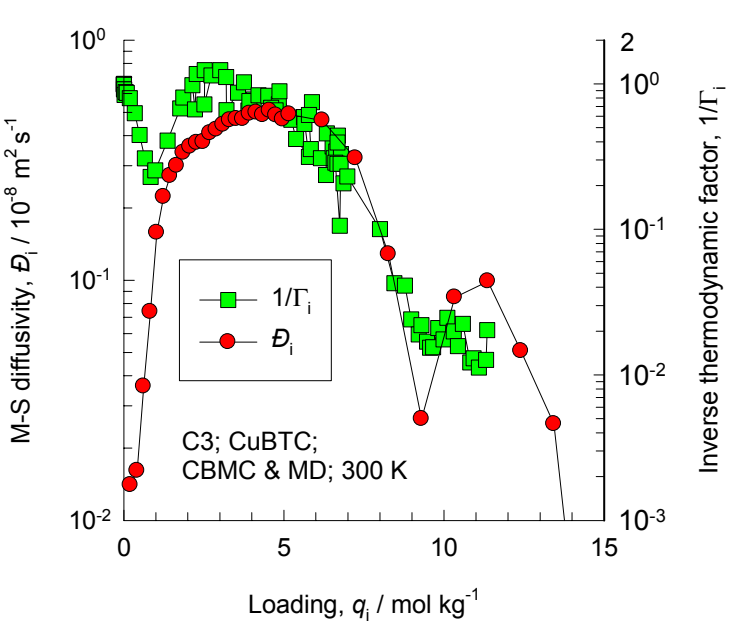

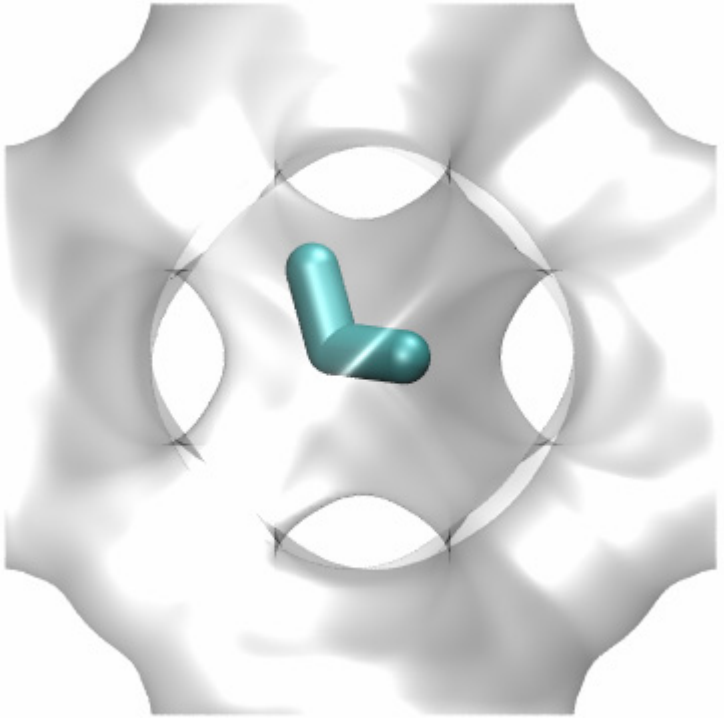

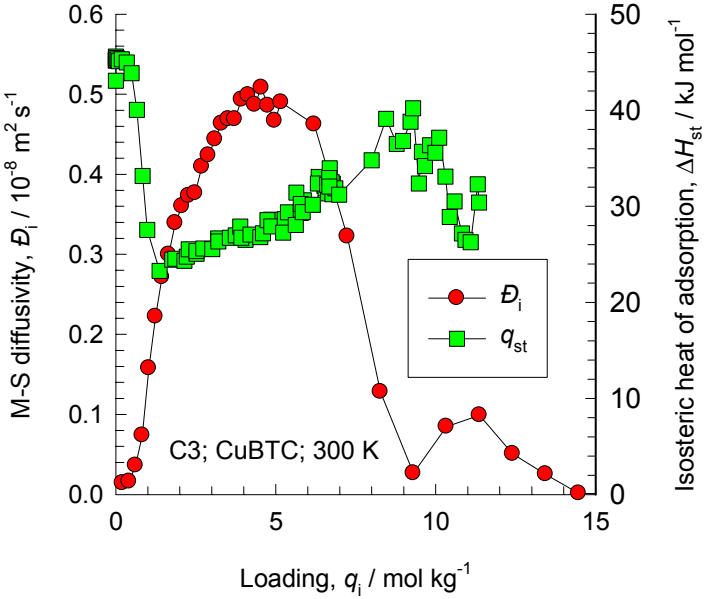

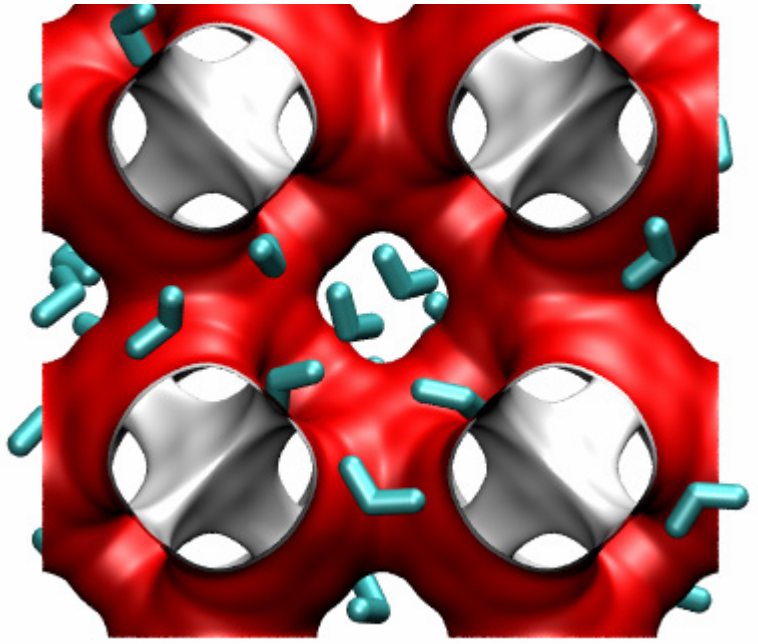

CuBTC
300 K
C3

Figure 15

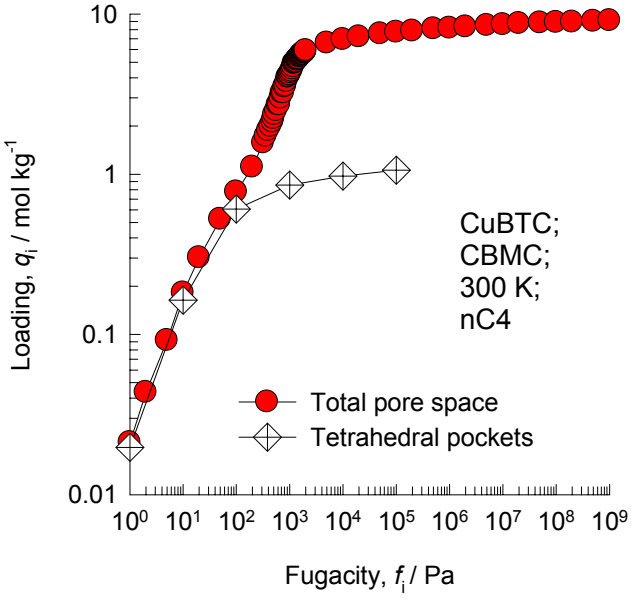

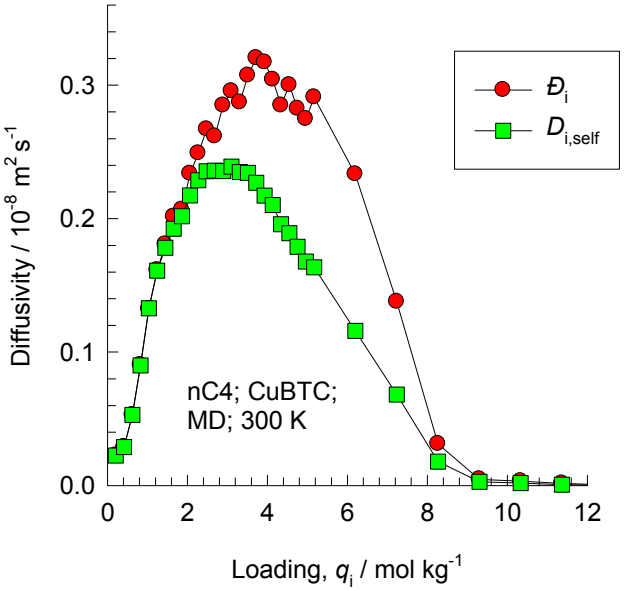

CuBTC, 300 K
nC4

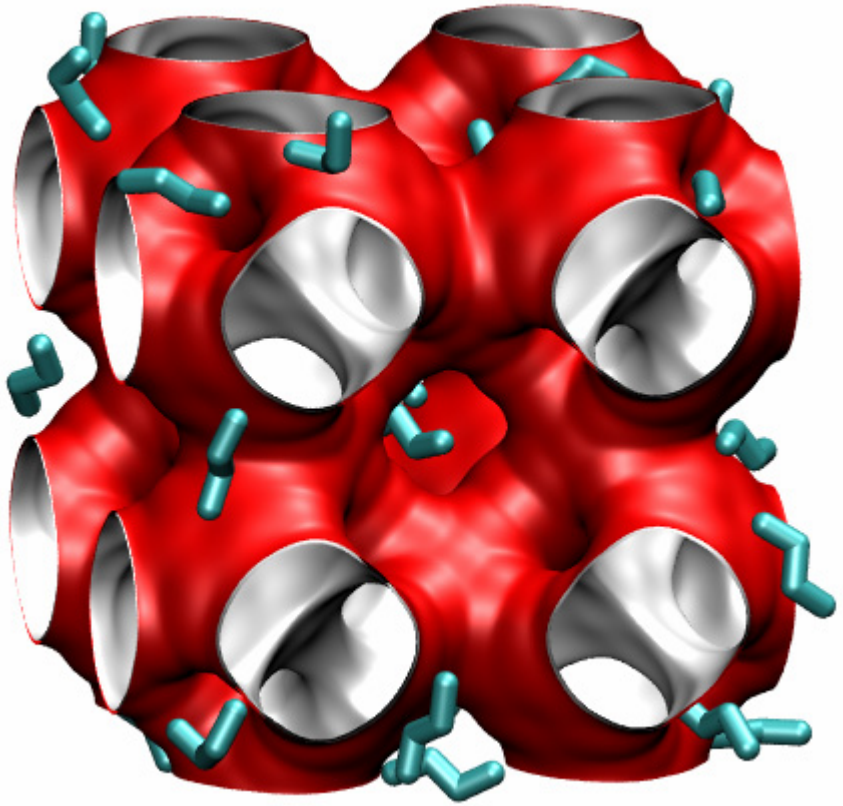

Figure 16

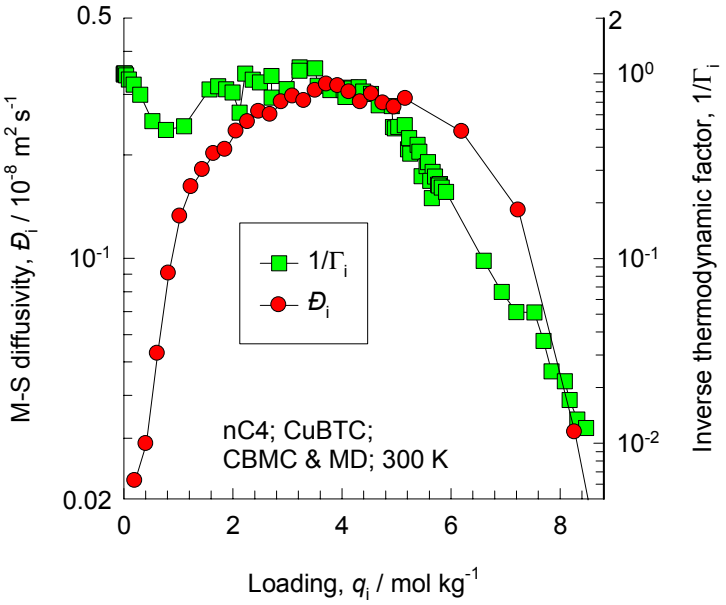

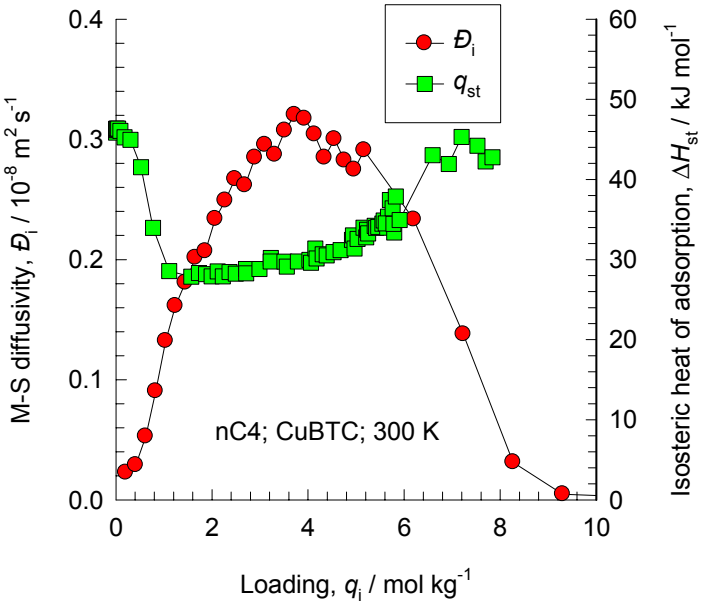

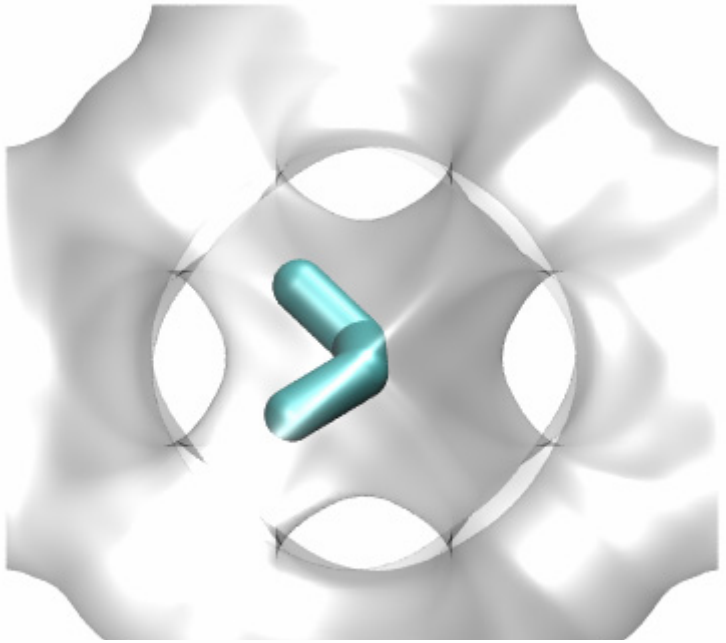

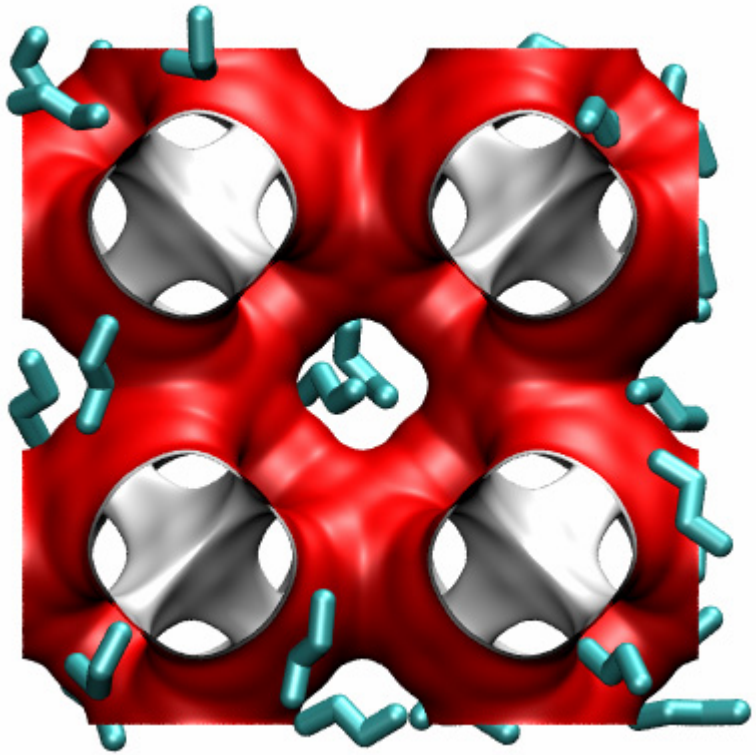

CuBTC
300 K
nC4

Figure 17

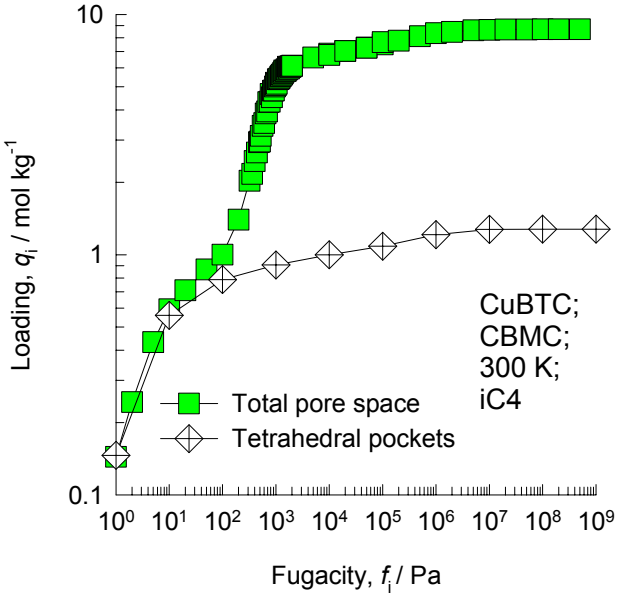

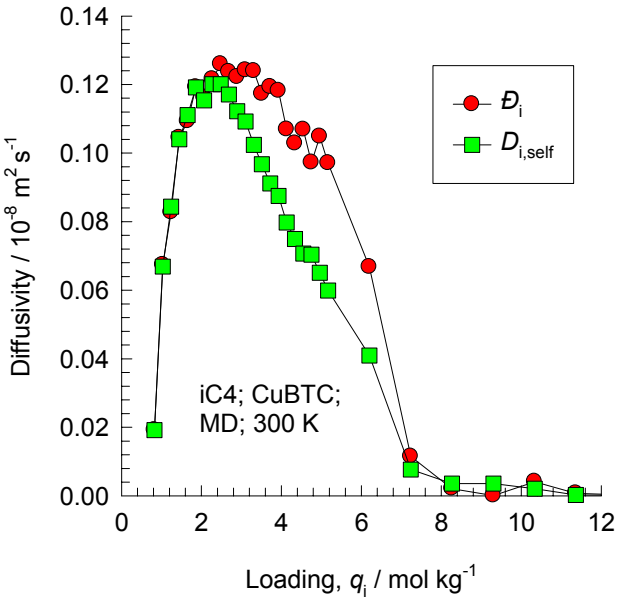

CuBTC, 300 K
iC4

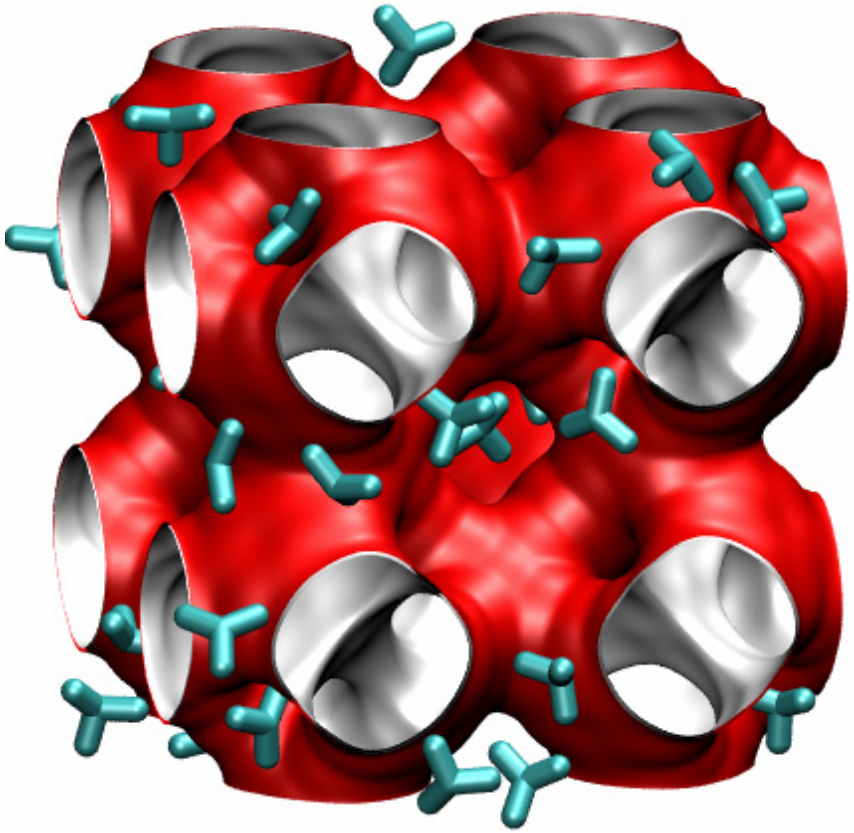

Figure 18

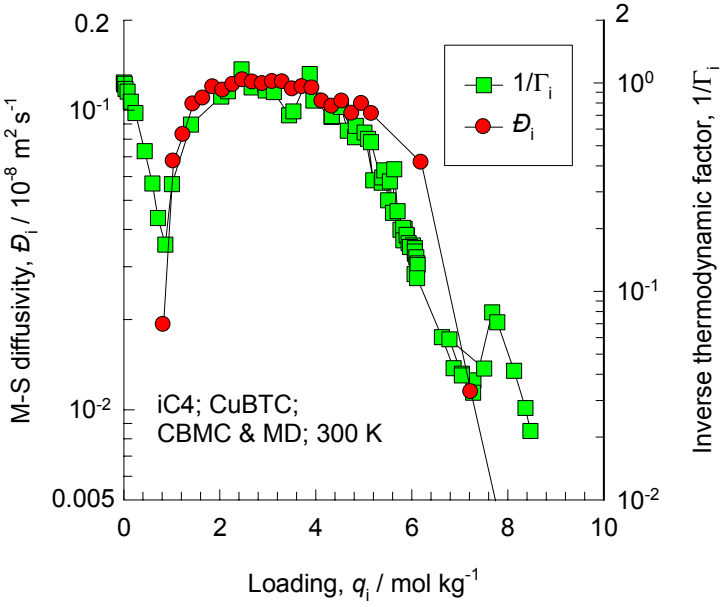

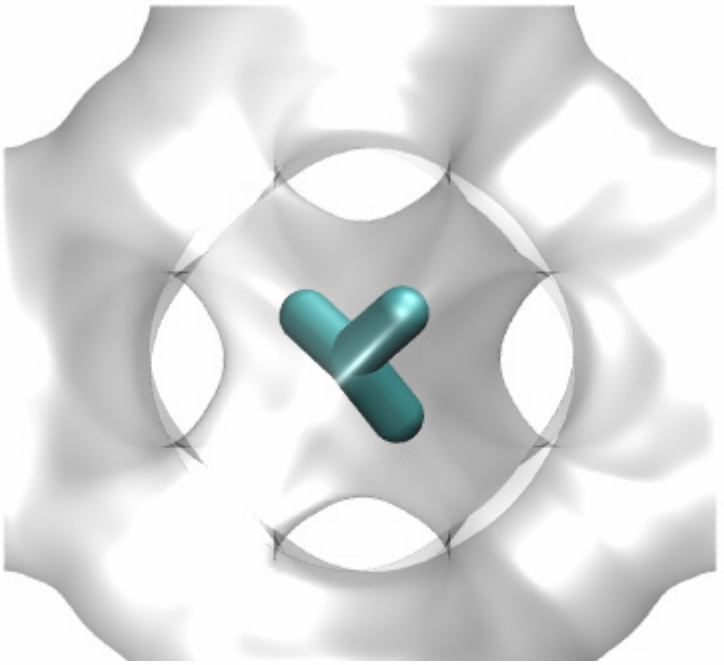

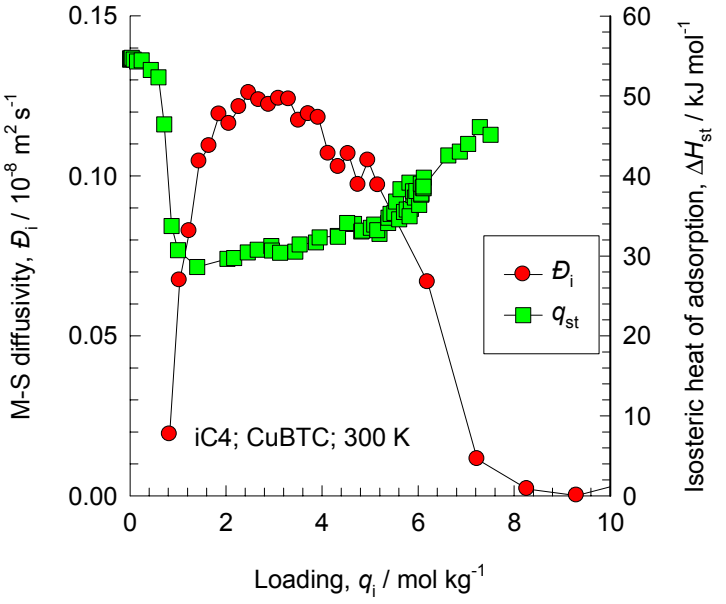

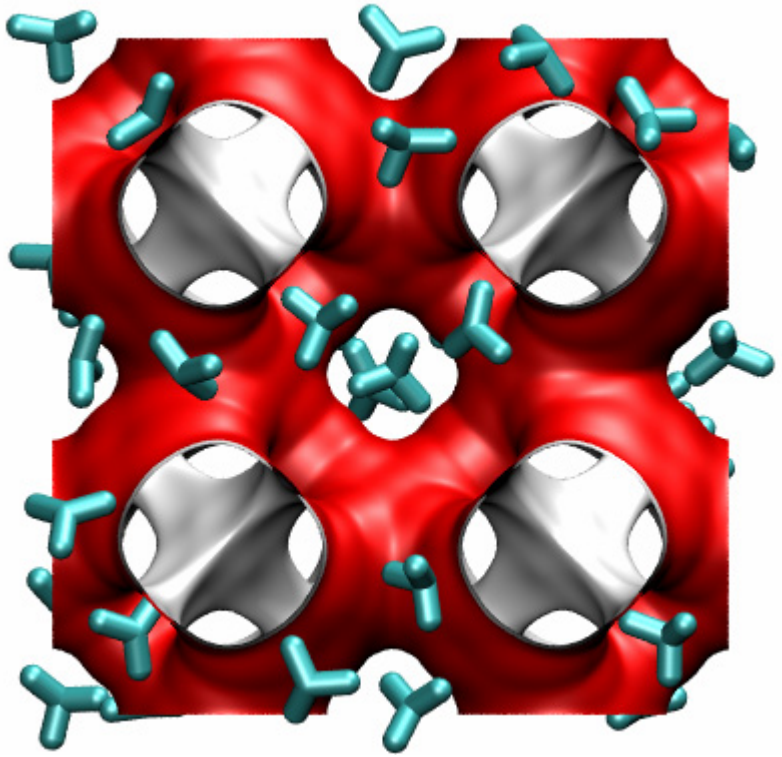

CuBTC
300 K
iC4

Figure 19

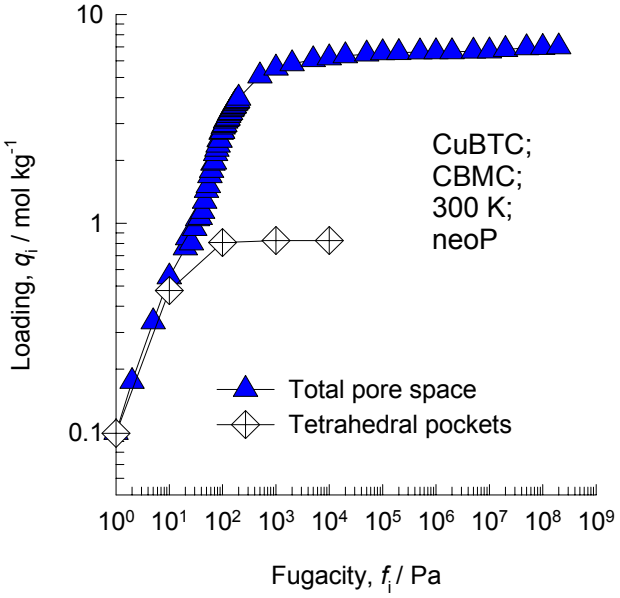

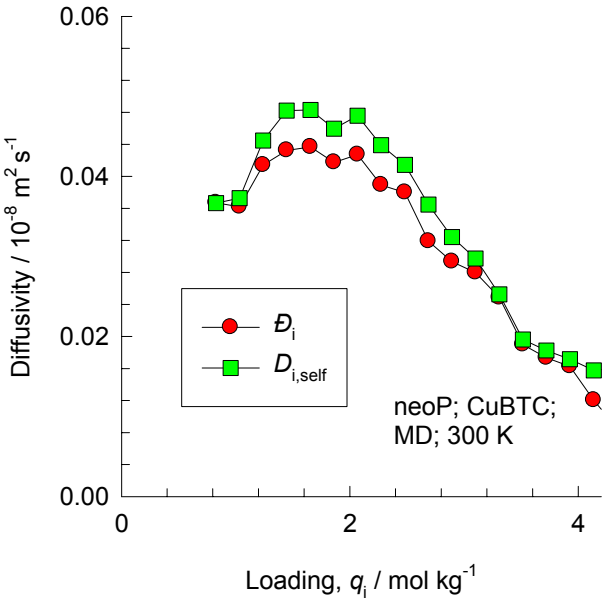

CuBTC, 300 K
neoP

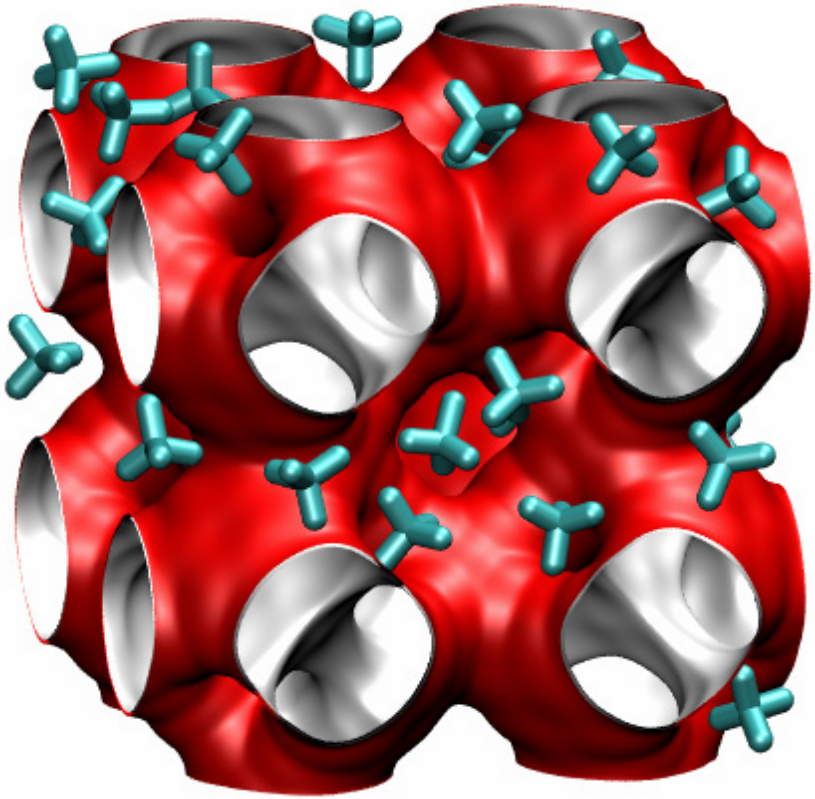

Figure 20

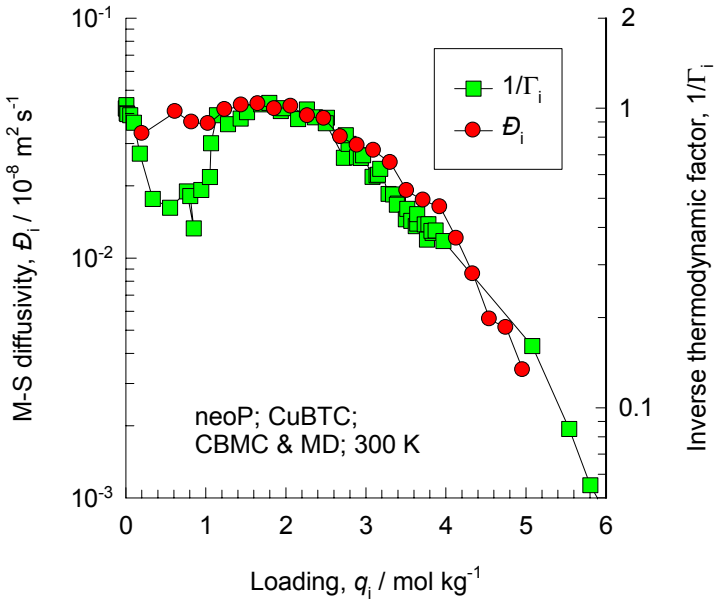

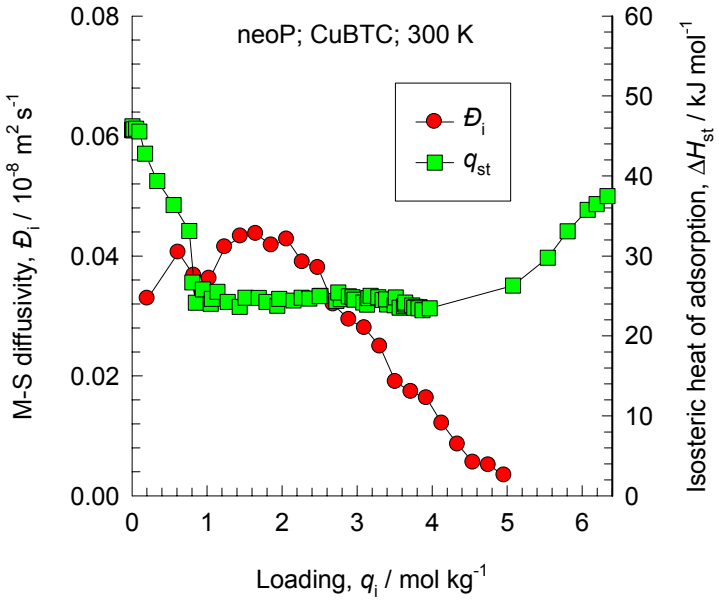

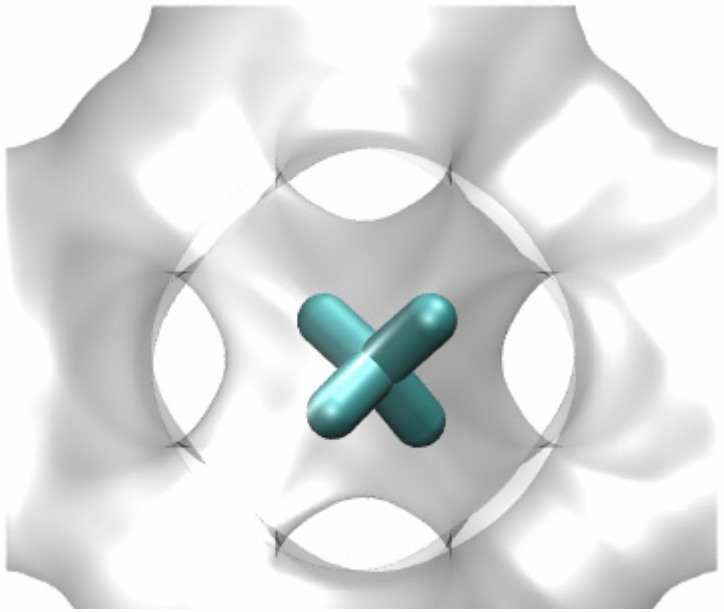

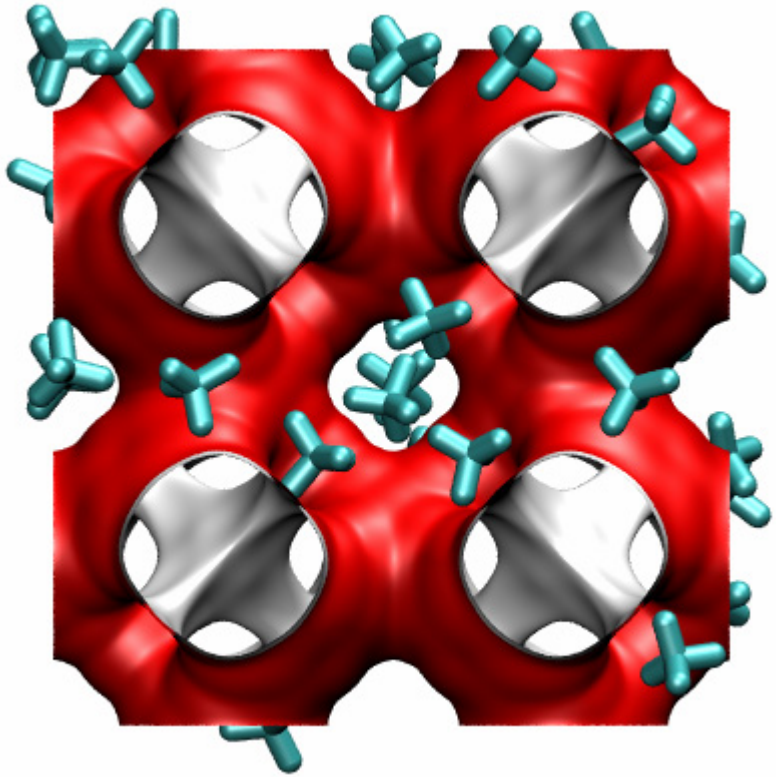

CuBTC
300 K
neoP

Figure 21

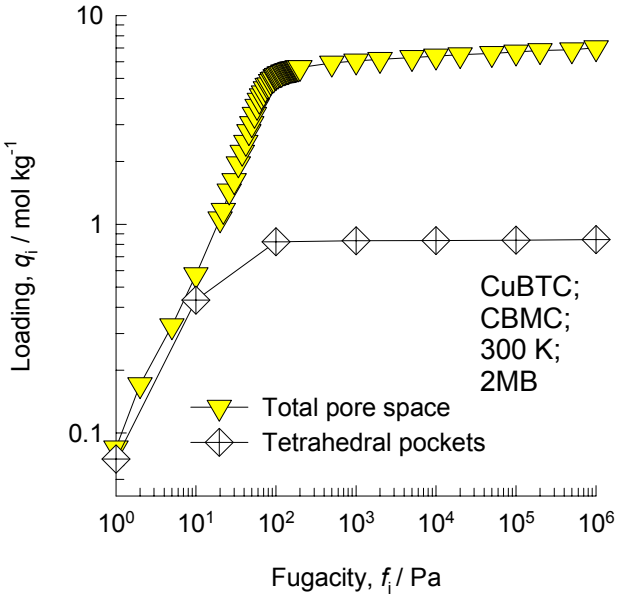

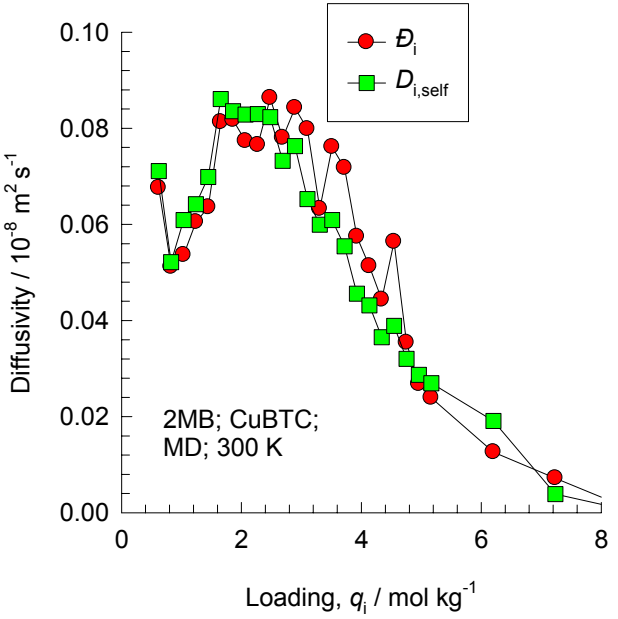

CuBTC, 300 K
2MB

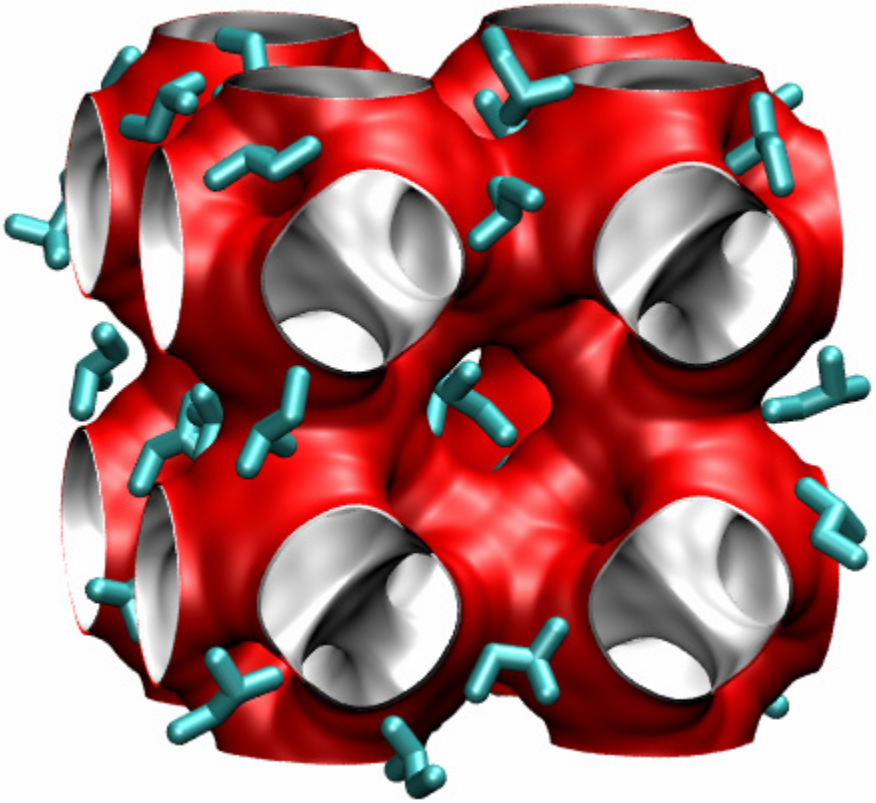

Figure 22

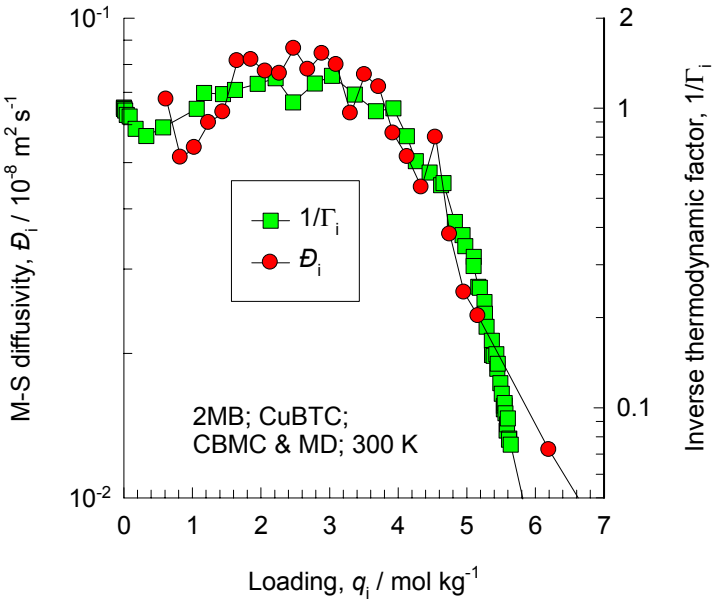

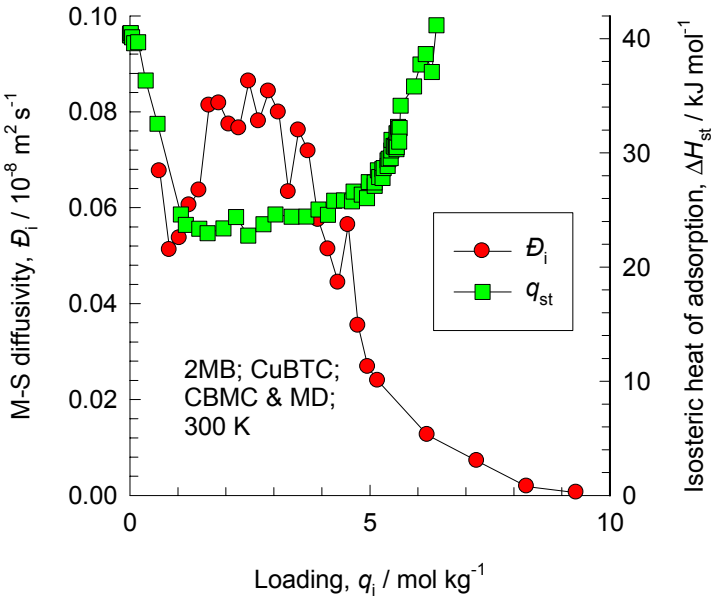

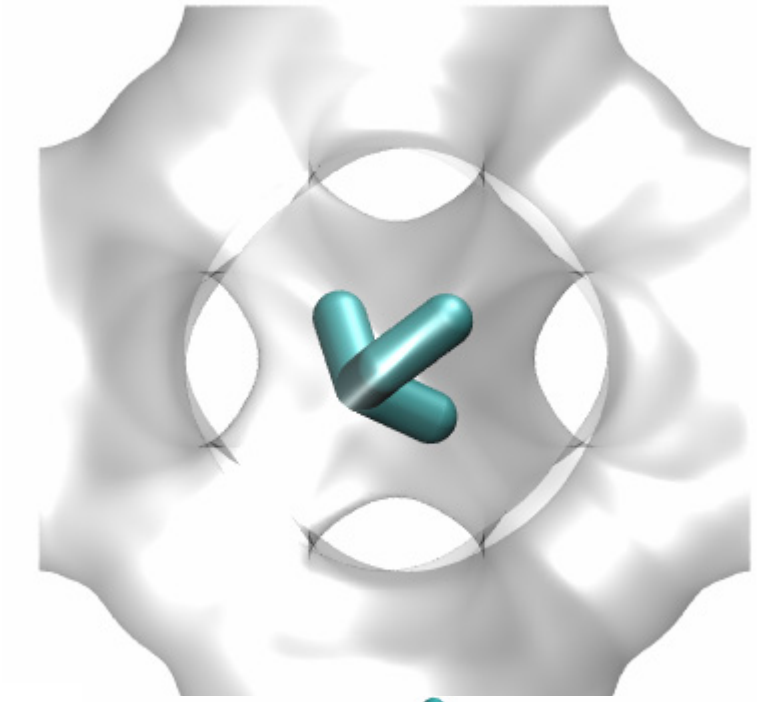

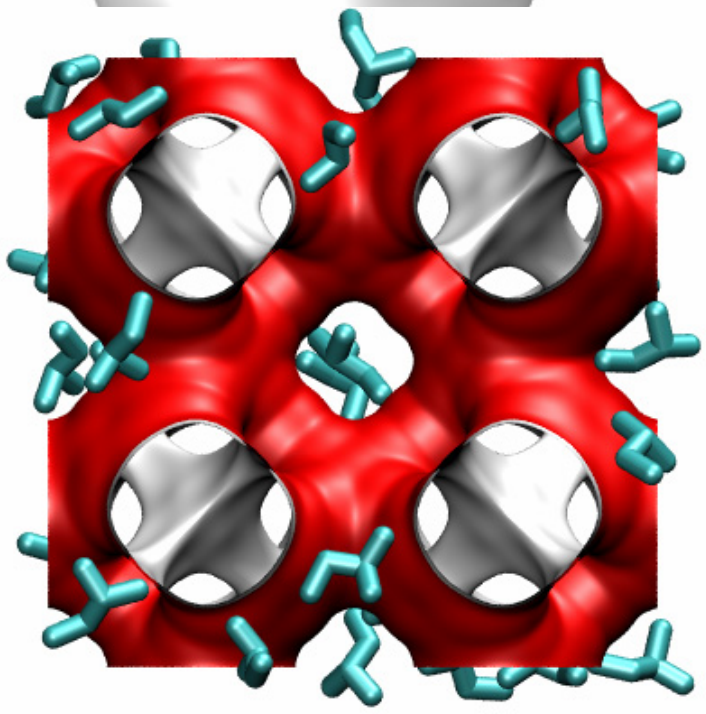

CuBTC
300 K
2MB

Figure 23

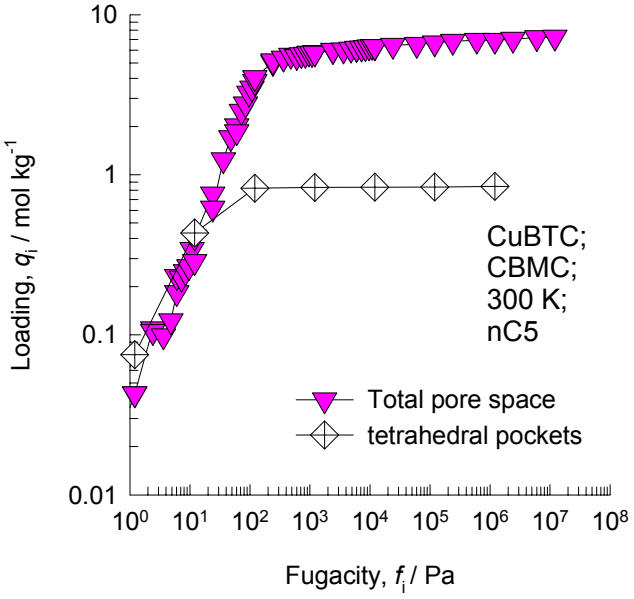

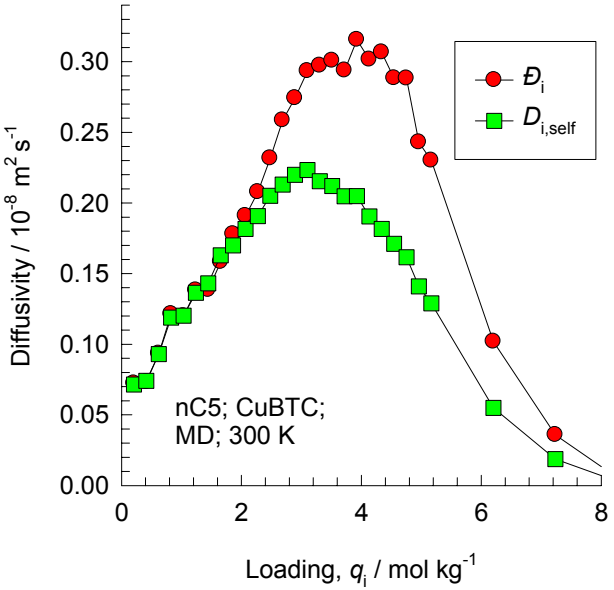

CuBTC, 300 K
nC5

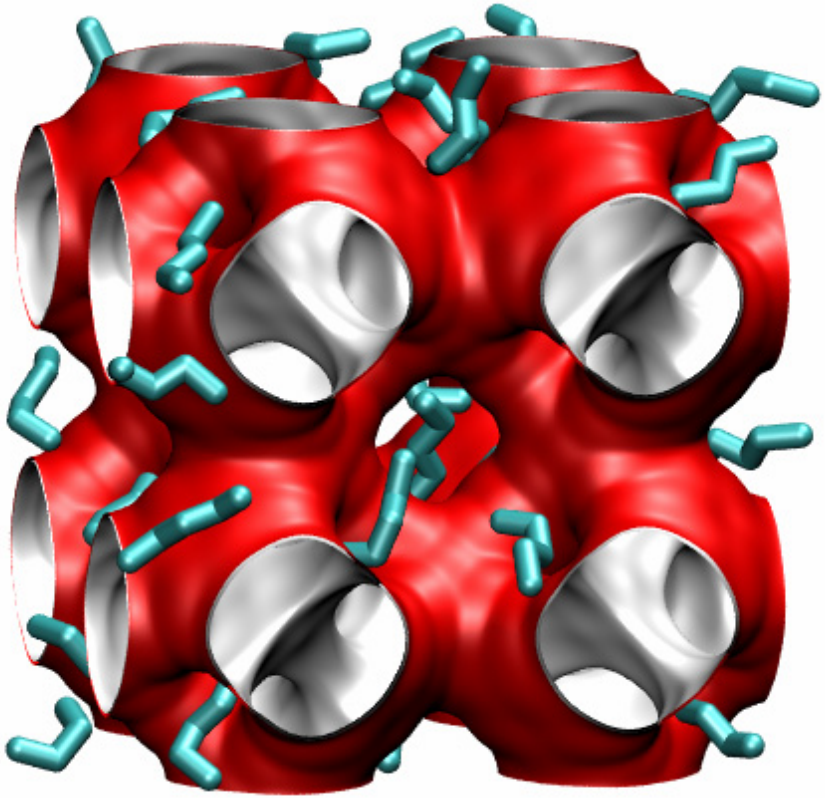

Figure 24

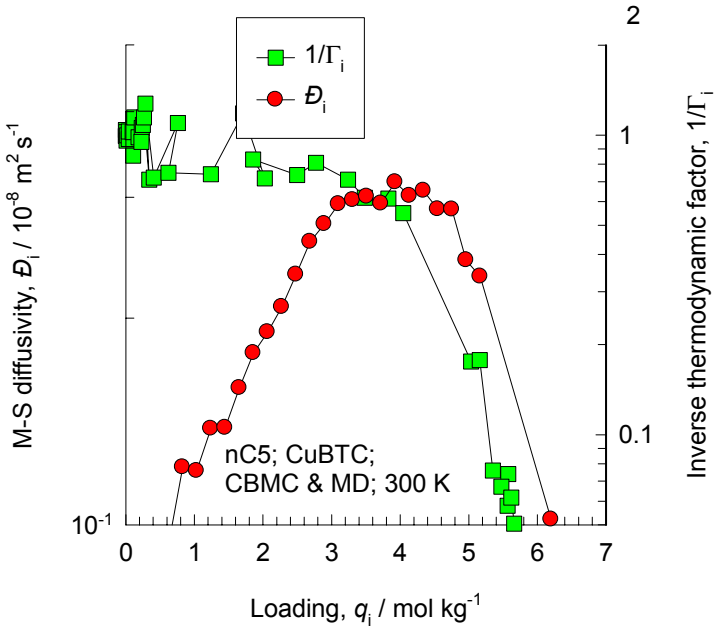

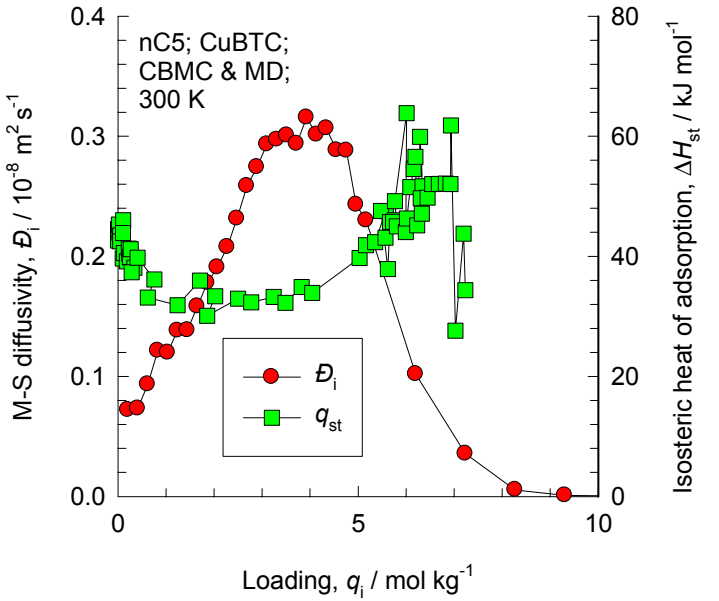

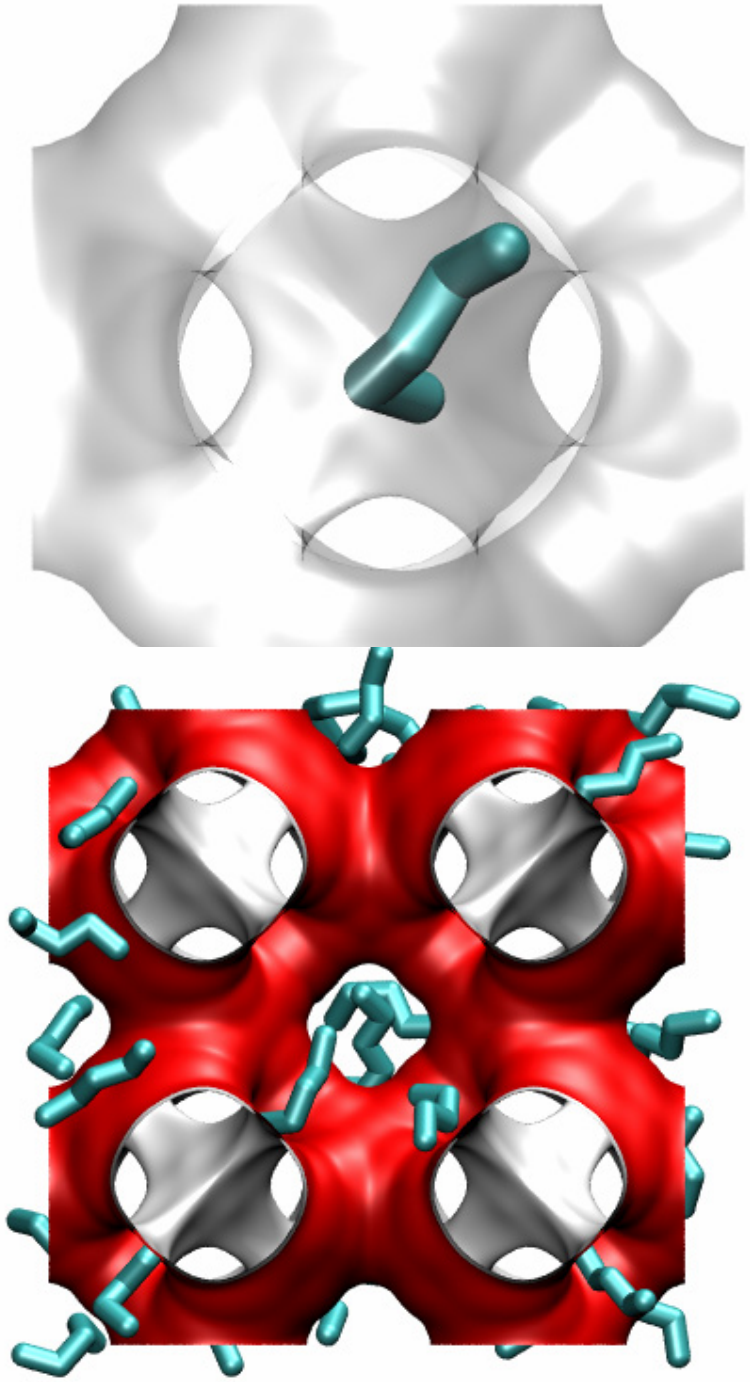

CuBTC
300 K
nC5

Figure 25

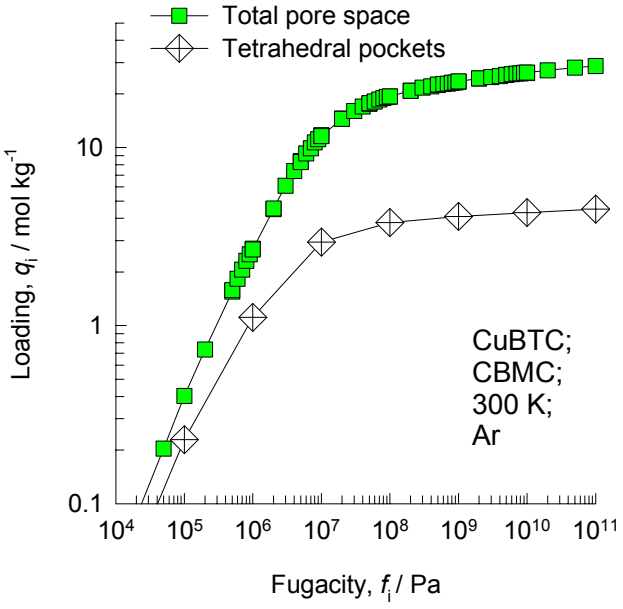

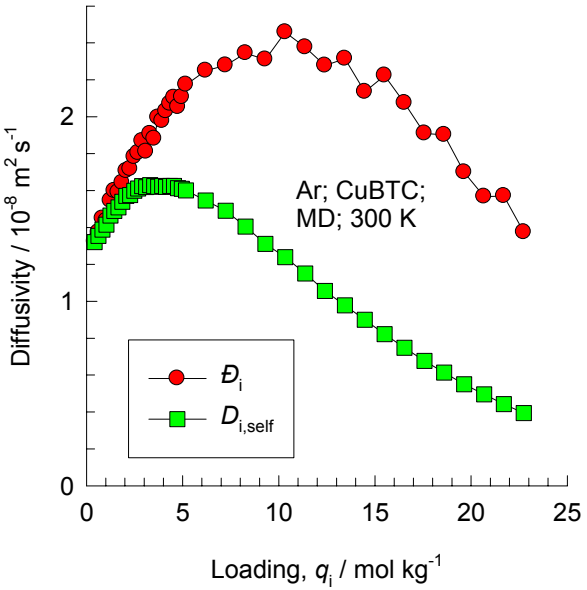

CuBTC, 300 K
Ar

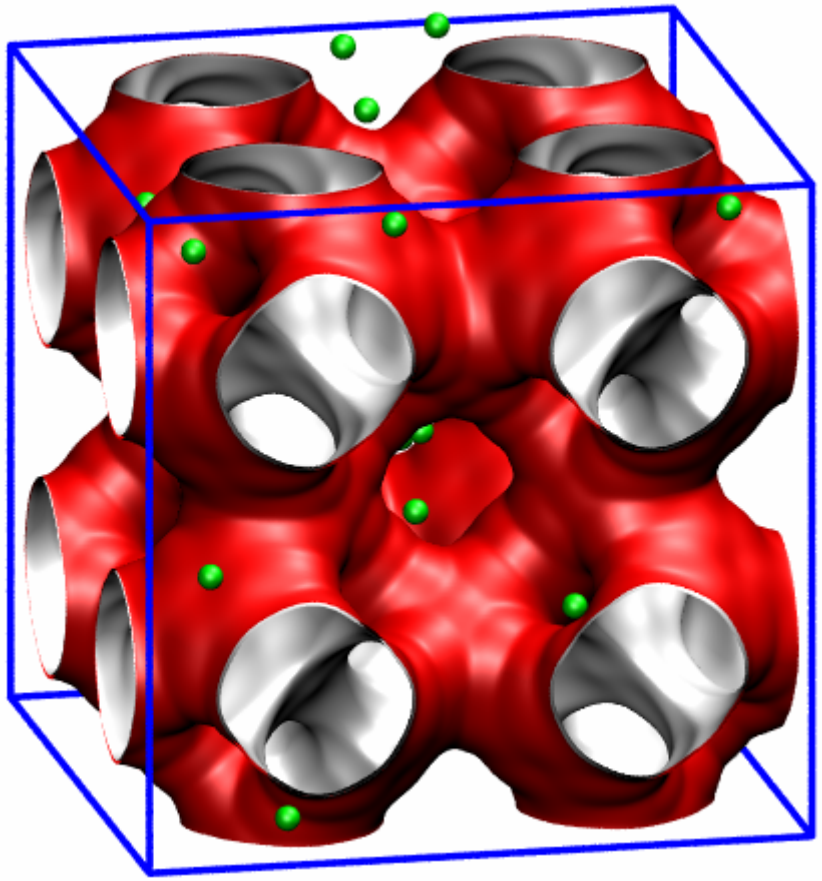

Figure 26

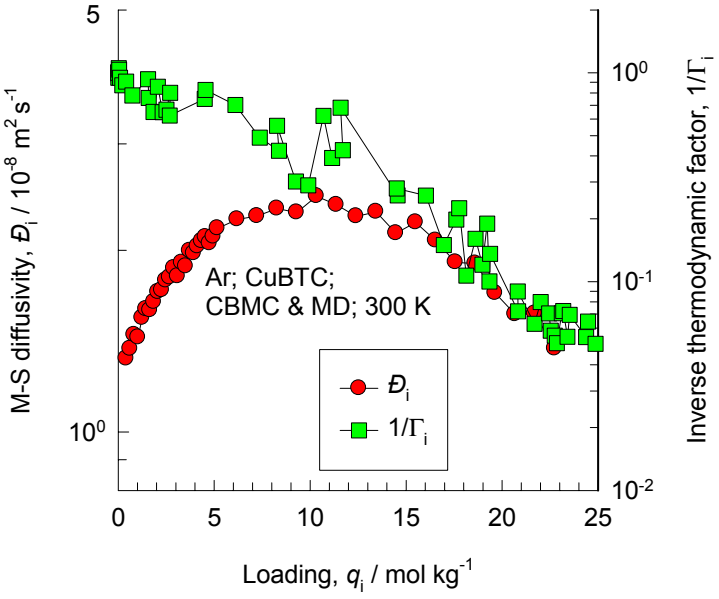

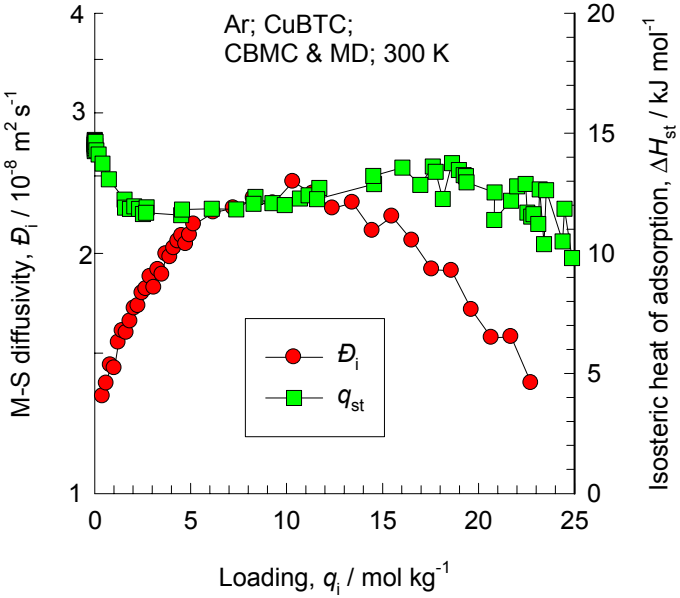

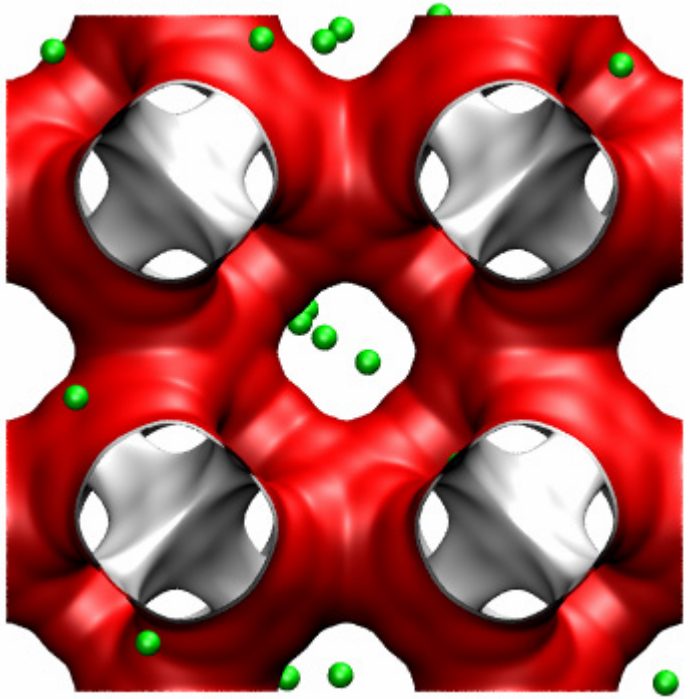

CuBTC
300 K
Ar

Figure 27

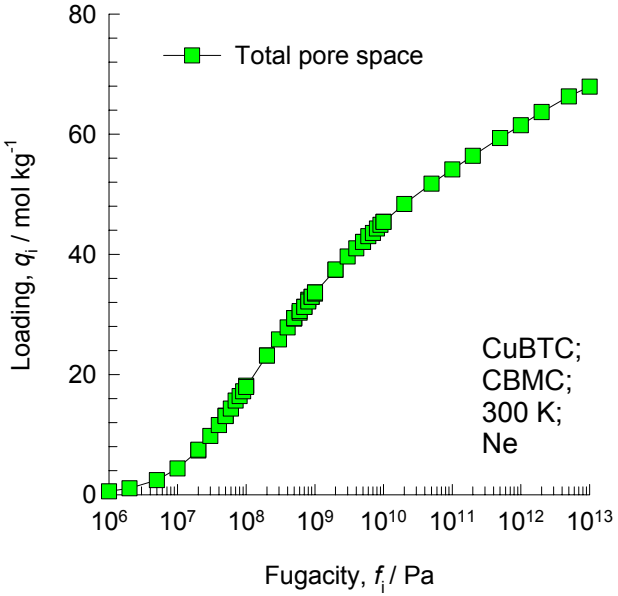

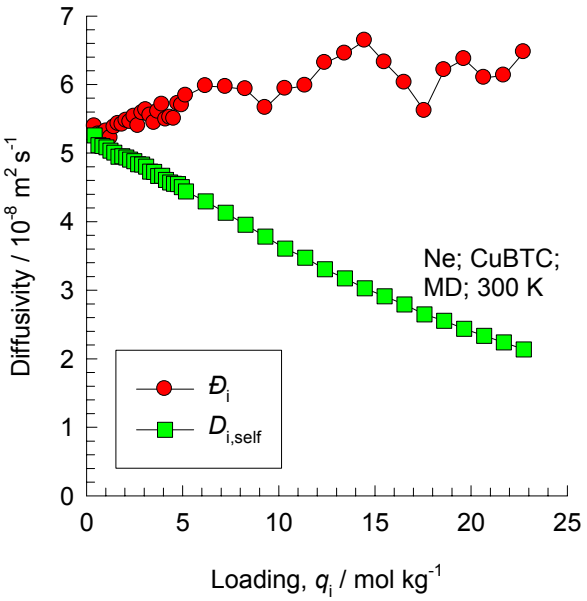

CuBTC, 300 K
Ne

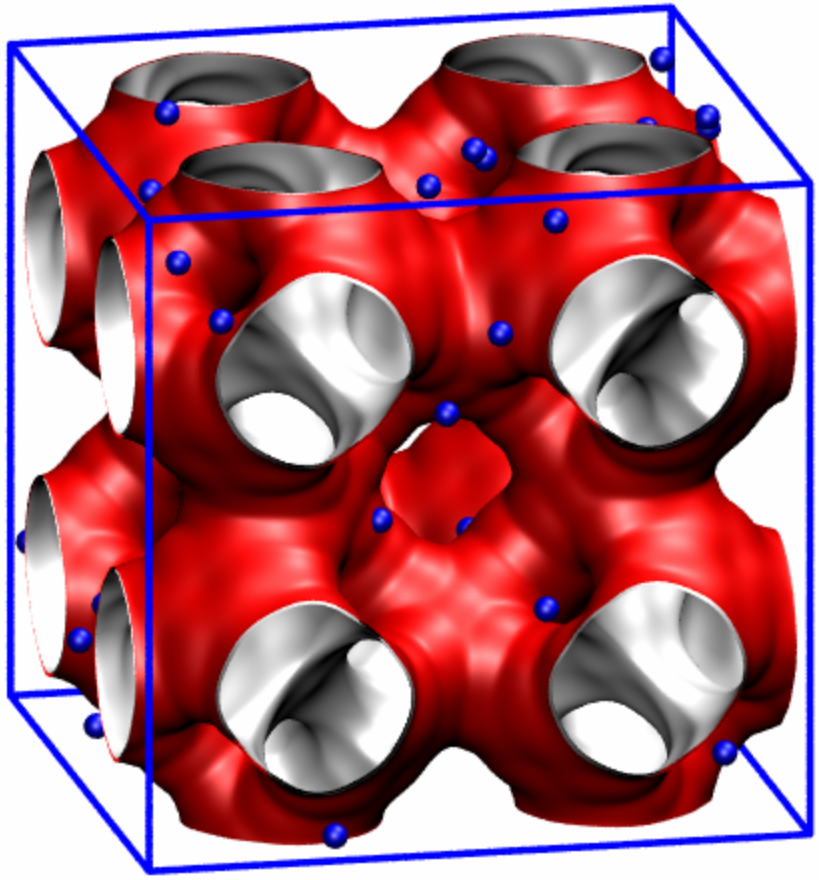

Figure 28

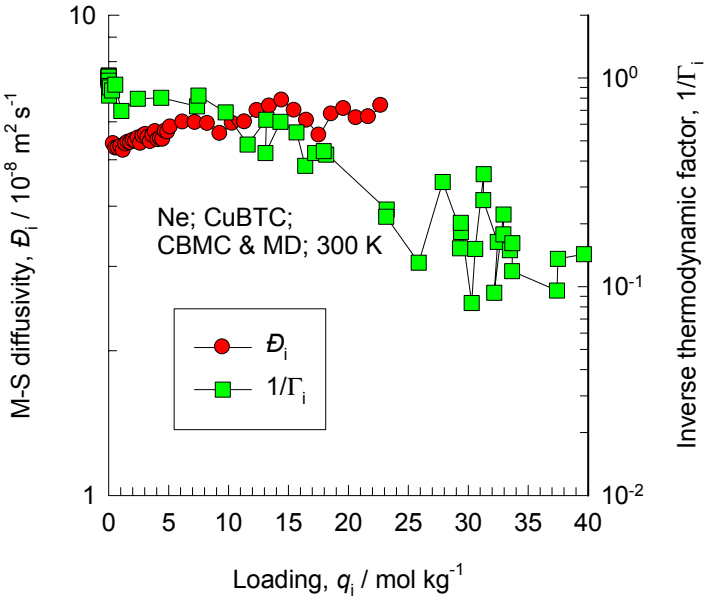

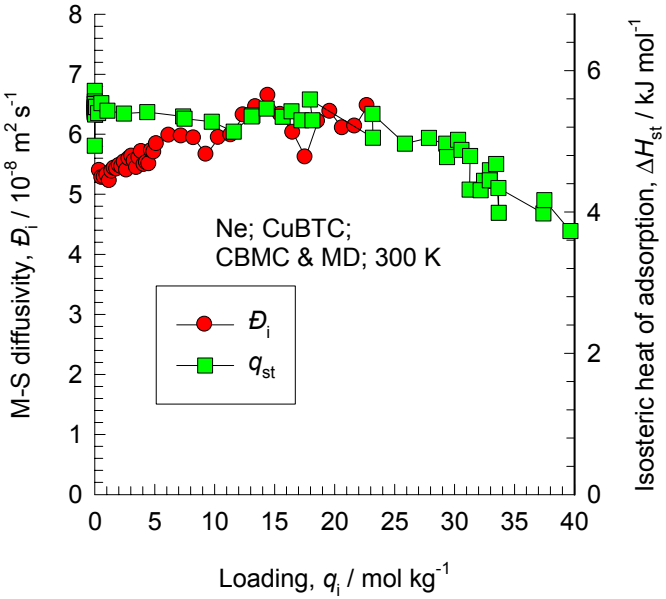

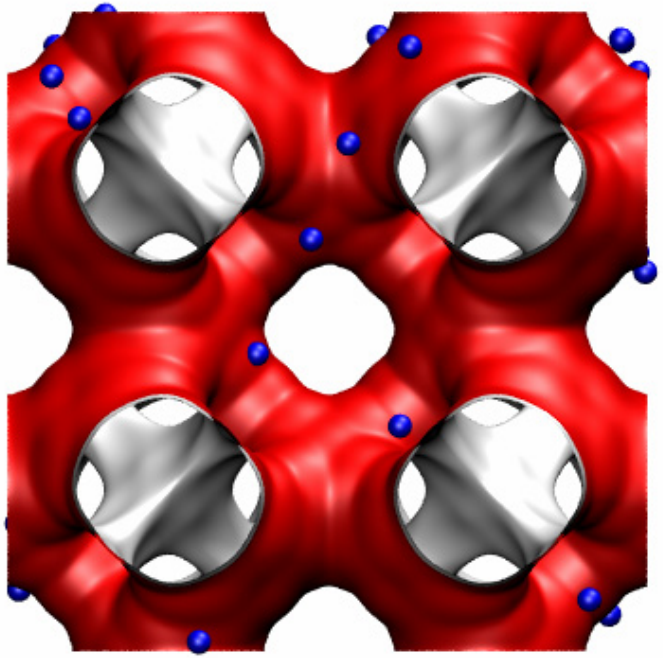

CuBTC
300 K
Ne

Figure 29

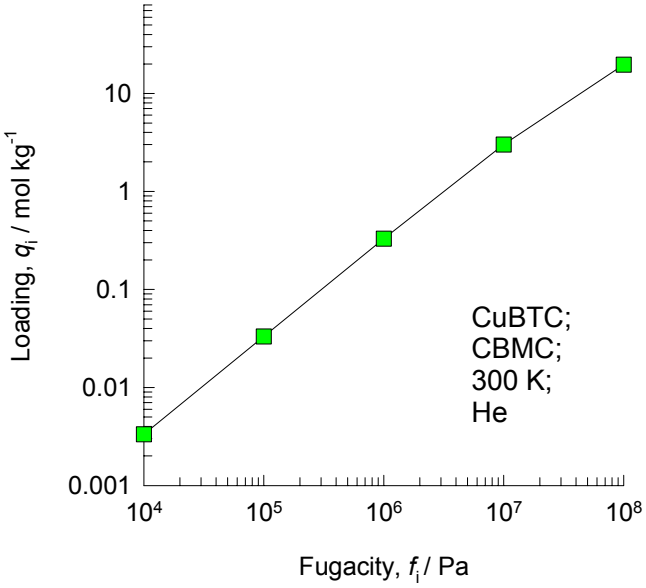

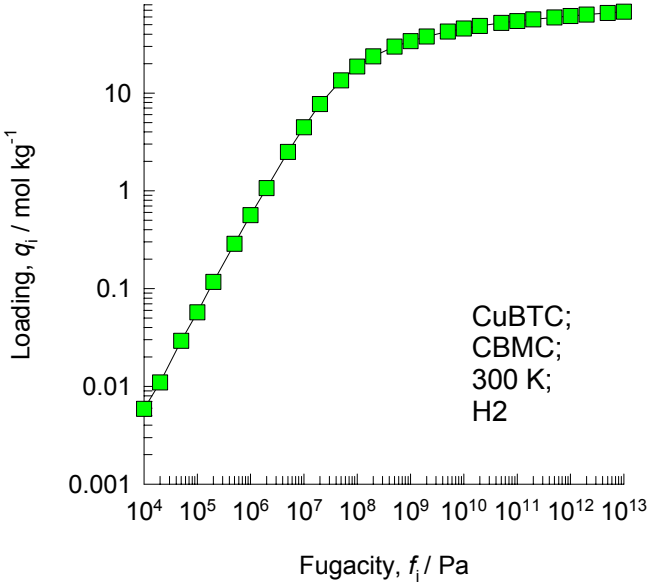

CuBTC, 300 K, He

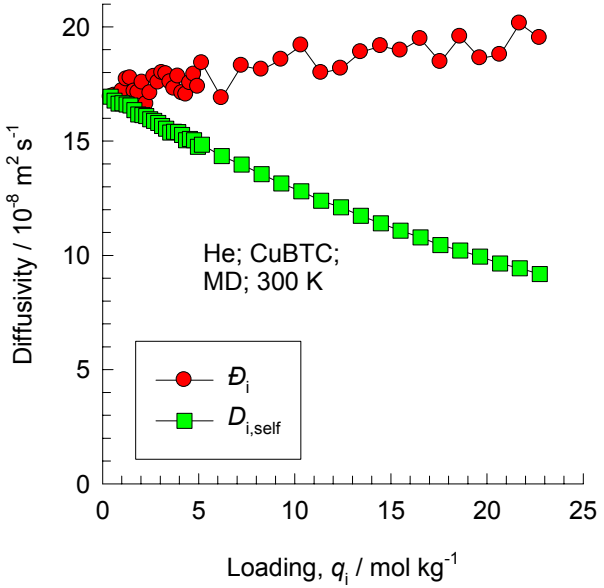

CuBTC, 300 K, H2

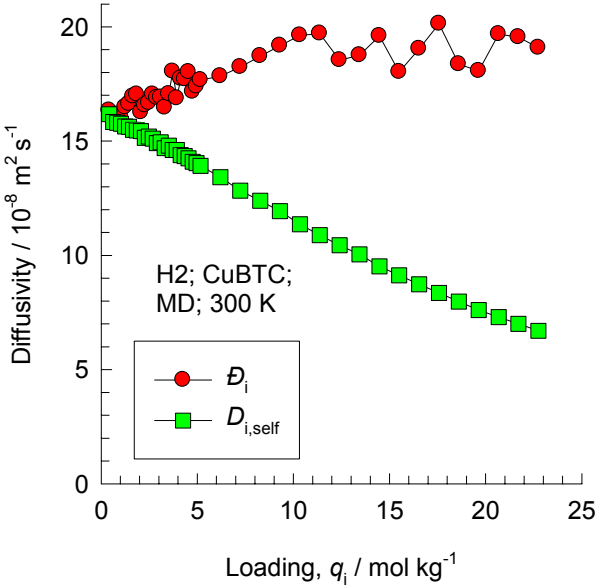

Figure 30

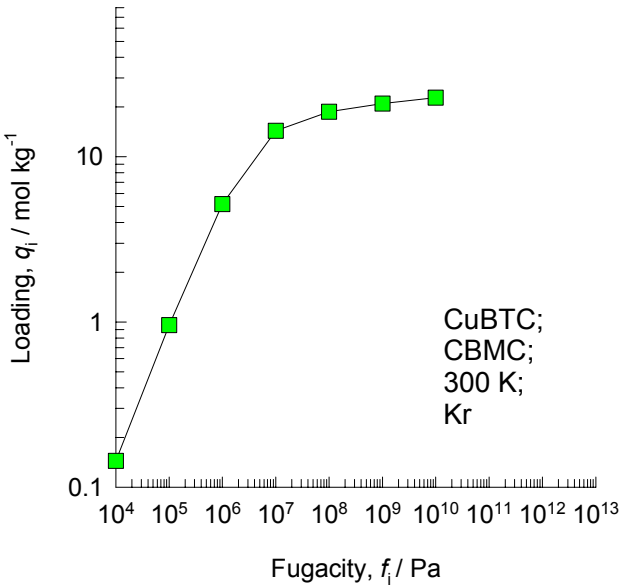

CuBTC, 300 K, Kr